Global gyrokinetic simulations of electrostatic microturbulent transport in LHD stellarator and aditya-u tokamak

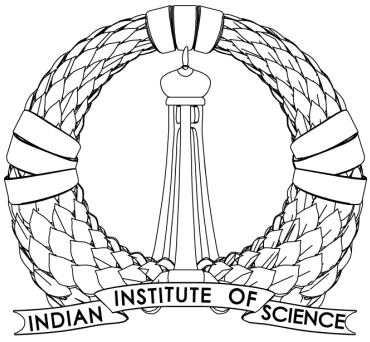

Tajinder Singh

Department of Physics

Submitted in partial fulfilment for the requirements of the degree of

Doctor of Philosophy

May 2023

Declaration

I declare that the work presented in this thesis is original and carried out by me at the Department of Physics, Indian Institute of Science, Bangalore. The appropriate references and citations of the previous work by different researchers are made wherever necessary. I also abide by academic honesty and integrity principles while presenting this work. I further declare that any degree, diploma, fellowship, or similar title has not been awarded to any university or institution based on this work.

Tajinder Singh

Dedicated to my
parents
&
sisters

Acknowledgements

Firstly, I would like to express my sincere gratitude to my thesis supervisor Dr. Animesh Kuley for his continuous support and guidance during the years of my PhD. Over this journey, his friendly nature has always been a source of inspiration for me. I am also thankful to him for giving me the independence to carry out the work.

I am grateful to Prof. Zhihong Lin and Dr. Javier Hernandez Nicolau for their guidance and support during my PhD. I thank Dr. Xishauo Wei for the helpful discussions. A special thanks to Prof. Abhijit Sen, Prof. Joydeep Gosh, Dr. Sarveshwar Sharma, and Dr. Federico Nespoli for a fruitful collaboration.

Thanks to the physics department chair, Prof. Prabal Kumar Maiti, for his support and excellent administration. I am obliged to Prof. Manish Jain and Prof. Anindya Das for a great learning experience during my coursework. I want to thank the members of my comprehensive exam committee, Dr. Piyali Chatterjee, Dr. Tanmoy Das, and Dr. Biplob Bhattacharya. It was my pleasure to have them in my comprehensive exam.

I sincerely thank the scientific staff at SERC, IISc, particularly Dr. Aditya Krishna Swamy, for the help and valuable discussion. I want to thank the office staff of the physics department for their support during my PhD. Thanks to Prof. David Logan, Prof. Prateek Sharma, and Prof. Prasad Hegde for the friendly discussions. I sincerely thank Prof. Dipshikha Chakravortty and Prof. P. S. Anil Kumar for the administration during COVID-19.

I want to extend my gratitude to Abhijit-3, Aditya, Akila, Ankan, Baljeet, Bhanu, Biswajit, Deebalena, Hardeep, Harshada, Jatendra, Jay, Karandeep, Kiran, Lavneet, Mannu, Mayank, Neda, Nilanjan, Nimitha, Nisarg, Rohit, Sahel, Samriddhi, Satpal, Shamim, Shinjin, Shubadeep, Siddharth, Sreekar, Venkat for giving me a friendly company.

Lastly, I am grateful to my mother (Kashmir Kaur), father (Jeet Singh), and sisters (Sonia and Sarbjeet) for their continuous support and love during my entire life, to say the least. This thesis would not have completed without their support.

Synopsis

Fusion plasma could act as a viable source of clean and unlimited energy, replacing fossil fuels and fission-based reactors. In this direction, inertial confinement fusion (ICF) and magnetic confinement fusion (MCF) are two major technological alternatives to achieve the nuclear fusion from the burning plasmas. ICF uses powerful lasers, such as one at Lawrence Livermore National Laboratory, to fuse the fusion reactants. Whereas MCF uses strong magnets that produce the magnetic field in a torus-shaped geometry to confine the fusion fuel. MCF, which is the focus of this thesis work, has gained considerable attention over the past few years for the commercialization of fusion reactors and thus inspired the world's largest fusion reactor, ITER (International Thermonuclear Experimental Reactor), to demonstrate the efficient replication of fusion reactions on Earth and hence to show the viability of nuclear fusion as a clean energy source. In this quest, the tokamak and the stellarator are two leading contenders for achieving nuclear fusion from magnetically confined plasmas. They differ in terms of magnetic field configuration in the toroidal direction. A tokamak is an axisymmetric device, and a stellarator is a non-axisymmetric device. Both of these concepts have inherent advantages and disadvantages in achieving nuclear fusion from toroidally burning plasmas. In particular, for the viability of fusion, the plasma confinement time should be sufficiently long to achieve a net energy balance. However, the measured particle and energy losses in fusion plasma are higher than those of collisional processes. This so-called anomalous transport is due to the small-scale instabilities, called micro-instabilities, that are a major cause of particle and heat loss from the device. Irrespective of the magnetic field structure, both the tokamak and the stellarator are prone to microturbulence, and thus their understanding and control are of paramount importance.

In this thesis, first-principles-based global gyrokinetic simulation studies of the electrostatic microturbulence are presented in the Large Helical Device (LHD) stellarator and ADITYA-U tokamak, using the state-of-the-art code GTC (Gyrokinetic Toroidal Code), and the effects of impurities on the microturbulence are investigated in both machines. (ADITYA-U is the first Indian tokamak, and LHD is one of the world's largest superconducting stellarators in Japan.)

In the first part of the thesis, global gyrokinetic simulations of the ion temperature gradient (ITG) and trapped electron mode (TEM) driven turbulence in the LHD stellarator are carried out with kinetic electrons using the monotonic smooth numerical plasma profiles. ITG simulations show that kinetic electron effects increase the growth rate by more than 50% and more than double the turbulent transport levels compared with simulations using adiabatic electrons. Zonal flow and microturbulence are ubiquitous in nature. Zonal flow dominates the saturation mechanism in the ITG turbulence. Nonlinear simulations of the TEM turbulence show that the main saturation mechanism is not the zonal flow but the inverse cascade of high to low toroidal harmonics. Further nonlinear simulations with various pressure profiles indicate that the ITG turbulence is more effective in driving heat conductivity, whereas the TEM turbulence is more effective for particle diffusivity.

In the second part of the thesis, global gyrokinetic simulations of electrostatic microturbulent transport for the experimental discharge of the LHD stellarator are carried out in the presence of boron impurity using GTC. The simulations show the co-existence of the ITG turbulence and TEM before and during boron powder injection. ITG turbulence dominates in the core, whereas TEM dominates near the edge, consistent with the experimental observations. Linear TEM frequency increases from ~ 80 kHz to ~ 100 kHz during boron injection, and the ITG linear frequency decreases from ~ 20 kHz to ~ 13 kHz, consistent with the experiments. The poloidal wave number spectrum is broad for both ITG: $0 - 0.5$ mm^{-1} and TEM: $0 - 0.25$ mm^{-1}. The nonlinear simulations with boron impurity show a reduction in the turbulent transport compared to the case without boron. The comparison of the nonlinear transport shows that the ion heat transport is substantially reduced in the region where the TEM is dominant. However, the average electron heat transport throughout the radial domain and the average ion heat transport in the region where the ITG is dominant are similar. The simulations with boron show the effective heat conductivity values qualitatively agree with the estimate obtained from the experiment.

In the third part of the thesis, global gyrokinetic simulations of the electrostatic microturbulence driven by the pressure gradients of thermal ions and electrons are carried out for the ADITYA-U tokamak geometry using its experimental plasma profiles and collisional effects. The dominant instability is TEM, based on the linear eigenmode structure and its propagation in the electron diamagnetic direction. Collisional effects suppress turbulence and transport to a certain extent. Simulations by artificially suppressing the zonal flow show that

the zonal flow is not playing a critical role in the TEM saturation, which is dominated by the inverse cascade. The frequency spectrum of the electrostatic fluctuations is in broad agreement with the experimentally recorded spectrum in the ADITYA-U, with a bandwidth ranging from ~ 0 to 50 kHz.

In the fourth part of the thesis, the global gyrokinetic simulations of the electrostatic microturbulent transport in the ADITYA-U tokamak are performed in the presence of argon impurity and radial electric field determined from the toroidal rotation. The dominant instability shares the features of ITG turbulence and TEM based on the direction of propagation and its response to the zonal flow. The radial electric field itself suppresses the turbulence and transport by changing the $\vec{E} \times \vec{B}$ shear, in agreement with the experimental observations. However, due to their low concentration, including argon ions in the gyrokinetic simulations does not affect the transport. A comparison of the simulations before and after argon puffing shows that the primary mechanism responsible for the reduction in transport is due to the change in plasma profile after argon puffing, which changes the linear instability drive due to the change in the profile gradient. Further simulation studies would be necessary to decipher the underlying mechanism for the change in plasma profile after argon puffing.

Finally, a novel framework is presented in the cylindrical coordinates to get rid of the difficulties of the null point (X-point), where the poloidal magnetic field vanishes, along with the singular behaviour of the safety factor and Jacobian in Boozer coordinates. This framework allows cross-separatrix coupling, which makes it feasible to carry out whole-volume gyrokinetic simulations of fusion plasmas.

To summarize, this thesis presents first-principles-based global gyrokinetic simulations of electrostatic microturbulence and the effects of impurities on the microturbulence in the LHD stellarator and ADITYA-U tokamak. These microinstabilities act as one of the dominant channels for the transport of particles and heat flux in fusion plasma, so their understanding and control are crucial for the viability of nuclear fusion.

List of publications

- **T. Singh**, J.H. Nicolau, Z. Lin, S. Sharma, A. Sen, A. Kuley, "Global gyrokinetic simulations of electrostatic microturbulent transport using kinetic electrons in LHD stellarator", *Nuclear Fusion*, Vol. 62, No. 12, 126006, Sept 2022 (https://doi.org/10.1088/1741-4326/ac906d).

- **T. Singh**, D. Sharma, T. Macwan, S. Sharma, J. Ghosh, A. Sen, Z. Lin, A. Kuley, "Gyrokinetic simulations of electrostatic microturbulence in ADITYA-U tokamak", *Nuclear Fusion*, Vol. 62, No. 5, 056008, Mar 2023 (https://doi.org/10.1088/1741-4326/acc344).

- **T. Singh**, J.H. Nicolau, F. Nespoli, G. Motojima, Z. Lin, A. Sen, S. Sharma, A. Kuley, "Global gyrokinetic simulations of electrostatic microturbulent transport in LHD stellarator with boron impurity" (under review in *Nuclear Fusion*).

- **T. Singh**, et al., "Gyrokinetic simulations of electrostatic microturbulence in ADITYA-U tokamak with impurity" (to be submitted to *Nuclear Fusion*).

- S. De, **T. Singh**, A. Kuley, J. Bao, Z. Lin, G.Y. Sun, S. Sharma, A. Sen, "Kinetic particle simulations in a global toroidal geometry", *Physics of Plasmas*, Vol. 26, Issue 8 , 082507, Aug 2019 (https://doi.org/10.1063/1.5108684).

Contents

List of Figures

List of Tables

Chapter 1

Introduction

1.1 Nuclear fusion

Tremendous efforts are going on worldwide to efficiently replicate the fusion reaction on Earth that powers our Sun and other stars in the universe [1]. In this reaction, two light nuclei fuse by overcoming the Coulomb barrier due to the strong gravitational pull of the massive star, forming the heavy nuclei with a little discrepancy in mass which is released as the energy according to Einstein's mass-energy relationship $E = mc^2$, where m is the difference in mass of product and reactant nuclei and $c = 3 \times 10^8$ m/sec is the speed of light. On Earth, one of the preferable reactions is governed by the fusion of deuterium (^{2}H) and tritium (^{3}H) [2], as shown in Fig. 1.1.

The mass discrepancy is released as 14.1 MeV of energy as the kinetic energy of the neutron (n), which is aimed to be harnessed by the fusion devices to generate electricity. The α-particle (^{4}He) released as a fusion product is targeted to self-sustain the fusion.

The so-called controlled thermonuclear fusion could be a viable source of unlimited and clean energy that can resolve the energy-related issues of the largest part of the world's population. This approach is beneficial as it could help achieve the net zero carbon emission goal, shifting the demand for non-renewable energy resources and negligible radioactive waste compared to fission reactors. In this direction, inertial confinement fusion (ICF) [3] and magnetic confinement fusion (MCF) [4] are the two major technologies used to achieve fusion. In ICF, the strong pulsed lasers are used (as one installed at National Ignition Facility, Lawerence Livermore National Laboratory, USA) to fuse the nuclei. However, MCF uses strong electromagnets to confine the fusion fuel.

Despite the science and engineering challenges and complexities of harnessing the power from nuclear fusion, recent research based on the two alterna-

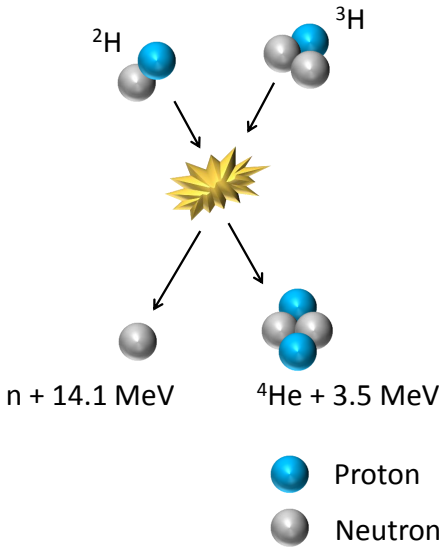

Figure 1.1 – Nuclear fusion reaction.

tives has shown encouraging results. The last years entitle the breakthroughs in fusion science from both ICF and MCF. For example, on 5th December 2022, NIF, USA achieved the first ignition and target gain > 1 [5]. The net gain was achieved by shining a laser with energy 2.05 MJ, resulting in 3.15 MJ of output fusion energy, with a gain of ~ 1.5. It breaks the earlier record by NIF, where they demonstrated the 1.3 MJ of fusion energy release with an input laser energy of 1.9 MJ. Alongside ICF, MCF has also picked up the pace in this direction. The JET fusion facility, housed at Culham Center for Fusion Energy in Oxford, UK, is one of the biggest fusion reactors based on MCF. On 21st December 2021, JET announced the production of 59 MJ of fusion energy during a 5 s pulse, breaking the 21.7 MJ of energy record in the 1997 campaign [6]. This increased time window over which the fusion is sustained will allow scientists to explore the crucial phenomena for sustainable fusion.

These breakthroughs have paved the attention of governments and several private sectors worldwide. For example, the US government invests $700 million per year in fusion energy. Last year it announced that $50 million would be delivered to private companies to help the private fusion start-ups to accelerate the commercialization of the nuclear fusion reactors [7]. Following the breakthrough at the JET fusion facility, the UK government has also agreed to provide £220 million for the first phase of the STEP project [8]. Similarly, the European Union delivers €679 million to EUROfusion through which the European countries collaborate [9]. Japan has always been a hub for fusion energy advancements competing world's fusion leaders. The Japanese govern-

ment spends tens of billions of Yen annually on international and domestic fusion projects. As a pacifist country, Japan has also reviewed some sensitive topics to keep pace with other countries [10]. In this quest, based on MCF, International Thermonuclear Experimental Reactor (ITER) will be the largest fusion reactor in the world to demonstrate the net gain with 500 MW of output power with 50 MW of input power, with an estimated funding of $\sim$ \$25 billion [11]. It is the largest collaborative project, including 35 nations, being constructed at Saint-Paul-lès Durance, France. Furthermore, it aims to sustain the fusion plasma pulse for $\sim$ 8 minutes and hence will prove the viability of nuclear fusion as a long-term energy source. Given this, the research in fusion science will enter a new era in the coming years.

1.2 Magnetic confinement fusion

In MCF, heating the neutral gas to the fusion temperature leads to the formation of plasma, which is used as the fusion fuel whose degrees of freedom are suppressed using the strong magnetic field. For instance, the unidirectional magnetic field along the axis of the cylinder confines the charged particle in a plane perpendicular to the magnetic field and make them gyrate along the magnetic field. However, the charged particles can still drift in the third direction. To suppress this third degree of freedom, the cylinder's two ends are combined to form a torus. Due to the geometrical effects and inhomogeneities in the magnetic field, the particles drift outward while moving across the torus, leading to the loss of plasma. To nullify this drift, the magnetic field lines are twisted in the toroidal direction by applying a magnetic field in a plane perpendicular to the toroidal direction, known as the poloidal plane. This twist in the magnetic field is represented in terms of safety factor q (or the rotational transform $\iota = 1/q$), which is the number of toroidal transits in one poloidal transit by a magnetic field line. These poloidal and toroidal components of the magnetic field are generated by different means. External coils generate the toroidal magnetic field, and the poloidal magnetic field is generated differently in tokamak and stellarator, which are two major alternatives to achieve fusion using MCF. In tokamak, the poloidal magnetic field is generated using plasma current in the toroidal direction. Whereas in the stellarator, the poloidal cross-section is rotated by modifying the design of external coils. Tokamak and stellarator are the two leading contenders in achieving nuclear fusion from toroidal burning plasma. Both of them have their advantages and disadvantages [12]. The following sections present a brief description of the tokamak and stellarator.

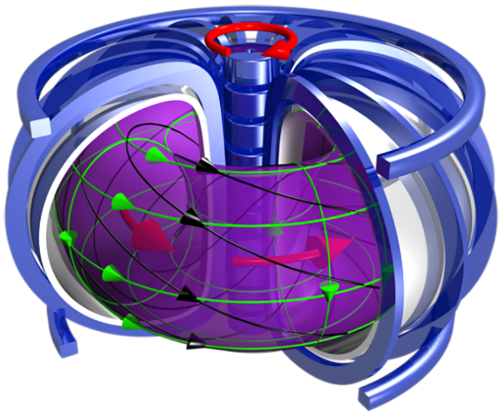

Figure 1.2 – Schematic of magnetic confinement fusion based on the tokamak. Source: Max Planck Institute for Plasma Physics, Germany.

1.2.1 Tokamak

Tokamak (with the Russian acronym: toroidal chamber with magnetic coils) is a torus-shaped axisymmetric device that uses strong electromagnets to confine the plasma [2]. It was conceptualized by two Russian scientists, Tamm and Sakharov, in 1952. Tokamak uses a central solenoid to generate the plasma current, generating the poloidal magnetic field. Whereas the external magnetic coils generate the toroidal magnetic field. Figure 1.2 shows the schematic of the tokamak fusion reactor. The central solenoid, shown by the blue column at the center, drives the plasma current, shown by big red arrows inside the vacuum vessel, that generates the poloidal magnetic field. The toroidal magnetic field is produced by the poloidal magnetic coils shown in blue. Over the magnetic flux surface shown by magenta, the toroidal and poloidal magnetic field lines are indicated by green arrows. Thus, the total magnetic field results from the toroidal and poloidal magnetic fields, as shown by black arrows, and is twisted around the torus to produce a rotational transform that cancels the radial drifts of plasma. Till now, a substantial amount of research has been carried out in tokamaks [13], and the design of the world's largest fusion reactor, ITER [11], is inspired by the existing tokamaks. Tokamak plasma is relatively easy to generate with good confinement properties; however, the need for transformer action to generate the current makes its operation pulsed [2]. In addition, the necessity of toroidal plasma current to produce the rotational transform makes the device more prone to current-driven instabilities.

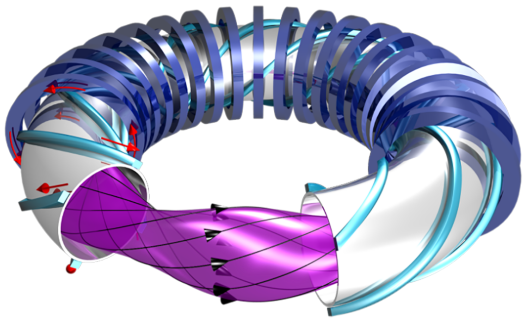

Figure 1.3 – Schematic of magnetic confinement fusion based on the stellarator. Source: Max Planck Institute for Plasma Physics, Germany.

1.2.2 Stellarator

Stellarator (Stella means star in Latin) is the non-axisymmetric counterpart of the tokamak [14], in which the rotational transform is produced by using a combination of helical, planar and non-planar magnetic coils instead of plasma current. It was first proposed by astrophysicist Lyman Spitzer from Princeton University in 1951. Figure 1.3 shows the schematic of a modern-day stellarator. In the figure, the toroidal magnetic field is generated by the magnetic coils in blue, and the rotational transform is produced by twisting the magnetic field lines using helical coils shown in coastal blue. The red arrows represent the direction of the current in the coils. The resulting magnetic flux surface is twisted, as shown in magenta. The magnetic field lines are drawn in black on the flux surface. Absence of toroidal plasma current leads to several benefits in stellarators in contrast to axisymmetric tokamaks. For example, it leads to steady-state operation of the device with the avoidance of disruptions, reduced MHD activities, lower levels of zonal flows, etc. [14–16], discussed in the following sections. However, these benefits come at the cost of toroidal symmetry breaking, leading to an increased neoclassical transport [14]. To mitigate these disadvantages, quasi-symmetry and quasi-isodynamicity concepts have been developed as further optimization of the stellarator configuration [17–19]. In contrast to quasi-symmetric stellarator, quasi-isodynamic stellarator has a unique property, due to which, in addition to the only dependency of the action integral of the bounce motion of trapped particles on the particle's radial position, the trapped particle orbits precess around the torus poloidally. Due to this, the trapped particle driven instabilities are stabilized over a large parameter space [20, 21]. Stellarator optimization, to reduce the neoclassical and turbulent transport, is gaining interest by tuning the 3D magnetic field configuration. One major challenge is constructing such a twisted magnetic field configuration with high precision. Due to the design complexities of the stel-

larator, the tokamak is considered the mainline magnetic fusion device. However, the stellarator has also gained considerable attention in recent years as a viable fusion reactor.

1.3 Major challenges

The science and engineering challenges are immense and huge on the path to viable fusion. In a tremendously complicated system like fusion reactors, finding the parametric dependence for the efficient fusion reaction is quite a non-trivial task. In this direction, J. D. Lawson, in 1955, found the criterion for the efficiency of the fusion, which is known as Lawson criterion [22] and later on modified to a more suitable quantity known as fusion triple product [23, 24], given by:

$$nT_i\tau_E > 5\times10^{21}\ \mathrm{m}^{-3}\ \mathrm{s\ keV}, \tag{1.1}$$

where n is the plasma density, T_i is the ion temperature, and τ_E is the energy confinement time. The precise value of the constant on right hand side depends upon the nature of n and T_i profiles and the use of average or peak values [2]. The parabolic profiles and peak values are used while writing Eq. 1.1. Fusion triple product is one of the most important quantities to measure the viability of nuclear fusion. Equation 1.1 means that not only should the plasma be hot enough for the fusion to occur, but it should also be sustained for a time long enough, along with the condition which dictates that a sufficient amount of fusion reactions are happening to exceed the net power gain of unity; $Q > 1$, where Q is the fusion power gain which is the ratio of power produced from fusion to the power used to heat the system.

Figure 1.4 shows the variation of fusion triple product with the ion temperature for various devices operated since 1960's and projected values for future reactors such as ITER. Till today, JT-60 has reported the highest fusion triple product of 1.5×10^{21} m^{-3} s keV [25]. TFTR and JET have also achieved the high fusion triple product of 7.9×10^{20} m^{-3} s keV [26] and 6.1×10^{20} m^{-3} s keV [27], respectively. This progress in fusion science has demonstrated the achievable reactor relevant parameters and allowed the physics understanding of the underlying processes governing the transport. The shaded blue region in the figure corresponds to ignition with $Q > 1.0$ for D-T fusion. So far, the breakeven $Q = 1.0$ (which represents the situation when the energy supplied to fuse the nuclei equals the energy released in fusion) has not been achieved yet, though the reactors such as TFTR and JET have come close to it with $Q = 0.27$ for TFTR in 1990's [28], and $Q = 0.64$ for JET in 1999 [29]. Future reactors like

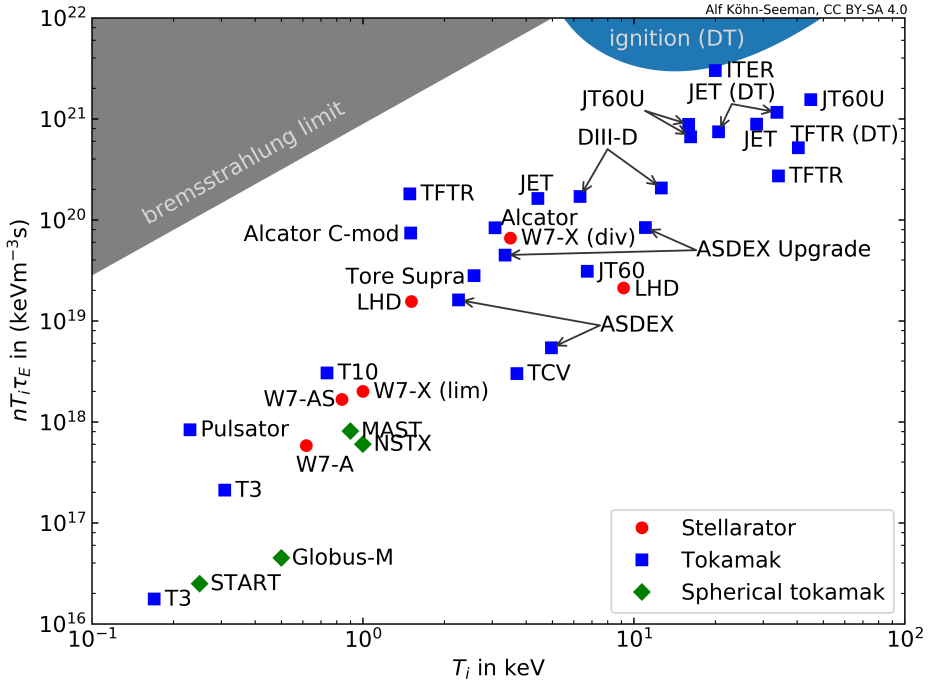

Figure 1.4 – Fusion triple product as a function of ion temperature for various fusion devices operated at different times. Source: Alf Köhn-Seeman.

ITER [30] and SPARC [31] are projected to surpass the breakeven and achieve ignition for the first time. The shaded region in gray corresponds to the undesired plasma cooling due to bremsstrahlung radiation and therefore is not suitable for fusion. The relevant information for the other fusion devices can be found in Ref. [32]. ITER is intended to demonstrate the viability of fusion with power gain $Q > 1$ along with the steady-state operation over ~ 1000 s. Following this, DEMO will be the first prototype commercial nuclear fusion reactor and successor of ITER, with a power gain of $Q = 25$ and is supposed to be fully operational by 2050 [33].

On the journey to the commercialization of nuclear fusion reactors, hurdles and knowledge gaps will be overcome and filled over time with the continuous efforts happening worldwide. The following are the major challenges:

1.3.1 Design considerations

In fusion reactors, the plasma temperature is quite high, and the particles have radially outward drifts due to the various transport processes. In addition to this, energetic particles such as α-particles produced during fusion exhibit MeV of kinetic energy and hit the plasma-facing components such as the divertor and cause damage. Several strategies have been proposed to mitigate the damage caused by the energetic particles and reduce the heat load at the

divertor plates. However, it requires the development of advanced materials to sustain the heat load on walls [34]. Furthermore, designing magnetic coils with high precision is quite challenging. In particular, a great deal of complexity is involved in designing the magnetic coils of stellarators. This is one of the major reasons the fusion research on stellarators was in the dark for a long time. However, recent research has shown the alternatives to simplify the designs of magnetic coils using permanent magnets [35].

1.3.2 MHD activities

Magnetohydrodynamics (MHD) instabilities are one of the major candidates for the transport in the present-day fusion devices, limiting their operation for the viable fusion [2]. Therefore, it is always desired that the plasma is MHD stable at high values of β, where β is the ratio of kinetic pressure to magnetic pressure. The high β plasma also provides a driving force for the MHD instabilities. However, due to economic constraints, the fusion reactors must operate at high β values, thus making the fusion plasma inherently unstable. In their simplest form, these large-scale instabilities are described by the MHD equations. They are mainly excited by the gradients in plasma current and plasma pressure and are termed as kink modes and ballooning modes, respectively. These instabilities could be stabilized by plasma compression, bending, and compression of magnetic field lines, which is a subject of plasma shaping [36]. Furthermore, macroscale instabilities called Alfvén eigenmodes are driven unstable by the energetic particles used to heat the plasma to the fusion temperatures [37]. These instabilities lead to a loss of energetic particles and α-particles produced during fusion before they deliver their energy to the plasma. The loss of energetic particles also leads to localized heating of plasma-facing components, thus degrading the device's performance.

1.3.3 Disruptions

The disruptions are the instabilities that lead to the sudden and violent loss of plasma confinement [38]. They correspond to the worst events that can occur in tokamaks as they lead to an intense mechanical stress and heat load on the walls, due to which the plasma discharge collapses abruptly [39]. Disruptions affect the tokamak operation by imposing limits over the maximum achievable density, β value, and low-q current. Disruptions are phenomenological rich and are caused by multiple reasons. From the instability point of view, tearing modes and magnetic islands play a vital role in their occurrence. Fundamentally, these instabilities and hence the disruptions are driven unstable by the

toroidal currents, one of the key components of tokamaks to generate the rotational transform. In this context, stellarators are advantageous due to the absence of toroidal plasma current. For the safe operation of fusion reactors, mitigating or reducing their impact on the device is necessary. To reduce the mechanical and thermal load on the walls during disruptions, neutrals are injected, leading to the radiative cooling of the plasma [40]. This process converts most of the plasma energy into electromagnetic radiation and thus lowers the damage to the walls. Recent advances in machine learning-based approaches have opened new avenues for the real-time avoidance of disruptions [41].

1.3.4 ELMs

The discovery of high confinement mode (H-mode) in tokamaks has played an important role in advancing progress in fusion science. It was invented in ASDEX tokamak in the early 1980's during the heating experiments with neutral beam injection (NBI) [42]. During the H-mode operation, the energy confinement time increases by almost twice. H-mode arises in the plasma due to the creation of a transport barrier at the plasma edge with steep profile gradients, known as pedestal, which limits the radial outward flux of heat and particles. Therefore, it will be the default operational mode for future reactors such as ITER. Along with the H-mode discovery, different diagnostics have shown a new type of instability near the plasma edge, called edge localized modes (ELMs). During the onset of ELMs, the stored energy in the plasma is expelled out with short and sudden bursts of particles within a few hundred microseconds or even lesser. These bursts cause severe damage to the walls of the container and hinder the plasma operation. Even in their weakest form, ELMs lead to the erosion of impurities from the walls that diffuse inside the core and cool the plasma by diluting the fuel. Considerable research has been done to understand and control ELMs [2]. Recent experiments in EAST tokamak have shown the suppression of ELMs during the injection of impurities and have access to the H-mode of plasma [43].

1.3.5 Microturbulence

In fusion reactors [2, 4], the energy and particle confinement times must be long enough to achieve a net energy balance between the energy supplied to heat the system and the energy produced by the fusion process in the plasma. The energy and particle losses observed in magnetic fusion experiments are significantly higher than predicted values for the collisional processes [44]. This so-called anomalous transport is believed to be primarily due to small-scale

instabilities called micro-instabilities caused by the temperature and density gradient of plasma species [45]. These micro-instabilities are the drift wave instabilities, the wave-like fluctuations of the electric field, density, and temperature that move along the poloidal direction, driven unstable by the plasma drifts [46]. These fluctuations cause a significant energy release mechanism for the free energy stored in the pressure gradient in the confined plasma [45]. In simple terms, the gradient in the plasma profile acts as a source of available free energy for the turbulence to rise; for example, ion temperature gradient (ITG) turbulence [47] is driven unstable due to a gradient in ion temperature. Even the trapped particle orbits about the magnetic field lines can excite some of the turbulences in the presence of drive; for example, trapped electron mode (TEM) [48] is excited in fusion plasmas due to the population of trapped electron orbits and the existence of a gradient in electron density and/or electron temperature. Unlike ITG turbulence, TEM requires the resonant interaction of trapped electrons with drift wave. Fluctuations in the presence of drive cause $\vec{E}\times\vec{B}$ drift of the plasma particles, leading to turbulence. In addition, due to the nature of magnetic drifts and trapped electron orbits in the toroidal geometry, the magnetic field curvature defined as $\vec{\kappa} = \left(\hat{b}\cdot\nabla\right)\hat{b}$ plays an essential role in the growth of microturbulence, where $\hat{b}$ is the unit vector along the magnetic field. For example, ITG and TEM driven turbulence in tokamaks are unstable on the outboard side where the curvature is bad ($\kappa < 0$) [45]. Furthermore, microturbulence excites poloidally and toroidally symmetric structures with a variation in the radial direction called zonal flow. Zonal flow and microturbulence are universal aspects of drift wave instability [49]. The $\vec{E}\times\vec{B}$ shear caused by zonal flow plays a vital role in regulating the turbulent transport in fusion plasmas.

1.4 Microturbulence in fusion plasmas

Microturbulence is an extensively studied subject in fusion research [45]. It is one of the major concerns for the viable operation of fusion devices due to its multi-physics and multi-scale nature. It is highly accepted in the fusion community that ITG and TEM driven turbulences play a crucial role in transporting the heat and particle fluxes on ion scales [45]. The design of future reactors relies on the extrapolation of the turbulent transport levels from past and current fusion experiments to much larger future experiments such as ITER [11, 30]. Therefore, it is essential to review the various fusion devices and microturbulence investigations, which are described as follows:

1.4.1 JT-60

Japan Torus-60 (JT-60) is an advanced tokamak operated by Japan Atomic Energy Agency since 1985, in Japan and recently has been upgraded to the "super advanced" JT-60SA [50]. As of 2018, JT-60 entitles the highest achieved fusion triple product of 1.5×10^{21} m^{-3} s keV [25]. It is designed to assist the optimized operation of bigger reactors such as ITER by overcoming the physics and engineering challenges [51]. Investigating the physics of microturbulent transport and their control are the major research plans of JT-60SA for improved plasma confinement [52, 53]. In this direction, PCI diagnostic has been designed in JT-60SA for core fluctuation measurements on the ion scale turbulence such as ITG/TEM that is a major cause of anomalous transport [54].

1.4.2 JET

Joint European Torus (JET) is one of the world's largest tokamak-based fusion reactors, operational since 1983 in Culham Center for Fusion Energy, UK. JET has played a significant role in demonstrating the attainability of reactor-relevant parameters [55]. However, turbulence fluctuations have been found in various diagnoses in JET experiments. For example, the turbulent transport analysis of JET H-mode has shown the dominance of ITG instability [56]. Recent investigations on JET experiments have also shown the nonlinear electromagnetic suppression of microturbulence driven by ITG turbulence using the fast ion drive [57]. Furthermore, the power scan studies in JET exhibit a transition from ITG to kinetic ballooning mode (KBM) instability. During the L-H transition, the reduced core microturbulence amplitude has been seen along with the suppression of edge microturbulence [58].

1.4.3 EAST

Experimental Advanced Superconducting Tokamak (EAST) is the first tokamak to use superconducting magnets [59]. It is housed in Hefei, China. Operating since 2006, EAST has already made significant contributions towards the long-term goals of future fusion reactors such as ITER. For example, the change in microturbulence activity followed by the L-H transition is poorly understood. In this direction, EAST experiments have measured the characteristics of core microturbulence during the L-H transition [60]. Similarly, the nonlinear coupling of MHD mode and microturbulence is studied in EAST [61], and the effect of 2/1 classical tearing mode on microturbulence has been investigated in the core of L-mode discharge of EAST [62]. Improved plasma confinement is

recently achieved in EAST over ~ 1000 s in a new self-organizing, high confinement regime called Super I-mode [63].

1.4.4 DIII-D

DIII-D is the tokamak designed to operate at high β values with strongly shaped plasma. Since 1980's, it has been operated by General Atomics, San Diego, US. Several experiments in DIII-D have witnessed the existence of microturbulence. For instance, the analysis of density and temperature fluctuations measurements has shown the signatures of ITG and/or TEM turbulence in the L-mode discharge of DIII-D [64, 65]. To optimize the energy and particle confinement in DIII-D, the impurity seeding experiments have been performed and have shown improved confinement due to the suppression of core turbulence and transport [66]. Recent results in DIII-D have found that in addition to the anomalous transport, microturbulence can also lead to the regulation of low frequency Alfvén waves [67]. Furthermore, the L-H transition causes a considerable decrease in radial correlation length as well as the amplitude of microturbulence due to the onset of the strong radial electric field in the edge transport barrier and hence an increased $\vec{E} \times \vec{B}$ shear [68]. DIII-D has also accessed the high performance Super-H mode, where the turbulent transport leads to increased core temperature and pressure with the increased pedestal height [69].

1.4.5 ADITYA-U

ADITYA-U is the first Indian tokamak housed in Institute for Plasma Research, India. It is a medium-sized, air-core tokamak that has recently been upgraded from the ADITYA tokamak [70–73] to incorporate a new set of divertor coils for shaped plasma operations with a new vacuum vessel along with a new toroidal belt limiter. Since its commissioning, several experiments relevant to the operation of future fusion devices such as ITER have been performed [71–73], including experiments on generation, transport, and control of runaway electrons [72, 73], plasma disruption [72, 73], transient transport phenomena such as cold-pulse propagation [73, 74] and plasma detachment [73]. Edge region in ADITYA-U is thoroughly diagnosed using various probes and signatures of MHD modes, and turbulence-induced fluctuations have been investigated [73]. These fluctuations are found to be suppressed due to argon gas puffing.

1.4.6 W7-X

Wendelstein 7-X (W7-X) is the world's largest stellarator at Max Planck Institute for Plasma Physics, Greifswald, Germany, built in 2015. Stellarators have the advantages over their axisymmetric counterparts, tokamaks, due to the absence of disruptions, lower levels of MHD activities, and steady-state operation [14–16]. However, these benefits come at the cost of toroidal symmetry breaking that leads to an increased neoclassical transport and stronger damping of zonal flows as compared to the axisymmetric tokamaks [75, 76]. W7-X is an quasi-isodynamic stellarator which has been optimized by reducing the neoclassical transport to an advanced stellarator [19]. Even in the neoclassically optimized W7-X, the core plasma fluctuations measured using PCI diagnostics show evidence of microturbulence [77]. Recent impurity injection experiments in W7-X have shown improved plasma confinement through the profile change [78]. During the periods of enhanced confinement, an attenuation in the turbulence fluctuations has been observed. The reduction in the transport is due to the change in plasma profile that changes the profile gradient and the intensity of the turbulence structures. Recently, W7-X has set a new record by maintaining the hot plasma for ~ 8 minutes [79].

1.4.7 LHD

Large Helical Device (LHD) is the world's second largest superconducting stellarator after W7-X, currently operational at the National Institute of Fusion Science, Japan. LHD employs a heliotron magnetic field originally developed in Japan to produce the quasi-symmetry. Being a stellarator, the transport in LHD is dominated by the neoclassical processes, which is reduced by finding a magnetic configuration with a reduced neoclassical transport due to the strong inward shift of the magnetic axis [80]. Even after the neoclassical optimization in LHD, transport due to microturbulence remains a major challenge. For example, characteristic signatures of the ITG turbulence [81–84] have been observed in the LHD. Towards controlling the turbulent transport, recent impurity injection studies in LHD have shown encouraging results [85, 86]. In particular, access to a reduced-turbulence improved confinement regime has been observed upon the injection of boron powder into the plasma [86]. Following this, LHD has also demonstrated significant progress towards the feasibility of proton-boron fusion as an alternative to the mainstream D-T reaction [87].

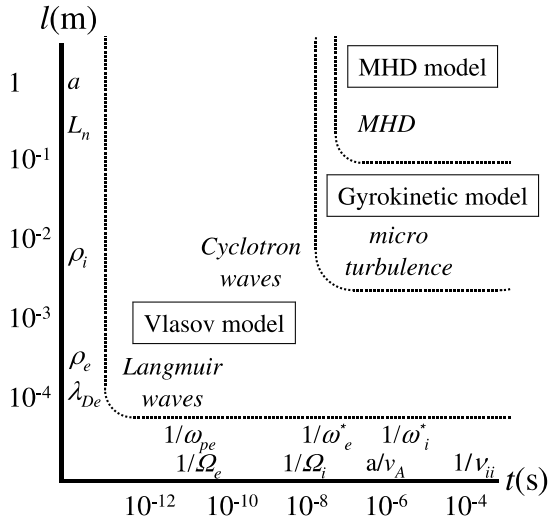

Figure 1.5 – Representation of range of spatio-temporal scales in fusion plasmas and applicability of various models. Here, λ_{De} is the Debye length, ρ_α is the gyroradius, L_n is the scale length of the plasma density profile at equilibrium, a is the size of the plasma, ω_{pe} is the frequency of plasma oscillation, ω^*_α is the diamagnetic rotation frequency, Ω_α is the cyclotron frequency, v_A is the Alfvén velocity, ν_{ii} is the ion-ion collision frequency, and α is the plasma species. Source: Ref. [88].

1.5 Gyrokinetic framework

Microturbulence is the key problem in fusion reactors, limiting their performance. Understanding and controlling turbulence and transport remains a serious challenge. Various analytical, numerical, and experimental studies have been performed in this attempt. Developing the gyrokinetic framework has been an important step. This section briefly describes the gyrokinetic framework and various approaches for the in-depth study of turbulence and transport in fusion plasmas.

Fundamentally, the plasma dynamics are complicated due to the co-existence of multiple spatial and temporal scales that represent the different physics aspects of the problem, as shown in Fig. 1.5. This poses great challenges in describing the microturbulence in plasma using various physical models. To avoid these difficulties nonlinear gyrokinetic model [49] solves the Vlasov-Maxwell system of equations by suppressing the phenomena evolving at time scales smaller than $\sim 1/\Omega_\alpha$ where $\Omega_\alpha = Z_\alpha B/m_\alpha c$ is the cyclotron frequency of the plasma species, m_α is the mass, Z_α is the charge, and B is the magnetic field strength.

In the early days of gyrokinetic formulation, the recursive method [49] was used for the gyro-averaging of the Vlasov equation; however, the modern gyrokinetics [89] uses the guiding center transform, which is based on the La-

grangian or Hamiltonian formulation [90, 91]. Though the gyrokinetic Vlasov-Maxwell equations correctly describe low frequency drift waves in plasma, it is still a numerically complicated and computationally expensive task for an accurate representation of microturbulence in the non-trivial magnetic confinement configuration. For this, various numerical models have been developed to serve the purpose. So far, three numerical approaches have been developed to solve the underlying gyrokinetic equations and are discussed below:

1.5.1 Lagrangian approach

Lagrangian approach is often referred to PIC (particle-in-cell) method [92], in which the plasma distribution is initialized by the marker particles in 5D phase space, following pushing the particle orbits and evaluating the source terms for the field equations at every time step. Several codes have been developed on the basis of the Lagrangian-PIC approach, for example, GTC [93], ORB5 [94], GTS [95], GT3D [96] etc. A delicate issue faced by this approach is the significant growth of noise over the simulation time due to the marker particles, which leads to the incorrect estimation of turbulent transport level. Noise control is also crucial for accurately representing important physical quantities such as zonal flow. Based on the nature of turbulence, several filtering techniques have been incorporated into the simulations; one such example is magnetic field-aligned Fourier filtering [94]. For further noise control, the low noise method [97] is used in which, instead of evolving the full plasma distribution, only the perturbed part of the distribution is evolved over time.

1.5.2 Eulerian approach

Eulerian approach is also referred to as the Vlasov approach. In contrast to the Lagrangian approach, the Eulerian approach does not suffer from the sampling noise of marker particles. However, it is prone to Courant-Friedrichs-Lewy (CFL) stability condition [98] due to explicit time integration, which puts an upper bound on the time step size as a function of spatial resolution of computational grids. Various gyrokinetic codes make use of the Eulerian approach, such as GS2 [99, 100], GKV [101], GKW [102], GYRO [103], GENE [104], and GT5D [105]. To overcome the CFL constraint, implicit or semi-implicit schemes have been proposed for time integration [105]. Moreover, the Eulerian approach benefits from a physically precise and numerically stable description of $\vec{E} \times \vec{B}$ nonlinearity. In the local (flux-tube) codes such as GKV and GS2, such things are easily taken care of by anti-aliasing and Fourier methods in the spectral domain; however, this approach cannot be used in global codes.

1.5.3 Semi-Lagrangian approach

Due to the inherent limitations of both Lagrangian and Eulerian approaches, a third approach, known as the semi-Lagrangian approach, has been discussed that benefits from the former ones [106–108]. In particular, it combines the characteristics of the Lagrangian approach to eliminate the CFL constraint and the use of the Eulerian grid to eliminate the sampling noise inherent in the Lagrangian approach. However, in gyrokinetic codes based on the semi-Lagrangian approach such as GYSELA [108], the potential is extremely sensitive to errors in particle conservation. Also, multi-dimensional interpolation is a tedious task for which split operator based methods are used in the semi-Lagrangian approach.

1.6 Motivation

Tokamak and stellarator are two leading contenders in the quest to achieve nuclear fusion from toroidally burning plasmas. They have their pros and cons. Out of all the transport processes discussed in this chapter that contribute to the loss of heat and particle fluxes from the fusion reactors, microturbulence plays an important role. It hence limits the operation of the device for useful fusion. Therefore, their complete understanding and control are vital for the viability of nuclear fusion.

Recent research in stellarator and tokamak has shown encouraging results. In the experiments, signatures of ITG and TEM turbulence have been found using the PCI diagnostics in W7-X and LHD stellarators [77, 81–84], and tokamaks [64, 65, 109], and are shown to pose a significant challenge by limiting their performance. Towards the understanding of turbulent transport, gyrokinetics is as a novel framework to simulate microturbulence in fusion plasmas. However, gyrokinetic simulations of microturbulence in stellarators impose a serious challenge due to the 3D structure of the magnetic field, in contrast to the axisymmetric tokamak. Over the past few years, sufficient progress has been made toward gyrokinetic simulations of microturbulence in stellarators. Gyrokinetic flux-tube simulations using GKV code have been carried out extensively in the LHD [110–112], where the reduction of the ITG turbulence due to zonal flow, the role of the zonal flow on the TEM turbulence, and the effects of isotopes and collisions on the microinstabilities in the LHD have been studied. However, the flux-tube simulations do not capture the linear coupling of multiple toroidal harmonics due to the 3D structure of the magnetic field in the stellarators and the secular radial drift of helically trapped particles across flux surfaces. Hence, a global gyrokinetic simulation study is required to better un-

derstand the microturbulence in the stellarators. The first global gyrokinetic simulations using the EUTERPE code with adiabatic electrons were recently carried out to study the effects of the radial electric field on the ITG turbulence in W7-X and LHD [113]. The gyrokinetic toroidal code (GTC) has been used to carry out the first global nonlinear ITG turbulence simulations with adiabatic electrons in the W7-X and LHD [114]. GTC has also self-consistently calculated neoclassical ambipolar radial electric fields in the W7-X, which is shown to suppress the ITG turbulence more strongly in the electron-root case than the ion-root case [115]. Furthermore, XGC-S [116] and GENE-3D [117] have performed global gyrokinetic simulations of microturbulence in the W7-X using adiabatic electrons. The adiabatic electron model cannot address the effect of kinetic electrons on the ITG turbulence [118, 119], and the excitation of the TEM turbulence [120]. Therefore, it is important to carry out the global simulations study of electrostatic microturbulence in stellarators.

Impurities in tokamak and stellarator can significantly impact the plasma confinement, depending upon their concentration. In general, impurity seedings in present-day fusion devices have improved plasma discharge in several ways. For example, neon seeding in DIII-D tokamak has led to the suppression of the core turbulence [66], boron powder injection in LHD has resulted in the region of reduced turbulent transport [86], boron and/or lithium powder injection in EAST [43], NSTX [121], and KSTAR [122] has resulted in the suppression of ELMs, and wall-conditioning methods in DIII-D [123], ASDEX [124], EAST [125], NSTX-U [126] have resulted in the beneficial plasma-material interface. Furthermore, an excess concentration of impurities can lead to even degradation of plasma confinement and can cause a radiative collapse of the discharge. However, a controlled injection of impurities can improve the plasma confinement by reducing the microturbulent transport [66]. In this direction, recent impurity injection studies in the stellarators LHD [85, 86] and W7-X [78] have shown encouraging results. In particular, in LHD, the access to a reduced-turbulence improved confinement regime has been observed upon the injection of boron powder into the plasma [86]. Here, the plasma temperature is observed to increase by about 25%. At the same time, the amplitude of turbulent fluctuations has been measured to decrease up to a factor of two over a broad region of the plasma volume. The reasons behind the confinement improvement are not fully understood yet, and dedicated gyrokinetic simulations can shed light on the matter. Therefore, global gyrokinetic simulations of electrostatic microturbulence need to be carried out for the realistic experimental discharge of LHD stellarator with boron impurities.

Microturbulence is extensively studied in tokamaks. However, in ADITYA-

U, there are very few simulation studies, and most importantly, the global gyrokinetic simulations of microturbulence using state-of-the-art codes such as GTC still need to be reported. Therefore, on the similar line of discussion, to understand the transport processes in ADITYA-U, global gyrokinetic simulations of electrostatic microturbulence need to be performed in ADITYA-U. Recently, argon gas puffing experiments have been performed in ADITYA-U, and an improvement in plasma confinement has been observed. To investigate the underlying mechanism in the plasma confinement enhancement in ADITYA-U, electrostatic microturbulent transport simulations need to be performed in the presence of impurities.

Furthermore, most gyrokinetic codes are based on their formulation in the magnetic coordinates that can only simulate the physics in the core region. However, the open field-line region, called scrape-off layer (SOL), can significantly affect the plasma confinement [127]. To understand the plasma processes in the SOL region, a new formulation is required for the whole-volume plasma simulations. For this, the gyrokinetic codes can be formulated in the cylindrical coordinates that allow the cross-separatrix coupling.

Overall, the first-principles-based global gyrokinetic simulation studies in tokamak and stellarator will not only help to validate the gyrokinetic simulation model as the accurate description of the fusion plasmas but will also help to gain an in-depth understanding of the underlying physics mechanism behind the observed transport and its control for better plasma confinement.

1.7 Outline of thesis

Finally, this chapter is concluded by outlining the work presented in the rest of the thesis as follows:

Chapter 2

In Chapter 2, the gyrokinetic simulation model implemented in GTC is presented. As this thesis presents the electrostatic microturbulence study in the fusion plasma, the electrostatic microturbulence formulation of GTC is discussed in this chapter. A brief overview of each module, such as particle equations of motion, field solver, and calculation of the fluctuation quantities, such as density and electrostatic potential, is described. Gyrokinetic formulation of plasma with the third species as impurity ions is also described, along with the thermal ions and kinetic electrons.

Chapter 3

In Chapter 3, the global gyrokinetic simulations of the electrostatic microturbulent transport using kinetic electrons are carried out in the LHD stellarator. The kinetic electrons are introduced using the fluid-kinetic hybrid model, well-benchmarked in GTC. The pure ITG and TEM turbulences are simulated by exciting a gradient in ion temperature and plasma density, respectively. ITG turbulence simulations are carried out using the adiabatic and kinetic electron models. The kinetic electron effects increase the growth rate of the turbulence by more than 50% and more than double the transport levels compared with simulations using adiabatic electrons. The role of zonal flow in suppressing turbulent transport is also discussed by artificially suppressing it. Zonal flow dominates the saturation mechanism in the ITG turbulence. Linear simulations of the TEM turbulence show that the eigenmode structure lies at the outer midplane where the curvature is bad, just like ITG turbulence. Nonlinear simulations of the TEM turbulence show that the main saturation mechanism is not the zonal flow but the inverse cascade of high to low toroidal harmonics. Further nonlinear simulations with various pressure profiles indicate that the ITG turbulence is more effective in driving heat conductivity, whereas the TEM turbulence is more effective for particle diffusivity.

Chapter 4

In Chapter 4, global gyrokinetic simulations of electrostatic microturbulent transport for the experimental discharge of the LHD stellarator are carried out in the presence of boron impurity using GTC. The simulations show the co-existence of the ITG turbulence and TEM before and during boron powder injection. ITG turbulence dominates in the core, whereas TEM dominates near the edge, consistent with the experimental observations. Linear TEM frequency increases from ~ 80 kHz to ~ 100 kHz during boron injection, and the ITG linear frequency decreases from ~ 20 kHz to ~ 13 kHz, consistent with the experiments. The poloidal wave number spectrum is broad for both ITG: $0-0.5$ mm^{-1} and TEM: $0-0.25$ mm^{-1}. The nonlinear simulations with boron impurity show a reduction in the turbulent transport compared to the case without boron. The comparison of the nonlinear transport shows that the ion heat transport is substantially reduced in the region where the TEM is dominant. However, the average electron heat transport throughout the radial domain and the average ion heat transport in the region where the ITG is dominant are similar. Furthermore, the simulations show the effective heat conductivity values qualitatively agree with the estimate obtained from the experiment.

Chapter 5

In Chapter 5, the first-principles global gyrokinetic simulations of the electrostatic microturbulence driven by the pressure gradients of thermal ions and electrons are carried out for the ADITYA-U tokamak geometry using experimental plasma profiles with collisional effects. The dominant instability is determined to be TEM based on the linear eigenmode structure and its propagation in the electron diamagnetic direction. The collisional effects suppress the turbulence and transport to a certain extent. The turbulent transport level of ion diffusivity determined by the nonlinear simulations matches well with the experimentally measured value of ~ 0.2 m^2/sec. The electron heat diffusivity estimated from the experimentally measured energy confinement time is within 20% of the simulated value of ~ 1.2 m^2/sec. Further nonlinear simulations by artificially suppressing the zonal flow show that the zonal flow is not playing any crucial role in the turbulence saturation, while the inverse cascade of the higher poloidal and toroidal modes to the lower one dominates the nonlinear saturation. The frequency spectrum of the electrostatic fluctuations, with broadband from ~ 0 to 50 kHz, also agrees with the experimentally recorded spectrum in ADITYA-U.

Chapter 6

In Chapter 6, global gyrokinetic simulations of the electrostatic microturbulent transport in the ADITYA-U tokamak are performed in the presence of argon impurity and radial electric field determined from the toroidal rotation. The dominant instability shares the features of ITG turbulence and TEM based on the direction of propagation and its response to the zonal flow. The radial electric field suppresses turbulence and transport by enhancing the $\vec{E} \times \vec{B}$ shear. However, due to their low concentration, including argon ions in the gyrokinetic simulations does not affect the transport. A comparison of the simulations before and after argon puffing shows that the primary mechanism responsible for the reduction in transport is due to the change in plasma profile after argon puffing, which changes the linear instability drive due to the change in the profile gradient. Further simulation studies would be necessary to decipher the underlying mechanism for the change in plasma profile after argon puffing.

Chapter 7

In Chapter 7, a significant enhancement of GTC called the global toroidal code using the X-point (GTC-X) is presented by developing a new global nonlinear particle simulation model that couples the tokamak core and SOL regions. A guiding center pusher has been implemented to simulate the low frequency drift wave instabilities such as ITG. In contrast to the finite difference scheme, which looses its capabilities at the magnetic axis and X-point, a finite-element-based field solver is incorporated in GTC-X for the whole-volume gyrokinetic simulations of fusion plasmas. A new particle-grid interpolation is implemented that uses interpolation along the magnetic field lines to calculate the fluctuating quantities on the simulation grid points. GTC-X is benchmarked by performing self-consistent simulations of zonal flow using the low noise δf method in the core of a tokamak.

Chapter 8

In Chapter 8, the conclusions are made based on the work presented in this thesis. As a future work, several possible research directions are motivated relevant to the progress towards understanding and controlling the turbulent transport in the fusion plasmas.

Chapter 2

Gyrokinetic toroidal code

2.1 Introduction

It is highly accepted in the fusion plasma community that the electrostatic micro-instabilities such as ion temperature gradient (ITG) and trapped electron mode (TEM) driven instabilities are one of the dominant channels for the particle and heat transport in fusion plasmas [45]. Therefore, their understanding is of vital importance for the viability of fusion. Recent advancements in numerical techniques and high-performance computing have proved that gyrokinetics accurately describes the microturbulence in plasmas [64, 65]. Given this, it has become feasible to validate the various plasma models using state-of-the-art numerical modeling. One of the main objectives of gyrokinetic modeling is to extrapolate the turbulent transport in future reactors such as ITER from the simulated transport levels in the past and present-day fusion reactors [128]. Such empirical scaling will ease the design of upcoming reactors for viable fusion.

Depending upon the model equations being simulated, gyrokinetic codes are kept into three categories: Lagrangian, Eulerian, and semi-Langrangian. All of these approaches have their inherent advantages and disadvantages. The gyrokinetic codes such as GTC [93], and ORB5 [94] are based on the Lagrangian approach representing the plasma by a finite number of marker particles. To reduce the particle noise due to Monte Carlo sampling of phase space, these codes use the δf scheme [97]. The gyrokinetic codes GENE [104], GKV [101], and GYRO [129] are based on the Eulerian approach. This method uses the time-stationary phase space mesh to discretize the Vlasov equation. Whereas the semi-Lagrangian approach-based codes such as GYSELA [108] combine the benefits of both the Lagrangian and Eulerian approaches with a suitable phase space description and enhanced numerical stability.

In addition to micro-instabilities, processes evolving at long time scales,

such as energetic particle confinement times, must be adequately understood. Both full-f and δf methods require noise control techniques to simulate such processes. In contrast to the δf method, full-f method does not rely on decomposing the equilibrium and fluctuations. Therefore, it is an obvious way to handle substantial changes in the plasma profile during the simulations. However, the full-f approach is more expensive and requires noise reduction schemes for the feasibility of simulations, specifically in the MHD limit. Though the δf method has better control over the noise due to the marker particle sampling, it still requires some noise reduction schemes for the Alfvén eigenmodes and energetic particle physics simulations, which is a topic of great interest [130].

Gyrokinetic toroidal code (GTC) is a fully nonlinear, Lagrangian-based particle-in-cell (PIC) code used to study the physics of microturbulent transport [120, 131], Alfvén waves [132], radio frequency waves [133], and energetic particles [134] in fusion plasmas. It has been applied to several different geometries, for example, tokamaks (DIII-D [131], ADITYA-U [135], EAST [136]) and field reversed configuration (FRC) [137] to simulate the plasmas. GTC has undergone continuous development for the past two decades to enhance its capabilities. Recently, GTC has been upgraded to study the micro-instabilities in 3D devices called stellarators [114]. Being a Lagrangian approach-based PIC code, GTC is prone to sampling noise of marker particles. For a better single-to-noise ratio, GTC uses the low noise δf method [97]. GTC is formulated in magnetic coordinates and uses field-aligned mesh to describe the fluctuating quantities, providing maximum numerical stability and computational efficiency without compromising any physics due to geometry approximation. GTC has been optimized for enhanced performance on the advanced computing architectures [138, 139].

The rest of the chapter presents the physics and simulation model used in GTC to simulate the electrostatic microturbulent transport in fusion plasmas.

2.2 Particle-in-cell simulations

GTC is the state-of-the-art global gyrokinetic code based on the particle-in-cell (PIC) algorithm as shown in Fig. 2.1 to solve the governing Vlasov-Maxwell system of equations. In the PIC cycle, the phase space distribution of the plasma species is initialized. Spatially, the marker particles representing the plasma are loaded uniformly, and a Maxwellian distribution is used in the velocity space. In GTC, a spatial mesh represents the dynamical quantities such as electromagnetic field quantities and density fluctuations. Given the initial positions and velocities, the equations of motion are integrated. From the up-

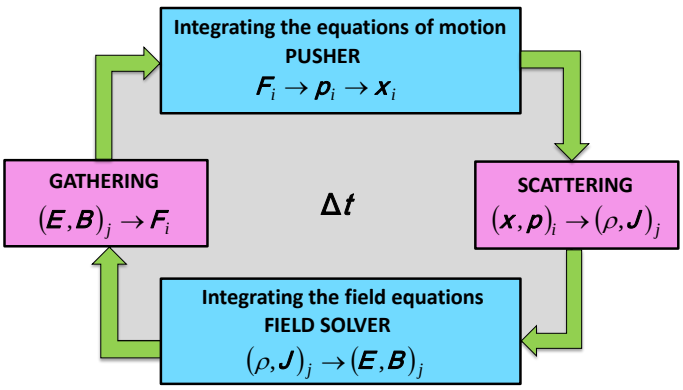

Figure 2.1 – Particle-in-cell algorithm. i and j are associated with the particle and grid indices, respectively.

dated positions and velocities, the density and current are calculated using the scattering operation on the spatial network of grids. These quantities are then used as the source terms for Poisson and Ampere equations, which are solved on the spatial grids to obtain the electromagnetic field. These field quantities are then gathered back to the particle position to integrate the equations of motion at the next time step. This cycle is repeated to obtain the self-consistent electromagnetic fields resulting from the plasmas.

2.3 Gyrokinetic theory

With the advancements in high-performance computing (HPC), it is now feasible to carry out large-scale particle simulations of fusion plasma with realistic parameters. However, to simulate the turbulences arising from the drift waves, it is crucial to resolve the fast cyclotron motion of the electron. It puts a constraint on the time step size, which must be sufficiently small to resolve 'ω_{H}' mode [140], where ω_H is the frequency of electrostatic shear-Alfvén wave. Gyrokinetic is a framework in which the fast cyclotron motion is averaged out, leading to the reduction of dimensionality of the system from 6D to 5D. It is important to note that finite Larmor radius (FLR) effects are recovered by reproducing the charge ring moving along with the particle over which the charge is distributed, as shown in Fig. 2.2. In the figure, $\vec{B}$ represents the magnetic field vector. The Vlasov and Maxwell equations should incorporate the coordinate transformation from the particle's position to the guiding center position. To correctly represent the plasma turbulence in this framework, the so-called gyrokinetic ordering [89, 141] involving a small parameter δ should be satisfied:

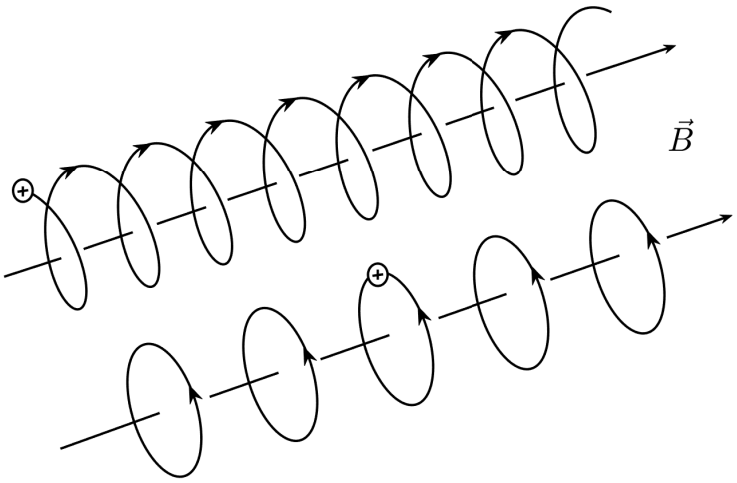

Figure 2.2 – Illustration of the cyclotron motion of the ion and its representation in the gyrokinetic framework. (Inpired by Ref. [142])

$$\frac{\omega}{\Omega_i} \sim k_{\parallel}\rho_i \sim k_{\perp}\rho_i \frac{\delta\phi}{T} \sim \mathcal{O}(\delta), \tag{2.1}$$

where ω is the drift wave frequency, Ω_i is the ion cyclotron frequency, $k_{\parallel}$ and $k_{\perp}$ are the wave number in the direction parallel and perpendicular to magnetic field lines, respectively; ρ_i is the ion gyro radius, T is the plasma temperature, $\delta\phi$ is the electrostatic potential fluctuations.

2.4 Model equations

This section presents the simulation and physics model implemented in GTC. The equilibrium magnetic configuration used in GTC is obtained from EFIT [143], IPREQ [144] or VMEC [145] codes that basically solve the Grad-Shafranov equation. The spline interpolation is used to map the coarse equilibrium mesh to the fine computational mesh [131]. GTC uses the field-aligned coordinate system to study the magnetically confined plasma with nested flux surfaces [88], which is suitable for efficiently integrating particle trajectories that move primarily along the magnetic field lines. The fully kinetic dynamics of the plasma particles require a smaller step size to resolve the cyclotron motion, which in turn makes the simulations computationally expensive. To resolve this issue, a coordinate transformation is made from particle coordinates to the

guiding center coordinates. So, the resulting gyrokinetic equations involve the motion of the plasma particles in the reduced 5D space.

2.4.1 Particle dynamics

The gyrokinetic Vlasov equation [89] describing the toroidal plasma in the inhomogeneous magnetic field in the five-dimensional phase space $(\vec{X}, v_\parallel, \mu)$ is given by

$$\left(\partial_t + \dot{\vec{X}} \cdot \nabla + \dot{v}_\parallel \partial_{v_\parallel}\right) f_\alpha(\vec{X}, \mu, v_\parallel, t) = C_\alpha f_\alpha, \tag{2.2}$$

$$\dot{\vec{X}} = \frac{\vec{B}^*}{B^*_\parallel} v_\parallel + \vec{v}_E + \vec{v}_c + \vec{v}_g + \vec{v}_{E_r}, \tag{2.3}$$

$$\dot{v}_\parallel = -\frac{1}{m_\alpha} \frac{\vec{B}^*}{B^*_\parallel} . (\mu_\alpha \nabla B + Z_\alpha \nabla \phi), \tag{2.4}$$

where $\vec{B}^* = \vec{B} + B v_\parallel / \Omega_i \left(\nabla \times \hat{b}\right)$, $B^*_\parallel = \hat{b} \cdot \vec{B}^*$, C_α is the pitch-angle collision operator described in Ref. [146], $\vec{v}_E$ is the $\vec{E} \times \vec{B}$ drift velocity, $\vec{v}_{E_r}$ is the drift velocity due to the neoclassical radial electric field, and $\vec{v}_c$, and $\vec{v}_g$ are magnetic drift velocities due to the curvature and gradient in the magnetic field that are given by

$$\vec{v}_E = \frac{c\hat{b} \times \nabla (\delta\phi + \langle\phi\rangle)}{B^*_\parallel}, \tag{2.5}$$

$$\vec{v}_c = \frac{B}{B^*_\parallel} \frac{v_\parallel^2}{\Omega_\alpha} \nabla \times \hat{b}, \tag{2.6}$$

$$\vec{v}_g = \frac{\mu_\alpha}{m_\alpha \Omega_\alpha} \frac{\vec{B} \times \nabla B}{B^*_\parallel}, \tag{2.7}$$

$$\vec{v}_{E_r} = \frac{c\hat{b} \times \nabla \phi_{E_r}}{B^*_\parallel}, \tag{2.8}$$

where B is the amplitude of the equilibrium magnetic field at particle position, B^* is the equilibrium magnetic field amplitude at the guiding center position of the particle, Z_α is the charge, m_α is the mass, μ_α is the magnetic moment of the particle, and Ω_α is the cyclotron frequency of the plasma species. ϕ is the electrostatic potential, which comprises of the electrostatic non-zonal potential $\delta\phi$, zonal potential $\langle\phi\rangle$ averaged over the flux surface, and the electrostatic potential due to the neoclassical radial electric field ϕ_{E_r}, i.e., $\phi = \delta\phi + \langle\phi\rangle + \phi_{E_r}$, with $\langle\delta\phi\rangle = 0$.

The gyrokinetic particle equations of motion are derived in magnetic coordinates (ψ, θ, ζ) [147], where ψ is the magnetic flux, θ is the poloidal angle and ζ is the toroidal angle, and are given by

$$\dot{\psi} = \frac{c}{Z_\alpha}\frac{\partial \varepsilon}{\partial B}\left(\frac{I}{D}\frac{\partial B}{\partial \zeta} - \frac{g}{D}\frac{\partial B}{\partial \theta}\right) + \frac{cI}{D}\frac{\partial \phi}{\partial \zeta} - \frac{cg}{D}\frac{\partial \phi}{\partial \theta}, \tag{2.9}$$

$$\dot{\theta} = \frac{v_\parallel B(1-\rho_c g')}{D} + \frac{cg}{D}\left(\frac{1}{Z_\alpha}\frac{\partial \varepsilon}{\partial B}\frac{\partial B}{\partial \psi} + \frac{\partial \phi}{\partial \psi}\right), \tag{2.10}$$

$$\dot{\zeta} = \frac{v_\parallel B(q+\rho_c I')}{D} - \frac{cI}{D}\left(\frac{1}{Z_\alpha}\frac{\partial \varepsilon}{\partial B}\frac{\partial B}{\partial \psi} + \frac{\partial \phi}{\partial \psi}\right). \tag{2.11}$$

The equation for the parallel momentum is given by

$$\dot{\rho}_\parallel = -c\frac{(1-\rho_c g')}{D}\left(\frac{1}{Z_\alpha}\frac{\partial \varepsilon}{\partial B}\frac{\partial B}{\partial \theta} + \frac{\partial \phi}{\partial \theta}\right) - c\frac{(q+\rho_c I')}{D}\left(\frac{1}{Z_\alpha}\frac{\partial \varepsilon}{\partial B}\frac{\partial B}{\partial \zeta} + \frac{\partial \phi}{\partial \zeta}\right), \tag{2.12}$$

where

$$D = gq + I + \rho_c(gI' - Ig'),$$

$$I' = \frac{\partial I}{\partial \psi}, \quad g' = \frac{\partial g}{\partial \psi},$$

$$\rho_\parallel = \frac{v_\parallel}{\Omega_\alpha},$$

$$\frac{\partial \varepsilon}{\partial B} = \mu_\alpha + \frac{Z_\alpha^2}{m_\alpha c^2}\rho_\parallel^2 B.$$

I and g are the poloidal and toroidal currents, respectively. The particle equations of motion are solved using the Runge Kutta method [92].

2.4.2 Low-noise δf method

To reduce the particle noise due to Monte Carlo sampling of the phase space, the δf method [97] is used in which only the perturbed part of the particle distribution is evolved with time. The distribution function is written as the sum of equilibrium and perturbed parts, $f_\alpha = f_{0\alpha} + \delta f_\alpha$, with the equilibrium part satisfying the 5D-gyrokinetic equation. Further, an additional dynamical variable, particle weight, is defined as $w_\alpha = \delta f_\alpha / f_\alpha$, that satisfies the following equation:

$$\frac{d\mathrm{w}_\alpha}{dt} = (1-\mathrm{w}_\alpha)\left[-(\vec{v}_E + \vec{v}_{E_r}).\frac{\nabla f_{0\alpha}}{f_{0\alpha}} + \frac{Z_\alpha}{m_\alpha}\frac{\vec{B}^*}{B}.\nabla\phi\frac{1}{f_{0\alpha}}\frac{\partial f_{0\alpha}}{\partial v_\parallel}\right], \tag{2.13}$$

where $f_{\alpha 0}$ is the Maxwellian, solution to the Vlasov equation to the lowest order, given by

$$f_{\alpha 0} = n_{\alpha 0}\sqrt{\frac{m_\alpha}{2\pi T_{\alpha 0}}}\exp\left[-\frac{m_\alpha v_\parallel^2 + 2\mu_\alpha B}{2T_{\alpha 0}}\right].$$

The kinetic treatment of electrons is required to study the effect of electrons on ITG turbulent transport and to include the instabilities like TEM in the simulations. However, a drift-kinetic treatment of electrons imposes difficulties due to the electron parallel Courant condition [148] and high frequency oscillations due to ω_H mode [140]. To overcome this limitation, the fluid-kinetic hybrid model is implemented in GTC [119]. To solve the drift-kinetic equation for electron, the electron response and electrostatic potential are expanded in the smallness parameter δ, where δ is the ratio of drift wave frequency to the electron transit frequency; as $f_e = f_{0e} + \frac{e\delta\phi^{(0)}}{T_e}f_{0e} + \delta g_e$, and $\delta\phi = \delta\phi^{(0)} + \delta\phi^{(1)}$. The nonadiabatic parts δg_e, $\delta\phi^{(1)}$ are smaller than the adiabatic parts by a factor of δ.

2.4.3 Field solver

The electrostatic potential is acquired from Poisson's equation in a spatial network of grids after the charge density is accumulated on the grids. However, in the gyrokinetic framework, gyrokinetic transformation must also be incorporated into Poisson's equation. This results in a gyrokinetic version of Poisson's equation involving the electrostatic potential and particle density that are averaged over the charge ring with a local gyro-radius of the charged particle. The gyrokinetic Poisson equation [140] is given by

$$\frac{e\tau}{T_e}\left(\phi - \tilde{\phi}\right) = \frac{\delta\bar{n}_i - \delta n_e}{n_0}, \tag{2.14}$$

where $\tau = T_e/T_i$, the first term on left-hand side is the ion polarization term, n_0 is the equilibrium electron density. The electrostatic potential in the lowest order is acquired from the gyrokinetic Poisson equation given below

$$\frac{(\tau+1)e\delta\phi^{(0)}}{T_e} - \frac{\tau e\delta\tilde{\phi}^{(0)}}{T_e} = \frac{\delta\bar{n}_i - \langle\delta\bar{n}_i\rangle}{n_0}, \tag{2.15}$$

where $\langle\delta\bar{n}_i\rangle$ is the ion zonal density, $\delta\tilde{\phi}^{(0)}$ is the second gyro-averaged perturbed potential defined as

$$\delta\tilde{\phi}^{(0)}(\vec{x}) = \frac{1}{2\pi}\int \mathrm{d}^3\vec{v}\int \mathrm{d}^3\vec{X} f_0(\vec{X})\delta\bar{\phi}^{(0)}(\vec{X})\delta(\vec{X}+\vec{\rho}-\vec{x}),$$

with $\vec{x}$ and $\vec{X}$ representing the coordinates of particle position and the particle guiding center position, respectively, and $\vec{\rho}$ is a gyro-radius vector. $\delta\bar{\phi}^{(0)}$ is the first gyro-averaged perturbed potential defined by

$$\delta\bar{\phi}^{(0)}(\vec{X}) = \int \mathrm{d}^3\vec{x}\int \frac{d\varphi}{2\pi}\delta\phi^{(0)}(\vec{x})\delta(\vec{x}-\vec{X}-\vec{\rho}),$$

and similarly

$$\delta\bar{n}_i(\vec{x}) = \int \mathrm{d}^3\vec{X}\int \frac{d\varphi}{2\pi}\delta f(\vec{X})\delta(\vec{x}-\vec{X}-\vec{\rho})$$

is the perturbed ion density at the guiding center, and φ is the gyro-phase. The second gyro-averaged perturbed electrostatic potential ($\delta\tilde{\phi}^{(0)}$) is calculated using Padé approximation [131]. In the higher order, the electron dynamics is governed by the drift-kinetic equation in δg_e. To resolve the electron dynamics it is pushed several times in a single push step for ion, known as the subcycling ratio. An iterative time-stepping sequence has been used to update the particle orbits and field quantities. At ith time step, all the field quantities are computed, and at $(i+1)$th time step, ion orbits are pushed using the gyrokinetic equation. The electron weight $\mathrm{w}_e = \delta g_e/f_e$ is evolved according to the equation

$$\begin{aligned}\frac{d\mathrm{w}_e}{dt} = \left(1-\frac{e\delta\phi^{(0)}}{T_e}-\mathrm{w}_e\right)\Bigg[-(\vec{v}_E+\vec{v}_{E_r})\cdot\nabla\ln f_{0e}|_{v_\perp} - \frac{\partial}{\partial t}\left(\frac{e\delta\phi^{(0)}}{T_e}\right) - \\ (\vec{v}_d+\delta\vec{v}_E)\cdot\nabla\left(\frac{e\phi}{T_e}\right)\Bigg],\end{aligned} \tag{2.16}$$

where $\delta\vec{v}_E = (c/B^*)\hat{b}\times\nabla\delta\phi$, the notation '$|_{v_\perp}$' indicates that the the gradient operator on '$\ln f_{0e}$' is performed with $v_\perp$ held fixed. The electron orbits are pushed from ith time step to $(i+1)$th time step using all the field quantities at ith time step in Eq. (2.16). The non-zonal electrostatic perturbed potential till the first order correction is related to the density perturbation as

$$\mathrm{e}^{e\delta\phi/T_e} = \mathrm{e}^{e\delta\phi^{(0)}/T_e} - \frac{\delta n_e - \langle\delta n_e\rangle}{n_0}, \tag{2.17}$$

with $\delta n_e = \int \delta h_e d^3\vec{v}$, $\langle\delta n_e\rangle$ is the electron zonal density. Equations (2.16) and (2.17) can be solved repeatedly to reach the higher order in the expansion. The order of expansion depends upon the trapped fraction of electrons. The convergence test shows that the second order expansion is sufficient for all the trapped

electrons taken into account. The equations for ions are solved only once. Finally, all the particle orbits and non-zonal components of field quantities are updated at $(i+1)$th time step, and the zonal component of the electrostatic potential at $(i+1)$th time step is obtained by solving

$$\frac{\tau e\left(\langle\phi\rangle - \left\langle\tilde{\phi}\right\rangle\right)}{T_e} = \frac{\langle\delta\bar{n}_i\rangle - \langle\delta n_e\rangle}{n_0}. \tag{2.18}$$

The flux-surface-averaged gyrokinetic Poisson equation represents the zonal component and is solved by traditional integration, while a finite difference-based gyrokinetic Poisson solver is incorporated in GTC for the non-zonal component. The resulting matrix equation is solved using PETSc [149] or HYPRE [150] libraries. The electrostatic field is then scattered back to the guiding center position to update the orbit. The out-of-boundary particles are brought back to the simulation domain by the energy-conserving boundary conditions. Fixed boundary conditions are applied for all fluctuating quantities at both sides of the radial simulation domain.

2.4.4 Charge deposition and gyro-averaging

Followed by the push phase of the PIC cycle, the particles need to deposit charge and current over the nearest grid points to compute the charge and current density, respectively. Figure 2.3 shows the schematic of the charge deposition scheme implemented in GTC. The 3D torus shown in the upper panel of the figure is decomposed into poloidal and toroidal grid points. Field-aligned mesh is used to represent the fluctuating quantities. The particle with the coordinates (ψ,θ,ζ) is first located along the toroidal direction, and then its weight is calculated to the neighboring poloidal planes. Over the poloidal plane, the simulation grids are created in the ψ and θ directions, as shown in the lower left panel of the figure. Flux surfaces, equidistant in the radial direction, are created. Then, the equidistant grid points are created in the poloidal direction on each flux surface. Onto the poloidal plane, the particle is located in the ψ direction by finding the flux surfaces between which it lies, and the corresponding weight is calculated. Once the particle deposit charge on the neighboring flux surfaces, it is located in the poloidal direction and weight is evaluated on the poloidal grids.

In the gyrokinetic framework, the physical quantities are averaged-out over the cyclotron motion of the particle. However, to retain the finite Larmor radius (FLR) effects, a procedure called gyro-averaging is used. For this, a charge ring is formed around the guiding center position of the particle with the local gyro-radius of the particle. Numerically, this charge ring is represented by a

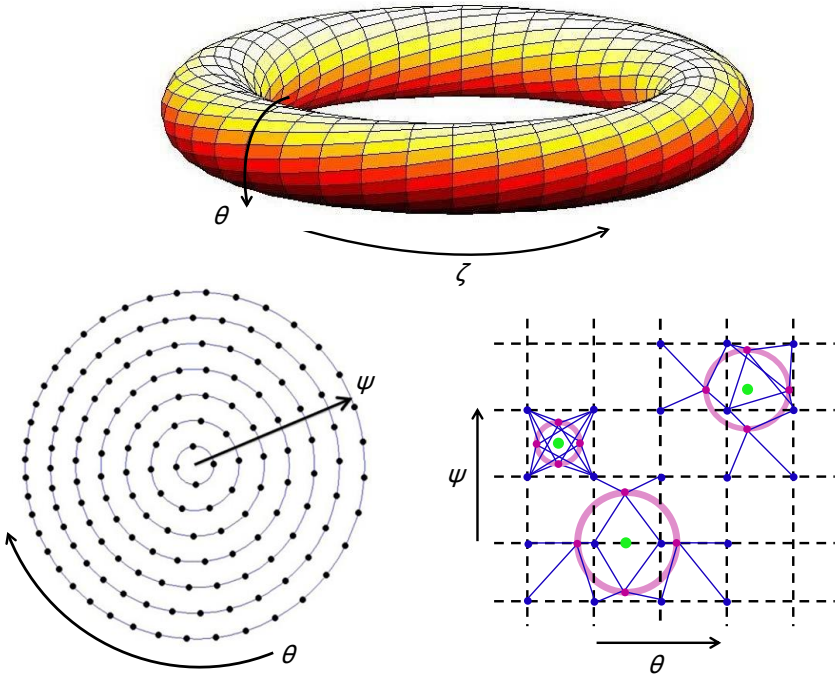

Figure 2.3 – Schematic of the charge deposition and gyro-averaging implemented in GTC. (Inspired by Ref. [138])

finite number of points (4, 8, 16, etc.), depending upon the radius of the ring. Usually, the four-point approximation of the charge ring is good enough. The poloidal magnetic field is much smaller than the toroidal magnetic field, so the gyro-averaging is approximated on the poloidal plane. The schematic of the gyro-averaging is shown in the lower right panel of the figure. In the figure, the poloidal grids are represented by the square mesh, and the guiding center particle position is represented by the solid green circles, the magenta circles show the charge ring, and the solid blue circles show the nearest grid points on which the particle deposit charge and current.

The deposited charge and current densities are then used to calculate the electromagnetic fields on the grid points from Poisson and Ampere's equation. These fields are scattered back to the particle's guiding center position by calculating the particle weights from the simulation grid points to the particle position, which is similar to the reverse of the charge deposition scheme. Once the fields are calculated at the particle's position, the equations of motion are integrated to update the particle's position and velocity, thus completing one PIC cycle.

2.4.5 Collisional effects

Collisional effects can significantly affect the microturbulent transport in fusion plasmas. The collisions between the plasma species can affect the turbulence and transport directly by affecting the linear microturbulence drive or indirectly by affecting the coherent phase space structure. It has been found that the collisional effects can reduce the ITG turbulence growth rate, can lead to the stabilization of TEM turbulence, or can lead to a transition from TEM to ITG turbulence by the de-trapping of electrons [151–153].

In GTC, the Fokker-Planck collision operator for the collisions between like species and the Lorentz pitch angle scattering operator for the collisions between unlike species are implemented where the momentum and energy conservation is enforced on the neoclassical mesh [146]. The dimensionless effective collision frequency defined in GTC is $\nu^* = \epsilon^{-3/2}\nu q R_0/v_{th}$, with $\epsilon = r/R_0$ as the local inverse aspect-ratio, r is the radius evaluated on the outer mid-plane, ν is the physical collision frequency, and $v_{th,\alpha} = \sqrt{T_{0\alpha}/m_\alpha}$ is the thermal velocity of the plasma species α. The recent gyrokinetic simulations using GTC have shown the effects of collisions on the ITG and TEM dominant discharges of the DIII-D [154], ADITYA-U [135].

2.4.6 Extension to multiple ion species

So far, the model equations have considered the plasma as the thermal ions and electrons. However, other ion species are also present as impurities. In order to study the effect of impurity ions on microturbulence, the impurity ions need to be modeled along with the thermal ions and electrons. The gyrokinetic equations of motion for impurity ions follow the same form discussed in Sec. 2.4.1. However, the gyrokinetic Poisson equation needs to be modified to incorporate the impurity ions as follows:

$$\sum_{\alpha=i,z} \frac{Z_\alpha^2 n_{0\alpha}}{T_\alpha}\left(\phi - \tilde{\phi}_\alpha\right) + \frac{e^2 n_{0e}}{T_e}\phi = \left(Z_i \delta\bar{n}_i + Z_z \delta\bar{n}_z - e\delta n_{e,kinetic}\right), \tag{2.19}$$

where i, z correspond to thermal and impurity ions. The first term on the left-hand side is the ion polarization density [140] due to each of the ion species, $\tilde{\phi}_\alpha$ is the second gyro-averaged electrostatic potential. The remaining procedure to solve the field equation is similar to that discussed in Sec. 2.4.3. The weight equation for the impurity ions also shares the same form as is given by Eq. 2.13.

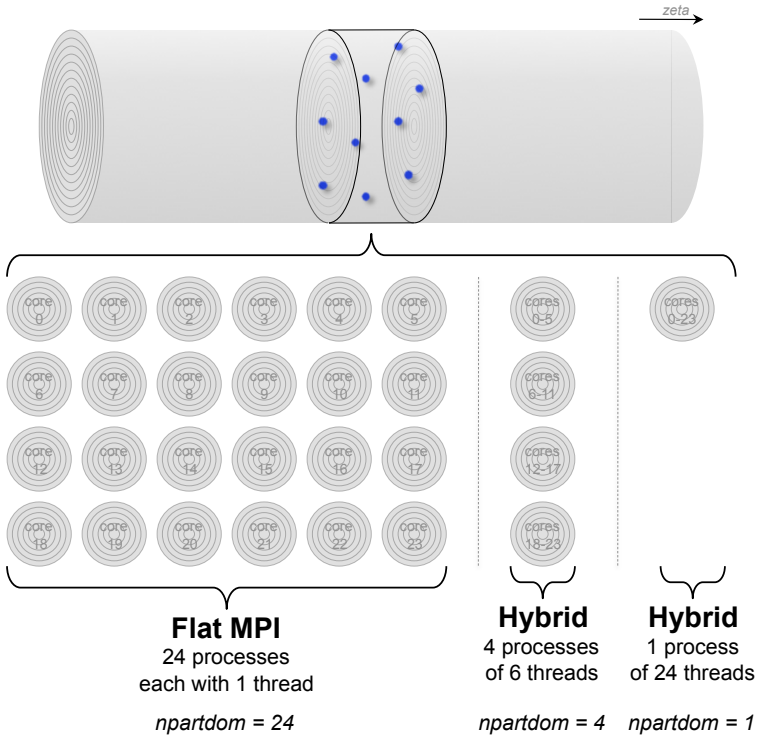

Figure 2.4 – Illustration of the parallel computing architecture used in GTC. Source: Ref. [138]

2.4.7 Parallel computing architecture

PIC-based codes like GTC require millions or billions of marker particles and millions of computational grids to represent the plasma distribution and confinement geometry. This increases the computational cost of the gyrokinetic simulations. Advancements in high-performance computing have made it possible to increase the computational efficiency of the simulations by using the parallel computing architecture. In this direction, GTC is optimized on multi-core and many-core computing systems. GTC uses hybrid computing architecture, OpenMP/MPI, for the computational speedup, as shown in Fig. 2.4. A two-level decomposition is implemented in GTC: a 2D domain decomposition in the toroidal direction and the particle domain decomposition. 3D torus is decomposed into *mtoroidal* number of toroidal domains assigned to each MPI process. Onto each toroidal section, the particle domain decomposition is implemented, assigning the chunks of particles in the domain to *npartdom* number of MPI processes. For further speedup, loop-level parallelization is utilized by assigning *numthreads* OpenMP threads to each MPI process. For example, the figure shows the schematic of the flat MPI and hybrid parallelization for a computing system with 24 cores per node. In the flat MPI parallelization, the particles in one toroidal section, as shown in the upper panel of the figure,

are assigned to 24 MPI processes with $npartdom = 24$ and $numthreads = 1$. However, hybrid parallelization can be realized in several ways with different values of $npartdom$ satisfying $numberpe = npartdom \times mtoroidal$, where $numberpe$ is the total number of MPI processes. In the figure, one of the possible combinations depicts 4 MPI processes assigned to each toroidal section along with 6 OpenMP threads dedicated to each MPI process, thus resulting in $npartdom = 4$. It is also possible to exploit the parallelism by assigning all the particles in the toroidal section to a single MPI process and using 24 OpenMP threads that give $npartdom = 1$. This parallel architecture results in the speedup of GTC simulations by many folds. GTC is also optimized for next-generation GPU-accelerated clusters with plenty of CUDA cores. Following this trend, the heterogenous CPU/GPU parallel programming architecture is exploited in GTC. Detailed information can be found in Refs. [138, 139].

2.5 Conclusions and discussion

This chapter has presented a brief overview of the simulation and physics model implemented in GTC to study the electrostatic microturbulent transport in fusion plasmas. Based on the numerical techniques and simulation model discussed, the global gyrokinetic simulations of electrostatic microturbulence in LHD stellarator and ADITYA-U tokamak are presented in this thesis to understand the transport.

Chapter 3

Electrostatic microturbulence in LHD stellarator

3.1 Introduction

The stellarator is increasingly becoming an attractive and promising concept in the quest of magnetically confined nuclear fusion due to its intrinsic advantages of not having a toroidal current, lower levels of MHD activities, steady state operation, and absence of disruptions [14–16]. However, these benefits come at the cost of toroidal symmetry breaking that leads to an increase in the neoclassical transport, and stronger damping of zonal flows as compared to the axisymmetric tokamaks [75, 76]. To mitigate these disadvantages, quasi-symmetry and quasi-isodynamicity concepts have been developed as further optimization of the stellarator configuration [17–19]. Following this trend, the Large Helical Device (LHD) has recently been optimized with a strong inward shift of the magnetic axis to reduce the neoclassical transport to a level of an advanced stellarator [155]. After the reduction of neoclassical transport, the microturbulent transport in the stellarators still remains a major challenge. For example, phase contrast imaging (PCI) of the core plasma fluctuations show evidence of the ion temperature gradient (ITG) and trapped electron mode (TEM) turbulence in the W7-X stellarator [77]. In a similar way, characteristic signatures of the ITG turbulence [81–84] have been observed in the LHD. Therefore, the presence of microturbulence in stellarators remains a serious challenge and it is of great importance to gain a proper understanding of their nature and dynamics.

Over the past few years, some progress has been made towards gyrokinetic simulations of microturbulence in stellarators. Gyrokinetic flux-tube simulations using GKV code have been carried out extensively in the LHD [110–112], where the reduction of the ITG turbulence due to zonal flow, the role of the

zonal flow on the TEM turbulence, and the effects of isotopes and collisions on the microinstabilities in the LHD have been studied. However, the flux-tube simulations do not capture the linear coupling of multiple toroidal harmonics due to the 3D structure of the magnetic field in the stellarators and the secular radial drift of helically trapped particles across flux surfaces.

Hence, a global gyrokinetic simulation study is required to have a better understanding of the microturbulence in the stellarators. The first global gyrokinetic simulations using the EUTERPE code with adiabatic electrons was recently carried to study the effects of the radial electric field on the ITG turbulence in W7-X and LHD [113]. The gyrokinetic toroidal code (GTC) has been used to carry out the first global nonlinear ITG turbulence simulations with adiabatic electrons in the W7-X and LHD [114]. GTC has also self-consistently calculated neoclassical ambipolar radial electric fields in the W7-X, which were shown to suppress the ITG turbulence more strongly in the electron-root case than the ion-root case [115]. XGC-S [116] and GENE-3D [117] have performed global gyrokinetic simulations of microturbulence in the W7-X using adiabatic electrons. The adiabatic electron model cannot address the effect of kinetic electrons on the ITG turbulence [118, 119], and the excitation of the TEM turbulence [120]. Furthermore, recently, a new scheme has been advised to precisely take care of the global effects in stellarators by taking the moments of the gyrokinetic equation and using an ordering that describes the fluctuations as strongly varying across the equilibrium magnetic field and slowly varying along it [156].

Kinetic electrons were first incorporated in the global gyrokinetic simulations of the W7-X and LHD to study the collisionless damping of zonal flow [157]. Subsequently, GTC simulation with a sufficiently high mesh resolution found a new helical trapped electron mode (HTEM) in the W7-X [158]. Finally, GENE-3D with a reduced mesh resolution has been used in the recent work to perform the simulations of the electromagnetic ITG turbulence with kinetic electrons in the W7-X-like plasma [159].

In this paper, we present global gyrokinetic simulations with kinetic electrons of microturbulent transport in the LHD stellarator. The GTC code [93] is employed for this purpose in order to investigate the growth rate, nonlinear turbulent transport, as well as the linear and nonlinear spectra of the ITG and TEM turbulence. ITG turbulence simulations show that the kinetic electron effects increase the growth rate of the most unstable mode and the turbulent transport. GTC simulations indicate that the zonal flow leads to a decrease in the ITG transport levels by the zonal flow, hence the zonal flow acts as the ITG dominant saturation mechanism. TEM simulations show that the linear

eigenmode is localized on the outer mid-plane of the LHD, due to the the trapping of electrons toroidally on the outer mid-plane side of LHD, similar to the tokamak. This is opposite to the HTEM localization in the inner mid-plane of W7-X [158]. Because the electrons are trapped toroidally on the outer mid-plane side of LHD, similar to the tokamak. However, the self-generated zonal flow is found to have insignificant effect on the dynamics of the TEM transport. Rather, the inverse cascade of the high poloidal and toroidal harmonics to the lower harmonics is the dominant saturation mechanism. The role of zonal flow in TEM turbulence suppression has been widely discussed for axisymmetric tokamaks [152, 160–166] and has been shown that the zonal flow effects are typically weaker in the TEM turbulence than in the ITG turbulence. However, the strength of the zonal flow in regulating the TEM turbulence depends on detailed plasma profiles and parameter regimes for both tokamaks [166] and stellarators [167]. A comparison of the transport coefficients between different cases for $\eta = 0$, 1, and ∞, where η is the ratio of the ion temperature gradient to the density gradient, shows that the ITG turbulence is more effective in driving the heat conductivity whereas TEM turbulence is more effective for the particle diffusivity.

This chapter is discussed as follows: in section 3.2, the three-dimensional geometry and simulation model are presented. In section 3.3, ITG and TEM turbulence simulations with kinetic electrons are presented. Finally, conclusions are made in section 3.4.

3.2 Stellarator geometry

Gyrokinetic toroidal code (GTC) is a global 3D code to study the physics of microturbulent transport [120,131], Alfvén waves [132], energetic particles [134], and radio frequency waves [133] in toroidally confined plasmas. To reduce the particle noise due to Monte Carlo sampling of particle distribution, GTC uses a low noise δf method [97] in which only the perturbed part of the particle distribution is evolved with time. GTC simulations performed in this paper use the non-axisymmetric equilibrium of the LHD stellarator [113] constructed by the ideal MHD code VMEC assuming closed magnetic surfaces [145]. The equilibrium geometry and the magnetic field are described as the Fourier series in both poloidal and toroidal directions on a discrete radial mesh that is equidistant in the toroidal flux. These equilibrium quantities are then transformed to the Boozer coordinates as the Fourier series in the toroidal direction on discrete grid points on the 2D poloidal plane [168]. The 3D quadratic spline interpolation is used in GTC to represent the equilibrium magnetic field and metric

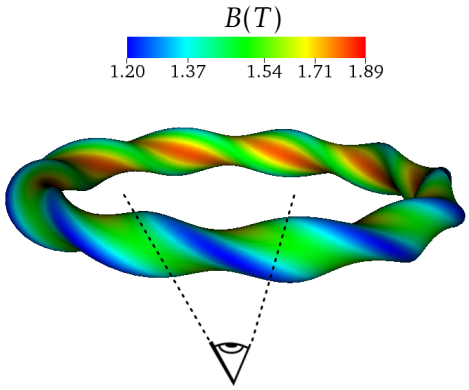

Figure 3.1 – The 3D real space contour plot of magnetic field amplitude on the flux surface with $\psi = 0.36\psi_w$.

tensor on an equilibrium mesh [168]. The 3D LHD equilibrium used in this paper corresponds to the "outward shifted" configuration and has been used in earlier work for self-consistent GTC simulations [114,157]. The LHD device has a symmetry with a field period of $N_{fp} = 10$, which means all the equilibrium quantities have a periodicity of $2\pi/N_{fp}$ in the toroidal direction. Therefore, for turbulent transport, there are ten drift wave eigenmode families corresponding to the ten field periods. Earlier GTC simulations had found similar ITG growth rates for these ten eigenmodes, each coupling all toroidal n harmonics [114]. The equilibrium magnetic field on the flux surface with $\psi = 0.36\psi_w$ is shown in Fig. 3.1, where ψ_w is the poloidal flux on the last closed flux surface. Due to the field symmetry of the LHD, one-tenth of the torus is simulated which is represented by the dashed lines in Fig. 3.1. The "eye" in Fig. 3.1 indicates the point of view of the following 3D figures.

3.3 Microinstabilities in LHD

Drift-wave instabilities arise in fusion plasmas due to the non-uniformities of the plasma profile. In this section, the microinstabilities responsible for most of the anomalous turbulent transport observed in fusion plasmas, mainly ITG and TEM, are studied in LHD with the GTC code. Various temperature and density profiles are used in order to analyze the different instabilities. Thus, the ratio $\eta = \nabla \ln T_i / \nabla \ln n$ will be different for each simulation. In Sec. 3.3.1, an ion temperature gradient is set to excite the pure ITG turbulence ($\eta = \infty$), then in Sec. 3.3.2 the pure TEM instability can be analyzed when a density gradient is applied ($\eta = 0$). Finally, in Sec. 3.3.3 both density and ion temperature gradients are applied ($\eta = 1$) and the resultant turbulent transport is analyzed. The profiles used in the simulations have been chosen to excite these microin-

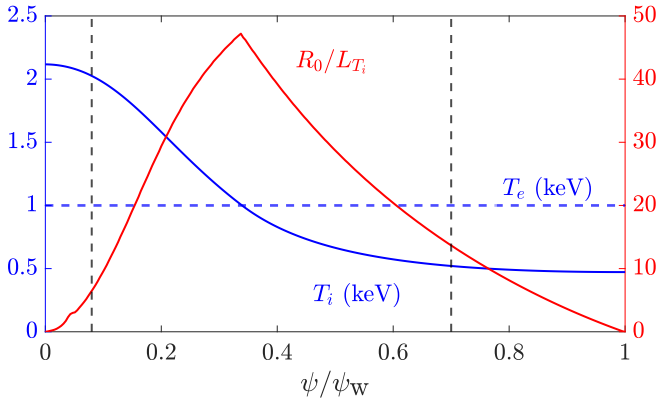

Figure 3.2 – Radial profiles for the equilibrium ion temperature T_i (blue solid line), the electron temperature T_e (blue dashed line), normalized ion temperature gradient R_0/L_{T_i} (red solid line) , used for the simulations of ITG turbulence with $\eta = \infty$. The black dashed lines represent the simulation boundary with $\psi_{\text{inner}} = 0.08\psi_w$ and $\psi_{\text{outer}} = 0.7\psi_w$.

stabilities in LHD plasma and are not meant to be the same as experimental profiles or previous gyrokinetic simulations [111, 112]. In the entire study, a uniform electron temperature profile is set and no equilibrium radial electric field is taken into account.

3.3.1 ITG

As mentioned in Sec. 3.1, global gyrokinetic simulations of ITG turbulence with adiabatic electrons have been carried out in non-axisymmetric devices as the LHD and/or W7-X stellarators using GTC [114], EUTERPE [169], XGC-S [170] and GENE-3D [117] codes. More recently, GENE-3D performed simulations of ITG in W7-X with kinetic electrons but reducing mesh resolution to solve the fastest growth rate [159]. Here, we expand the GTC work done in Ref. [114] by including kinetic electrons in ITG simulations using the model described in Chapter 2.

The plasma profile used for the pure ITG turbulence simulations is shown in Fig. 3.2. The on-axis ion temperature is 2 keV, the electron temperature is 1 keV, and the maximum normalized ion temperature gradient is $R_0/L_{T_i} \sim 47.2$ at $\psi \sim 0.33\psi_w$ where the rotational transform is $\iota \sim 0.5$. The inverse ion temperature gradient scale length is defined as $1/L_{T_i} = -\frac{\partial(\ln T_i)}{\partial r}$, where r is the local minor radius. The dashed black lines represent the simulation domain with $\psi_{\text{inner}} = 0.08\psi_w$, $\psi_{\text{outer}} = 0.7\psi_w$. A uniform density profile is set so $\eta = \infty$. After a convergence test, we use 200 radial grid points, 2700 poloidal grid points and 9 parallel grid points. The number of particles per cell are 50, the

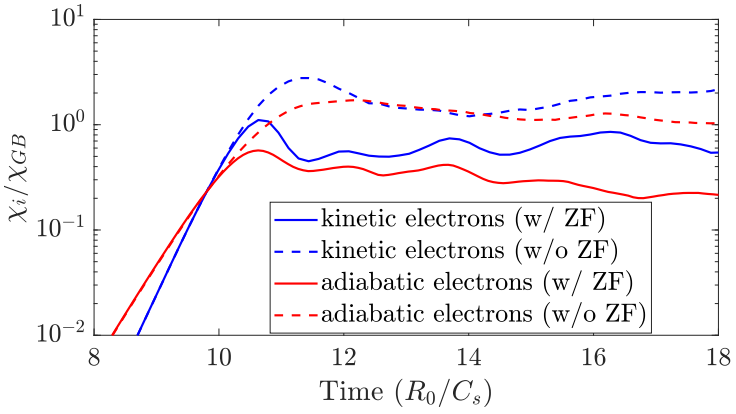

Figure 3.3 – The comparison of the time history of the ion heat conductivity averaged over $\psi \in [0.19, 0.38]\psi_w$ in gyro-Bohm units for adiabatic and kinetic electrons, with and without zonal flow.

time step size is $0.016R_0/C_s$, where $C_s/R_0 = 7.82 \times 10^4$ sec^{-1} and $C_s = \sqrt{T_e/m_i}$ is the speed of the ion acoustic wave. To resolve electron dynamics a time step 40 times lower is used. The linear instability threshold for the ITG turbulence is $(R_0/L_{T_i})_{cr} \sim 23.0$.

Figure 3.3 shows the time history of ion heat conductivity (averaged over $\psi \in [0.19, 0.38]\psi_w$) of the four nonlinear simulations discussed in this subsection. They correspond to simulations with (blue lines) and without (red lines) kinetic electrons where the self-generated zonal flow has been kept (solid lines) or numerically removed (dashed lines). Ion heat conductivity is normalized by the gyro-Bohm value, where $\chi_{GB} = \chi_B \rho^*$, $\chi_B = cT_e/eB$, and $\rho^* = v_i m_i c/eBa$ with $v_i = \sqrt{T_i/m_i}$, and a is the local minor radius. Nonlinear simulations show that turbulent transport grows exponentially in the linear phase and then it saturates. Simulations with zonal flow saturate at lower transport levels indicating the important role of zonal flow in turbulence saturation which is supported by the earlier gyrokinetic simulations. The effect of zonal flow is much more prominent in the case with adiabatic electrons (about 5 times higher). As the adiabatic electron response to the non-zonal potential does not drive a radial particle flux, the adiabatic electrons have no response to the zonal potential. However, the nonadiabatic part of the electron distribution leads to a radial particle flux that leads to zonal density, partially cancelling the ion zonal density. This reduces zonal flow and hence provides a mechanism to increase ITG turbulent transport by the kinetic electrons. These results are similar to the earlier investigations made for tokamaks [118, 119].

Figure 3.4a shows the electrostatic potential in a poloidal cross-section in

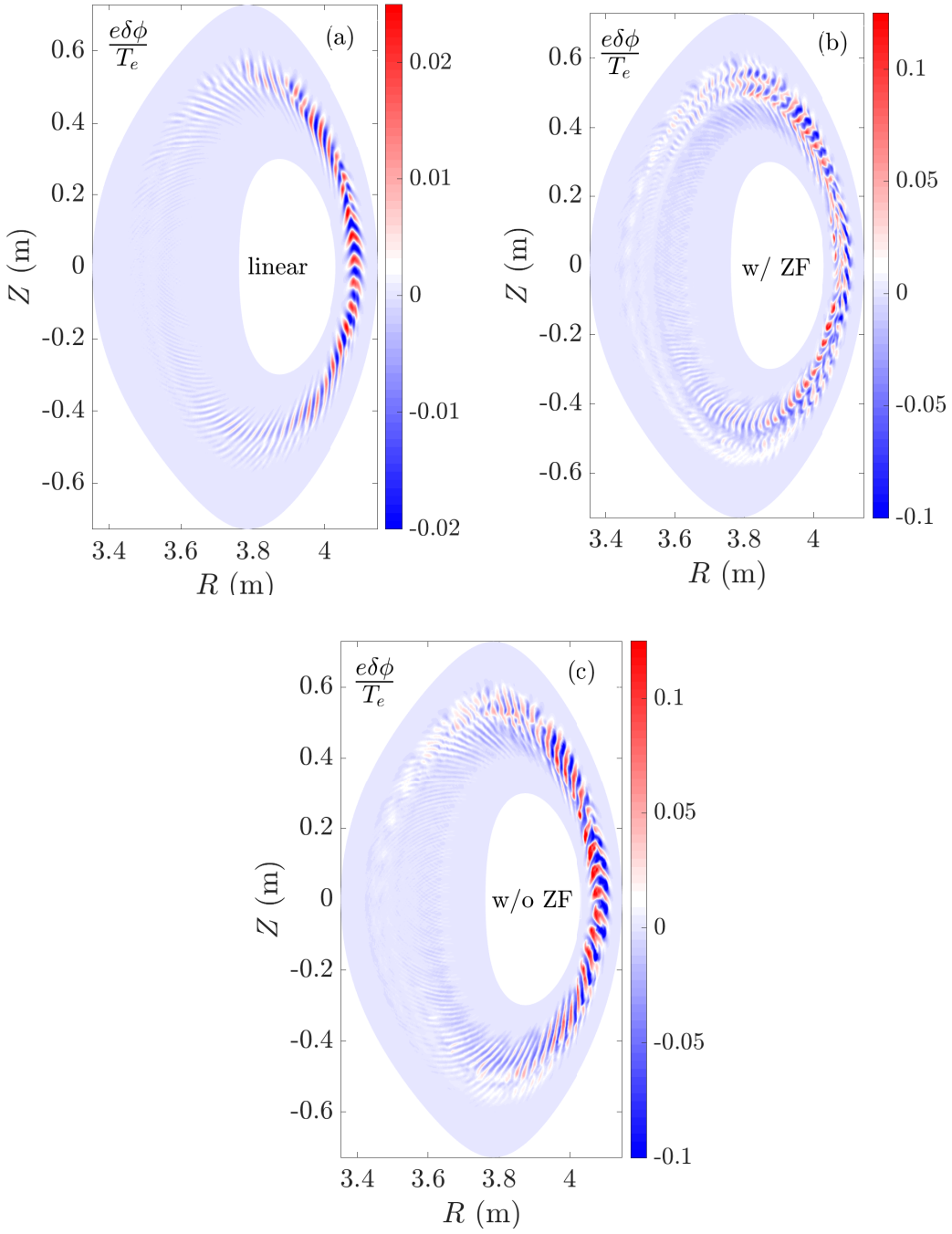

Figure 3.4 – Contour plots of the electrostatic perturbed potential in the linear phase at $t = 9.6R_0/C_s$ (a), in the nonlinear phase at $t = 11.2R_0/C_s$ with zonal flow (b) and in the nonlinear phase without zonal flow (c), of ITG turbulence simulation with kinetic electrons on a poloidal plane.

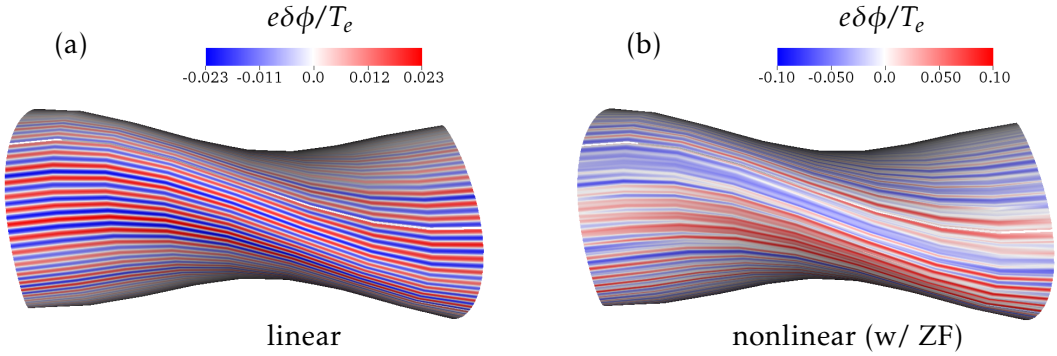

Figure 3.5 – The real space 3D contour plots of the electrostatic potential on the diagnosed flux surface with $\psi = 0.28\psi_w$ in the linear phase at time $t = 9.6R_0/C_s$ (a) and in the nonlinear phase at time $t = 11.2R_0/C_s$ with zonal flow (b).

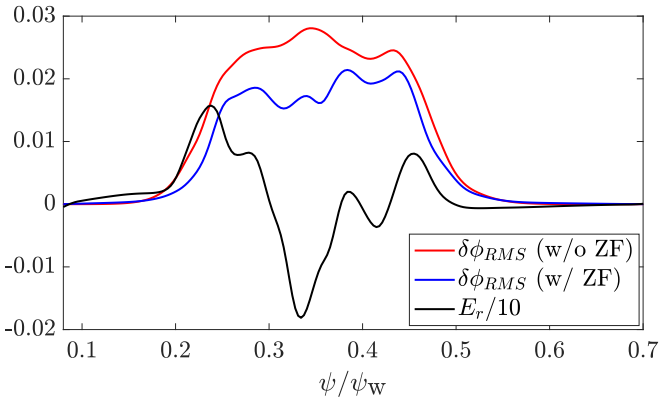

Figure 3.6 – The flux surface variation of the root-mean-squared electrostatic perturbed potential ($\delta\phi_{RMS}$) with (red line) and without (blue line) zonal flow and the radial electric field (E_r) (black line) resulting from the turbulence during the nonlinear stage of ITG turbulence simulations at time $t = 11.2R_0/C_s$. The electrostatic potential is normalized with T_e/e, and the radial electric field resulting from the turbulence is normalized with $\sqrt{T_e/e}$.

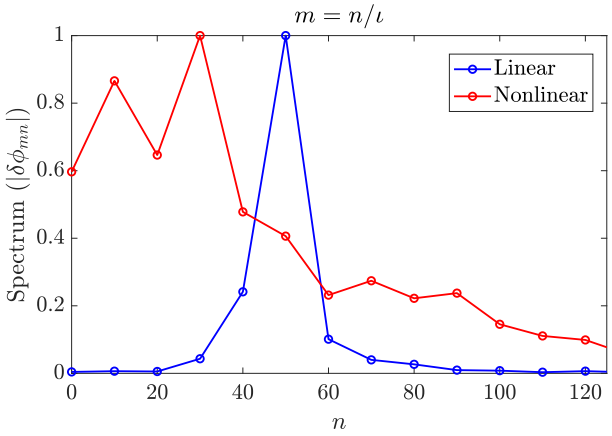

Figure 3.7 – The comparison of toroidal mode spectrum along $m = n/\iota$ in the linear and nonlinear phase of the ITG turbulence simulation using kinetic electrons.

the simulation with kinetic electrons during the linear phase at time $t = 9.6R_0/C_s$. The eigenmode is localized at the outer mid-plane in the region of low magnetic field strength where the curvature is bad, similar as in tokamaks and it peaks around $\psi \sim 0.26\psi_w$. Figure 3.4b shows the potential at the nonlinear stage at time $t = 11.2R_0/C_s$ during the simulation where the zonal flow has been kept (solid blue line in Fig. 3.3). In the nonlinear phase where the zonal flow is artificially removed (see Fig. 3.4c), the linear eigenmode structure starts smearing up due to the nonlinear mode coupling. Whereas, when the zonal flow is included in the simulations, the shear caused by the zonal flow leads to the breaking of these eddies even into finer structures. This behavior was also observed in LHD simulations with adiabatic electrons in a previous GTC work [114]. Figure 3.5 shows the real space 3D contour plot of the electrostatic potential on the diagnosed flux surface with $\psi \sim 0.28\psi_w$ in the linear stage at time $t = 9.6R_0/C_s$ (3.5a) and in the nonlinear stage at time $t = 11.2R_0/C_s$ (3.5b). Due to $k_{||} << k_{\perp}$ property of the microturbulence, the eddies are elongated along the field lines. The flux surface variation of root-mean-squared electrostatic perturbed potential with and without zonal flow, and the radial electric field resulting from the turbulence in the nonlinear stage at time $t = 11.2R_0/C_s$ are shown in Fig. 3.6. A noticeable difference between the turbulence potential with and without zonal flow can be seen by comparing red and blue lines that indicate the suppression of ITG turbulence due to the zonal flow.

Figure 3.7 shows the toroidal spectrum, for $m = n/\iota$, in the linear (blue) and nonlinear (red) phase of the simulation with kinetic electrons with zonal flow. The spectrum in the linear phase is narrow in the toroidal mode number with a maximum at $n = 50$ and an approximate width of $\Delta n \sim 20$. Linear simulations (not shown here) indicate that the most dominant eigenmode is $n = 50$, $m = 100$

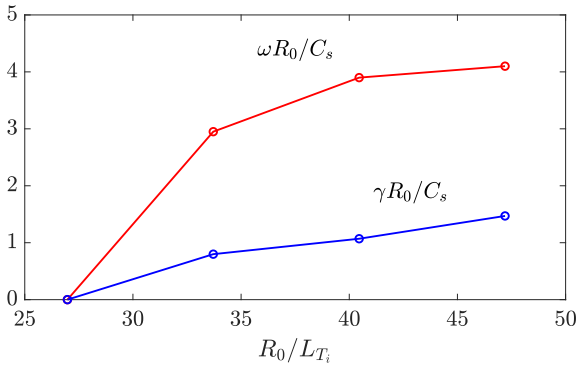

Figure 3.8 – The variation of the real frequency and growth rate of the most dominant ITG mode with the normalized density gradient R_0/L_{T_i}.

with a frequency of $\omega = 4.10C_s/R_0$, propagates in the ion diamagnetic drift direction and has a growth rate of $\gamma = 1.47C_s/R_0$ which is approximately 1.5 times larger than in adiabatic electron simulations ($\gamma = 0.96C_s/R_0$ and $\omega = 3.40C_s/R_0$). As there is no resonant interaction of the trapped electrons with the ITG modes, the response of trapped electrons to the ITG turbulence is almost zero, rather than adiabatic. Therefore, the dielectric constant in the gyrokinetic Poisson equation decreases when the trapped electron population increases. This provides a mechanism for increasing the ITG growth rate. The normalized perpendicular wave number corresponding to the dominant mode is $k_\perp \rho_i = 1.1$. In the nonlinear phase, the toroidal spectrum in Fig. 3.7 (averaged over time from $14.4R_0/C_s$ to $17.6R_0/C_s$), after an inverse cascade [114], becomes broader due to the nonlinear mode coupling.

Figure 3.8 shows the variation of the linear growth rate and frequency of the dominant ITG mode for each simulation. The linear instability threshold for the ITG turbulence is found for values of the normalized density gradient around $(R_0/L_{T_i})_{cr} \sim 27.0$. The growth rate increases almost linearly with the gradient though the variation is small as compared to the variation in frequency. As the gradient increases the spectrum also shifts to higher toroidal mode numbers. The nonlinear physics of the ITG turbulent transport show similar features as has been previously discussed in this section.

3.3.2 TEM

Trapped electron mode (TEM) driven turbulence is another dominant channel for transport in fusion plasmas which is destabilized due to the presence of density and/or electron temperature gradient. TEM turbulence simulations are mostly performed in LHD with flux-tube code GKV [111, 112] where the

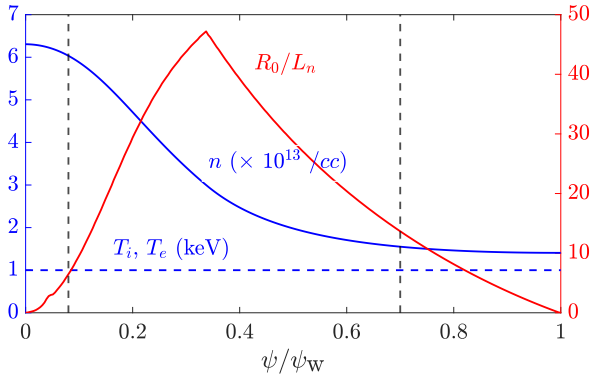

Figure 3.9 – Radial profiles for the equilibrium ion temperature T_i and electron temperature T_e (blue dashed line), the ion and electron density profile (blue solid line), the normalized density gradient R_0/L_n (red solid line), used for the simulations of TEM turbulence with $\eta = 0$. The black dashed lines represent the simulation boundary with $\psi_{\text{inner}} = 0.08\psi_w$ and $\psi_{\text{outer}} = 0.7\psi_w$.

effects of isotopes and collisions on microinstabilities and the role of zonal flow on TEM turbulence in LHD have been studied, as discussed in Sec. 3.1. In this section, the global nonlinear pure TEM turbulence simulations have been carried out using GTC.

The plasma profile used for the simulations is illustrated in Fig. 3.9. The maximum normalized density gradient is $R_0/L_n \sim 47.2$, where $1/L_n = -\frac{\partial(\ln n)}{\partial r}$, and also peaks at $\psi \sim 0.33\psi_w$. Temperature profiles are homogeneous along the plasma, $T_i = T_e = 1$keV, so $\eta = 0$. The simulation domain, represented by dashed black lines, is kept the same as in Sec. 3.3.1. Based on the convergence studies, mesh and number of particles are the same as described in Sec. 3.3.1.

Figure 3.10 shows the time history of two TEM simulations: one where the self-generated zonal flow has been kept (solid lines) and another where the zonal flow has been removed (dashed lines). The three quantities represented are the ion diffusivity averaged over $\psi \in [0.19, 0.45]\psi_w$ normalized by the gyro-Bohm value (red lines), radial electric field resulting from the turbulence (black line) and the root-mean-squared perturbed electrostatic potential (blue lines). It has been confirmed that $D_e \sim D_i$. First, turbulent transport exponentially grows during the linear phase, and then, due to mode coupling, inverse cascade from high to low mode number, and zonal flow interaction, it finally saturates. However, the zonal flow is not acting as the dominant saturation mechanism as can be seen from the simulations with and without zonal flow. In other words, the zonal flow in TEM simulations is not as important as it was for ITG saturation. The role of zonal flow in TEM turbulence suppression has been widely discussed for axisymmetric tokamaks [152, 160–166] and it is shown that the

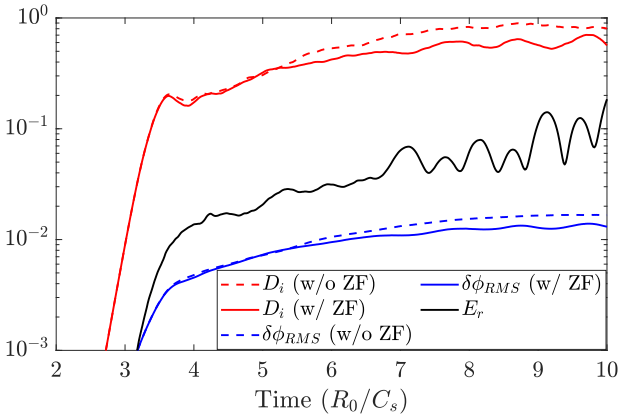

Figure 3.10 – Time history of the ion diffusivity averaged over $\psi \in [0.19, 0.45]\psi_w$ (red) and non-zonal electrostatic perturbed potential (blue) with zonal flow (solid) and without zonal flow (dashed) and zonal electric field (black). The diffusivity is normalized by the gyro-Bohm diffusivity and the electrostatic potential is normalzied by T_e/e, the radial electric field resulting from the turbulence is normalized with $\sqrt{T_e/e}$.

role of zonal flow is usually weak in TEM turbulence regulation. Although the TEM turbulence regulation by zonal flow depends upon the parameters such as magnetic shear, electron to ion temperature ratio, electron temperature gradient and η_e [152,163,164]. Additionally, the conclusions drawn for tokamak may or may not be consistent for LHD as the neoclassical radial electric field may have a considerable effect on the turbulent transport in stellarators [113, 171]. It could be a future study to explore this complex parameter landscape.

Figure 3.11a shows the electrostatic potential on a poloidal plane during the linear phase at time $t = 3.2R_0/C_s$, TEM eigenmode shows a thinner mode structure than ITG simulations. Like ITG turbulence, TEM turbulence is extended along the magnetic field lines and localized in the region of low magnetic field strength where the normal curvature is unfavorable and peaks at $\psi \sim 0.30\psi_w$. Figs. 3.11b and 3.11c shows the potential during the nonlinear phase at time $t = 6.4R_0/C_s$ for a simulation with and without zonal flows respectively. Turbulence spreading is observed during the nonlinear phase but the turbulent eddies are barely affected by zonal flows. Unlike ITG turbulence, the zonal flow is not playing an important role in the case of TEM turbulence. That is consistent with Fig. 3.10 where we previously discussed the little differences of the simulations with and without zonal flow. Figure 3.12a shows the contour plot of the electrostatic potential on the diagnosed flux surface $\psi \sim 0.28\psi_w$ in the 3D real space during the linear phase at time $t = 3.2R_0/C_s$. Like ITG turbulence, the eddies are elongated along the field lines. Figure 3.12b shows the

contour plot of electrostatic potential in 3D real space in the nonlinear stage at time $t = 6.4R_0/C_s$, with zonal flow. Figure 3.13 shows the flux surface variation of root-mean-squared electrostatic perturbed potential with and without zonal flow, and the radial electric field resulting from the turbulence. The red and blue lines are almost overlapping with each other, re-affirming that the zonal flow is not playing an important role in the TEM turbulent transport.

The toroidal mode spectrum, for $m = n/\iota$, at the linear (blue line) and nonlinear (red line) phases during a nonlinear TEM simulation is represented in Fig. 3.14. The linear spectrum indicates that the dominant eigenmode is $n = 140$, $m = 280$ with a linear growth rate $\gamma = 3.96C_s/R_0$, frequency $\omega = 0.55C_s/R_0$ and normalized perpendicular wave number $k_\perp \rho_i = 2.7$. The ratio $|\omega/\gamma| < 1$ implies that this TEM simulation may be reactive turbulence [172]. During the nonlinear saturation (averaged over time from $6.4R_0/C_s$ to $9.6R_0/C_s$), the nonlinear poloidal and toroidal mode coupling leads to an inverse cascade from high to low mode numbers [173].

We have carried out further TEM simulations with different normalized density gradients R_0/L_n. Figure 3.15 shows the variation of the linear growth rate and frequency of the dominant TEM turbulent mode for each simulation. The linear instability threshold for the TEM turbulence is found for values of the normalized density gradient around $(R_0/L_n)_{\rm cr} \sim 4.0$. The growth rate increases almost linearly with the gradient although the frequency barely increases. As the gradient increases the spectrum also shifts to higher toroidal mode numbers. The nonlinear physics of the TEM turbulent transport show similar features as has been previously discussed in this section.

3.3.3 Turbulence for $\eta = 1$ case

In the previous sections, the microturbulences studied are pure ITG and pure TEM in which either the ion temperature gradient or density gradient is present. But in general, both the temperature and density gradients are present in an experiment [111, 112]. In this section, an additional case is studied by taking into account the gradient in both the ion temperature and the plasma density while keeping the electron temperature profile uniform, and a comparison of the nonlinear turbulent transport for the cases with $\eta = 0$, 1, and ∞ is made. Figures 3.2 and 3.9 show the profiles used for the cases with $\eta = \infty$ and $\eta = 0$ that are discussed in Secs. 3.3.1 and 3.3.2 corresponding to the ITG and TEM turbulence respectively. For $\eta = 1$ case, the maximum of normalized ion temperature and density gradients are $R_0/L_{T_i} \sim 47.2$ and $R_0/L_n \sim 47.2$. The shape of the plasma profile is the same as is used for the cases with $\eta = \infty$ and 0. The maximum of gradients in profile is present at $\psi \sim 0.33\psi_{\rm w}$. The on-axis ion and

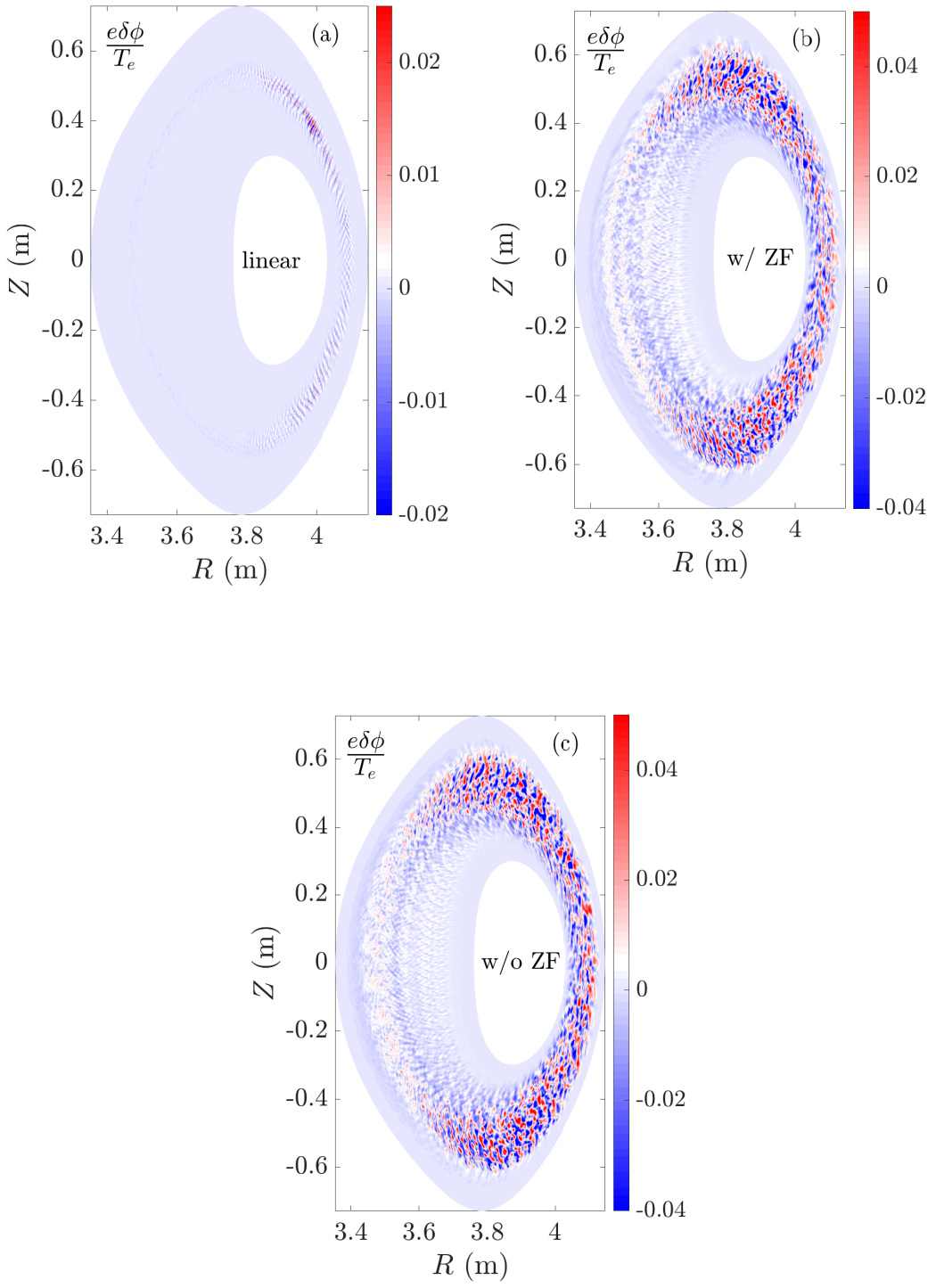

Figure 3.11 – Contour plots of the electrostatic perturbed potential in the linear phase at $t = 3.2R_0/C_s$ (a), in the nonlinear phase at $t = 6.4R_0/C_s$ with zonal flow (b) and in the nonlinear phase without zonal flow (c), of TEM turbulence simulation with kinetic electrons on a poloidal plane.

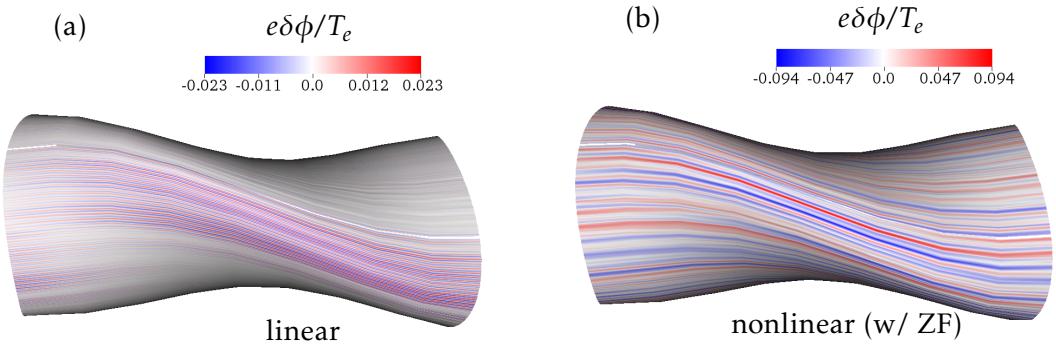

Figure 3.12 – The real space 3D contour plots of the electrostatic potential on the diagnosed flux surface with $\psi = 0.28\psi_w$ in the linear phase at time $t = 3.2R_0/C_s$ (a), and in the nonlinear phase with zonal flow at time $t = 6.4R_0/C_s$ (b).

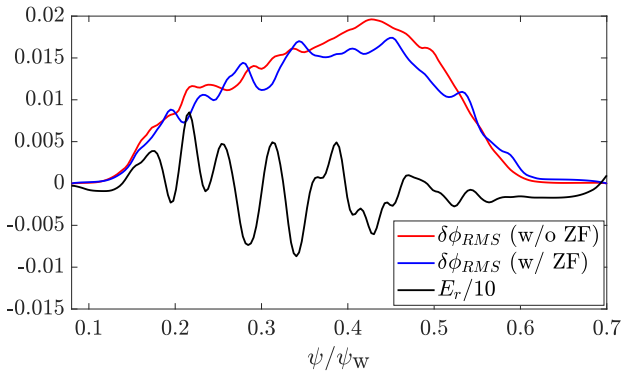

Figure 3.13 – The flux surface variation of the root-mean-squared electrostatic perturbed potential ($\delta\phi_{RMS}$) with (red line) and without (blue line) zonal flow and the radial electric field (E_r) (black line) resulting from the turbulence during the nonlinear stage of TEM turbulence simulations at time $t = 6.4R_0/C_s$. The electrostatic potential is normalized with T_e/e, and the radial electric field resulting from the turbulence is normalized with $\sqrt{T_e/e}$.

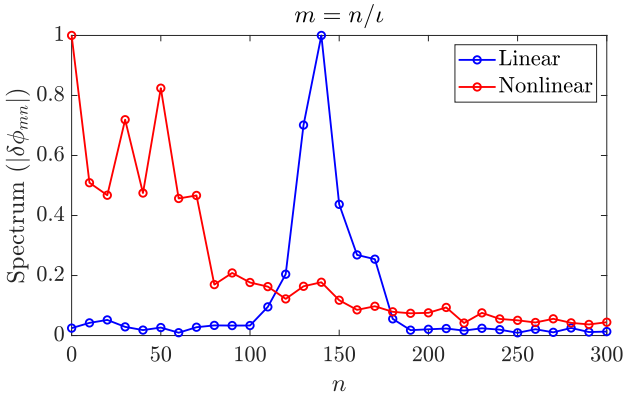

Figure 3.14 – The comparison of toroidal mode spectrum along $m = n/\iota$ in the linear and nonlinear phase of the TEM turbulence simulation.

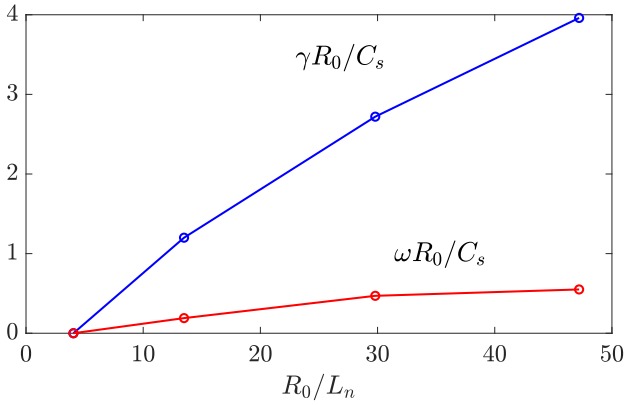

Figure 3.15 – The variation of the real frequency and growth rate of the most dominant TEM with the normalized density gradient R_0/L_n.

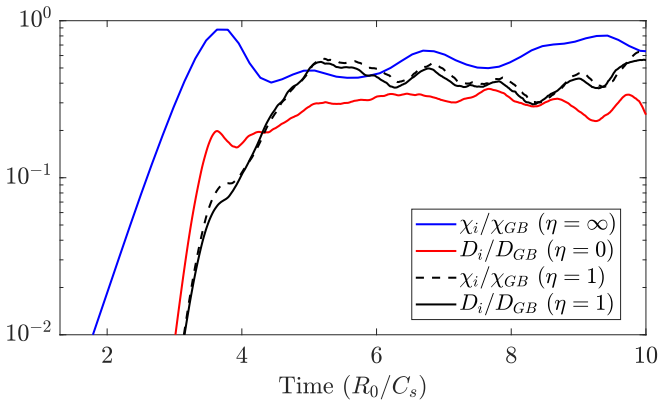

Figure 3.16 – The time history comparison of the transport averaged over $\psi \in [0.19, 0.45]\psi_w$ for $\eta = 0$, 1, and ∞.

electron temperature are 2 keV and 1 keV respectively. Based on the convergence studies, simulation parameters and mesh are the same as described in Sec. 3.3.2.

The linear spectrum shows that the dominant mode is $n = 160$, $m = 325$ with the growth rate $\gamma = 3.72 C_s/R_0$, frequency $\omega = 4.74 C_s/R_0$ and normalized perpendicular wave number $k_\perp \rho_i = 3.5$, propagating in the ion diamagnetic drift direction. So, the simulation is dominated by ITG turbulence. The electrostatic potential looks like the typical ITG mode structure localized on the outer mid-plane side. In the nonlinear phase, the zonal flow regulates the turbulent transport by reducing it by almost two times. The comparison of the turbulent transport levels for the three cases is shown in Fig. 3.16. The ion transport coefficients (χ_i, D_i) are averaged over $\psi \in [0.19, 0.45]\psi_w$. It has been confirmed that $D_e \sim D_i$. The zonal flow physics has been included in all three cases. For $\eta = 1$, two distinct saturations have been observed. The first saturation happens

at $t \sim 3.7R_0/C_s$ and the second saturation happens at $t \sim 5.0R_0/C_s$. Unlike the cases $\eta = \infty$ and $\eta = 0$, the spectrum for the $\eta = 1$ case is quite broad, comprising low and high numerical modes. The high numerical modes saturate first in the nonlinear phase while the low numerical modes saturate later which leads to two distinct saturations. The volume averaged ion diffusivity and conductivity are almost the same for the $\eta = 1$ case. The transport with $\eta = \infty$ case is the highest, while $\eta = 0$ has the lowest transport level. From this comparison, it is concluded that in the present scenario for similar plasma profile gradients, the ITG turbulence acts as the primary drive for the heat conductivity transport, whereas the TEM turbulence is effective for the particle diffusivity.

3.4 Conclusions and discussion

In this chapter, global gyrokinetic simulations of transport induced by micoturbulence arising from the pure ITG and pure TEM instabilities in the LHD stellarator have been presented. The pure ITG turbulence is excited by the gradient in ion temeperature while keeping the other profiles uniform. The effect of kinetic electrons on the ITG turbulence is studied using the hybrid model which is well-benchmarked in GTC. The kinetic electrons increase the linear growth rate of the ITG turbulence by ~ 1.5 times and the turbulent transport by ~ 2.5 times as compared to the case with adiabatic electrons. The pure TEM turbulence is excited by the density gradient in the plasma species. The eigenmode structure in the linear phase for the TEM turbulence is localized on the outer mid-plane side where the curvature is bad, similar to that in tokamaks and ITG turbulence. The TEM linear mode structure is thinner and radially localized as compared to the ITG linear eigenmode. The nonlinear simulations of TEM turbulence with and without zonal flow show that, unlike in ITG turbulence, zonal flow is not playing an important role in regulating the transport by TEM turbulence. In tokamaks, the regulation of TEM turbulence by zonal flow is weak although different works by independent codes have shown significant effect of zonal flow when some parameters are changed such as magnetic shear, electron to ion temperature ratio, electron temperature gradient and η_e [152, 163, 164]. For example, the lower magnetic shear has negligible effect on transport due to TEM turbulence. However, at larger magnetic shear, the radial streamer is easier to be broken by zonal flow due to turbulence elongation in the radial direction [152]. For cold ions and steeper electron temperature gradient, shear caused by zonal flow is weak in tokamaks [163] and also with the realisitc plasma profiles, for $\eta_e > 1$, zonal flow effect is weak [164]. Recent work in tokamaks has shown that the zonal flow excitation in TEM tur-

bulence is formally isomorphic to that of ITG turbulence, where the trapped electrons contribute implicitly only via linear dynamics [174]. Theoretically, control parameters are also identified. It could be a future study to explore the complex parameter space for the effect of zonal flow on TEM turbulence in LHD. Further, the comparison between different cases with $\eta = 0$, 1, and ∞ in LHD shows that the turbulent transport levels in the nonlinear saturation is highest for $\eta = \infty$ case and lowest for $\eta = 0$ case. Thus, in the present scenario for similar plasma profile gradients, the ITG turbulence acts as the primary drive for the heat conductivity transport whereas the TEM turbulence is effective for the particle diffusivity.

Chapter 4

Microturbulent transport in LHD stellarator with impurities

4.1 Introduction

Stellarator is gaining interest as a clean, unlimited, and viable energy source, replacing fossil fuels and fission-based reactors. In contrast to their axisymmetric counterparts: tokamaks, stellarators do not require the toroidal current, which leads to lower MHD activities, absence of disruptions, and steady-state operation [14–16]. The increased neoclassical transport at the expense of the 3D structure of the magnetic field leads to the concept of an optimized advanced stellarator in which tailoring the magnetic field allows the reduction of neoclassical transport to the level of an advanced stellarator [17–19,75,76,175]. Following this trend, an optimized magnetic configuration has been found in LHD with a strong inward shift of the magnetic axis [80]. In state-of-the-art stellarators such as large helical device (LHD) [155], the anomalous transport due to micro-instabilities remains a major cause of the degradation of plasma confinement [82, 83]. Therefore, reducing microturbulent transport is of foremost importance in stellarators. In this direction, the improvement in plasma confinement due to the injection of impurities has gained considerable attention over the past years in both tokamak and stellarator [176, 177].

Depending upon their concentration, impurities in the stellarators can significantly impact the plasma confinement. An excess concentration can lead to the degradation of plasma confinement and can cause the radiative collapse of the discharge [178, 179]. However, a controlled injection of impurities can improve the plasma confinement by reducing the microturbulent transport [66]. In this direction, recent impurity injection studies in the stellarators LHD [85, 86] and W7-X [78] have shown encouraging results. In particular, in LHD, the access to a reduced-turbulence improved confinement regime has

been observed upon the injection of boron powder into the plasma [86]. Here, the plasma temperature is observed to increase by about 25%, at the same time, the amplitude of turbulent fluctuations has been measured to decrease up to a factor of two over a broad region of the plasma volume. The reasons behind the confinement improvement are not fully understood yet, and dedicated gyrokinetic simulations can help shed light on the matter.

Advancements in high-performance computing have made it possible to validate the gyrokinetic model. Several attempts in this direction have shown that gyrokinetics accurately describes turbulence and transport in fusion plasmas [64, 65, 109, 135, 180]. However, the gyrokinetic simulations of microturbulence using realistic device geometries and experimental profiles face severe numerical challenges. For example, in realistic experimental scenarios, a wide range of spatial and temporal scales can co-exist and must be resolved. Furthermore, the cross-field particle, momentum, and energy transport due to microturbulence lead to mixing the space-time scales [45]. In addition, all the physics aspects must be incorporated into the simulations to describe the system accurately. For example, zonal flows, kinetic electron effects, neoclassical radial electric field, collisional effects, and electromagnetic effects could be significant in global gyrokinetic analyses of realistic experimental scenarios.

The neoclassical radial electric field and its shear play a vital role in the microturbulent transport. The radial electric field can change the linear growth rate of the turbulence. It can break the turbulent eddies into finer eddies by enhancing the nonlinear $\vec{E} \times \vec{B}$ shear, due to which the radial correlation length decreases, reducing the turbulence. The advancements in the neoclassical transport codes such as NTSS [181], SFINCS [182], FORTEC-3D [183] and PETA [184] have allowed an accurate description of neoclassical transport and hence have made it possible to calculate the ambipolar radial electric field in stellarators. In addition to the neoclassical radial electric field, self-generated zonal flow also plays an essential role in microturbulent transport. There are numerous investigations on the role of zonal flow in microturbulent transport for both tokamak [135] and stellarator [185]. The shear caused by zonal flow decorrelates the turbulent eddies by breaking them into finer eddies, thus, regulating the transport in the nonlinear saturation regime. Recent GTC simulations in LHD have shown that in the case of ITG turbulence, the zonal flow plays a vital role. In contrast, its effect is weak for TEM driven turbulence for which the inverse cascade of higher toroidal modes to the lower ones acts as a dominant saturation mechanism [185]. Further investigations indicate that the zonal flow effect on TEM transport depends upon several parameters such as magnetic shear, electron to ion temperature ratio, electron

temperature gradient, and the ratio of electron temperature gradient to density gradient [152, 160–165].

Recent years have shown some progress toward gyrokinetic simulations of microturbulence in stellarators. Gyrokinetic flux-tube simulations using the GKV code have been extensively performed in LHD [110–112, 186, 187], where the reduction of ITG turbulence by zonal flow, the role of zonal flow on TEM, the isotopes and collisional effects on microinstabilities, and their characteristics for high-T_i/T_e and high-T_e/T_i isotope plasmas in LHD are studied. However, flux-tube simulations fail to capture the linear coupling of multiple toroidal harmonics due to the 3D structure of the magnetic field in the stellarators and the secular radial drift of helically trapped particles across the flux surface. First global gyrokinetic simulations using the EUTERPE code with adiabatic electrons were recently carried out to study the effects of the radial electric field on the ITG turbulence in W7-X and LHD [113]. The gyrokinetic toroidal code (GTC) has been used earlier to carry out the first global nonlinear ITG turbulence simulations with adiabatic electrons in the W7-X and LHD [114]. GTC has also self-consistently calculated neoclassical ambipolar radial electric fields in the W7-X, which reduced the ITG turbulence more strongly in the electron-root case than the ion-root case [115]. Furthermore, XGC-S [116] and GENE-3D [188] have performed global gyrokinetic simulations of microturbulence in the W7-X using adiabatic electrons. The adiabatic electron model cannot address the effect of kinetic electrons on the ITG turbulence [118, 119], and the excitation of the TEM turbulence [120]. Kinetic electrons were first incorporated in the global gyrokinetic simulations of the W7-X and LHD to study the collisionless damping of zonal flow [157]. Subsequently, GTC simulation with a sufficiently high mesh resolution found a new helical trapped electron mode (HTEM) in the W7-X [158]. GENE-3D with a reduced mesh resolution has been used in recent work to simulate electromagnetic ITG turbulence with kinetic electrons in the W7-X-like plasma [159]. Recently, EUTERPE has been used for nonlinear simulations of ITG turbulence with adiabatic electrons using realistic experimental plasma parameters [169]. Recently, GTC has been used to carry out nonlinear gyrokinetic simulations to study the effect of kinetic electrons on ITG turbulence and to simulate the TEM in LHD using numerical plasma profiles [185].

In the present work, the global gyrokinetic simulations of electrostatic microturbulence for discharge # 166256 of LHD stellarator are carried out using the gyrokinetic toroidal code (GTC) [185]. In particular, the effect of injecting boron impurity powder on microturbulence is studied. GTC simulations are performed at two time instances, 5 s, and 9 s, representing the cases before

and during boron powder injection. The experimental plasma profile and LHD equilibrium are used for the simulations. The neoclassical radial electric field is taken into account in the simulations. In line with the experiment, simulations show the co-existence of ITG and TEM turbulence. ITG turbulence is dominant in the core, whereas TEM is dominant at the edge, with their respective propagations being in the ion and electron diamagnetic drift directions, respectively. For the 5 s case, the linear eigenmode frequency corresponding to ITG is ~ 20 kHz, and the TEM is ~ 80 kHz. For the 9 s case, the linear eigenmode frequency corresponding to ITG is ~ 13 kHz, and for the TEM, it is ~ 100 kHz. The nonlinear simulations show a broad poloidal wave number spectrum, $0-0.5$ mm^{-1} for ITG and $0-0.25$ mm^{-1} for TEM. Simulations by artificially suppressing the zonal flow show that the transport is greatly reduced by zonal flow in the region where ITG is dominant. In contrast, it has a comparatively weaker effect on transport in the region where TEM is dominant. These results are consistent with the recent global gyrokinetic simulations findings [185]. Zonal flow plays a vital role in regulating the ITG turbulent transport. In contrast, the inverse cascade of higher poloidal and toroidal modes to the lower modes is the dominant saturation mechanism for TEM. A comparison of the simulations done with and without boron for the 9 s case shows that the boron impurity reduces the turbulence in the entire radial domain by reducing the linear growth rate of both the ITG and TEM turbulence, consequently, the nonlinear turbulent transport. Comparing the heat conductivities for the 9 s case with the reference 5 s case shows that the ion heat conductivity values are considerably reduced in the radial range $r > 0.73a$, where the TEM is dominant. However, the ion heat conductivity is not affected in the rest of the radial domain. The electron heat conductivity also shows similar values before and during boron powder injection. This discrepancy is attributed to several possible sources: MHD activities, un-resolved low wave number fluctuations in the experiment, uncertainty in the radial electric field, unavailability of the experimental profile of boron impurity ions, and finite β effects. The comparison of effective heat conductivity is also presented between the simulation and experiment. The values are found to be in the same ballpark within the measurement uncertainty.

The remainder of the chapter is organized as follows: in Sec. 4.2, the microturbulence simulations are discussed, and conclusions are made in Sec. 4.3.

4.2 Microturbulence simulations

This section presents the electrostatic microturbulence simulations, using GTC, for the discharge # 166256 of the LHD stellarator at 5.34 s and 9 s, as discussed

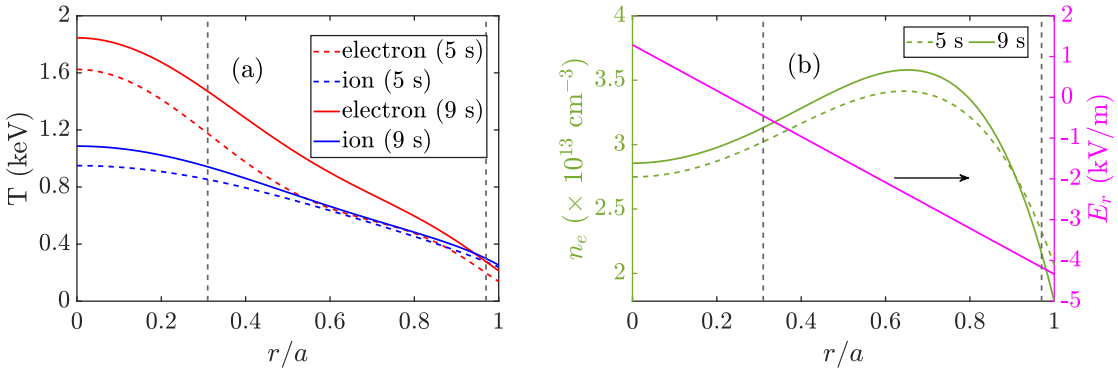

Figure 4.1 – The plasma profile for the discharge # 166256 for 5 s (dashed lines) and 9 s (solid lines) cases as a function of normalized minor radius (r/a): (a) The electron temperature (red lines) and ion temperature (blue lines), and (b) electron density (green lines) and the radial electric field (magenta line). The dashed vertical black lines represent the simulation domain.

in Ref. [86]. The time 5.34 s corresponds to the instance when there is no boron powder. In the following, we will refer to this case as 5 s for simplicity, and 9 s represents the situation with boron powder. In contrast to other low-Z impurities such as carbon, boron leads to better wall-conditioning in the experiments. However, from the perspective of the gyrokinetic simulations of microturbulence, they dictate a similar physical effect. For GTC simulations, the experimental equilibrium generated using VMEC code [145] and the experimental plasma profiles are used for the two time instances. Figure 4.1 displays the plasma profiles for the two instances, with the dashed lines corresponding to the profile for 5 s and the solid lines representing the profile for 9 s. As shown in Fig. 4.1(a), the electron and ion temperatures increase by about 25% and 20%, respectively, during boron injection. Fig. 4.1(b) shows the electron density and radial electric field. The radial electric field is represented by a magenta curve scaled on the right-hand side y-axis. The radial electric field is modeled from the SFINCS results presented in Ref. [86]. For simplicity, the radial profile of ambipolar E_r resulting from SFINCS is fitted with a linear relation with the radius, which provides a good approximation over the simulation domain. Also, since E_r is reported not to change sensibly with powder injection, the same E_r is used in this work for both the 5 s and 9 s cases. The simulation domain is represented by black dashed vertical lines, from $r \in [0.31, 0.97]a$ that corresponds to $\psi \in [0.05, 0.9]\psi_w$, where ψ is the poloidal magnetic flux and ψ_w is the value at the wall.

The normalized plasma profile gradient R_0/L_X is given in Fig. 4.2, where $1/L_X = -\frac{\partial(\ln X)}{\partial r}$ is the inverse gradient length scale, where r is the local minor radius. The dashed and solid lines correspond to the profile gradient for 5 s and

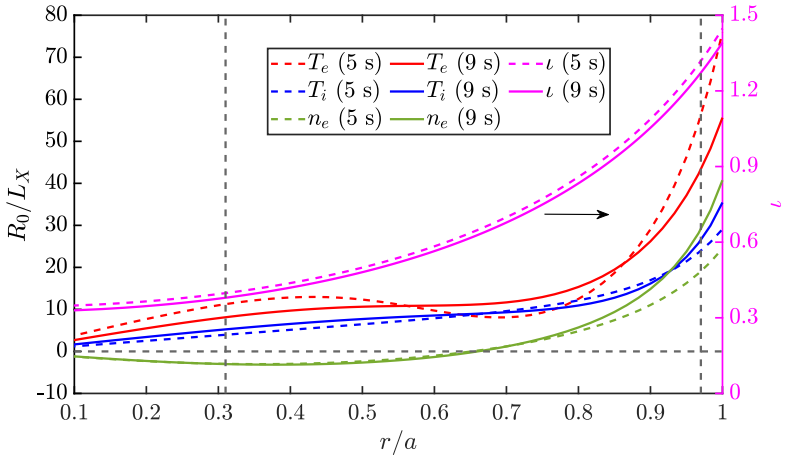

Figure 4.2 – The normalized plasma profile gradient as a function of normalized minor radius (r/a) for 5 s (solid lines) and 9 s (dashed lines) cases. The rotational transform ι is presented by magenta lines (see the y-axis on the right). The vertical black dashed lines represent the simulation domain.

9 s, respectively. Red and blue lines represent the gradient in electron and ion temperature. Green lines represent the density gradient. Magenta lines scaled on the right-hand side y-axis indicate the rotational transform $\iota = 1/q$.

In the experiment, the primary ion species is deuterium. However, other ion species, such as carbon and helium, are also present. Table 4.1 shows the concentration of each ion species along with the effective charge Z_{eff} for the 5 s and 9 s cases. All the ion species present in the experiment are fully ionized. For the 9 s case, three scenarios are discussed and labeled as I, II, and III, with different Z_{eff} and, thus, represent different boron concentrations. For case II, the experimental value of Z_{eff}=1.834 inferred from spectroscopic measurements is used as an input. For case I, an increase of Z_{eff} of $\sim$ 20% with respect to the experimental one is considered to assess the role of the increase of Z_{eff} on the plasma turbulence. This increase is consistent with the uncertainties of the experimental determination of Z_{eff}. To elucidate the effect of boron impurities on the transport in the following discussion, case III is introduced, which is similar to the case I, except the boron is removed, resulting in a lower value of Z_{eff}. For the simulations, plasma is represented by the thermal ions, electrons, and the boron impurity ions. Due to the unavailability of a realistic profile for boron impurity ions, the density and temperature profile of boron impurity ions is assumed to be the same as that of the thermal ions. For the thermal ions, the average charge and mass of the ion species are used as shown in Table 4.1. In the table, the concentration of each of the ion species is measured experimentally, from which Z_{eff}, Z_i, and a_i are calculated for each case. The density profile for the thermal ions and boron impurity ions is determined

Time	n_D/n_e	n_{He}/n_e	n_C/n_e	n_B/n_e	Z_{eff}	Z_i	a_i
5 s	0.7080	0.1389	0.0024	0.0000	1.349	1.18	2.36
9 s (I)	0.4747	0.1500	0.0017	0.0429	2.200	1.25	2.50
9 s (II)	0.5377	0.1615	0.0017	0.0228	1.834	1.24	2.48
9 s (III)	0.4747	0.1500	0.0017	0.0000	1.447	1.25	2.50

Table 4.1 – The concentration of different ion species (D - deuterium, He - helium, C - carbon, B - boron), Z_{eff} and the average charge (Z_i) and mass (a_i) of the thermal ions for 5 s and 9 s cases. For 9 s, three cases are studied, labeled as I, II, and III, corresponding to different Z_{eff}, and with different boron concentrations. All the ion species are fully ionized.

from the quasi-neutrality condition: $Z_i n_i + Z_z n_z = n_e$.

A convergence study is done to optimize the GTC parameters for the electrostatic microturbulence simulations in LHD for discharge # 166256. In this study, one-tenth of the LHD torus is simulated due to the field symmetry of the stellarator. The gyrokinetic model describes the ions, and electrons are treated according to the fluid-kinetic hybrid model, as discussed in Chapter 2. The time step size is $0.025R_0/C_s$, and 30 electron sub-cycles are used, where $C_s/R_0 = 7.069 \times 10^4$ sec^{-1} for 5 s and 7.292×10^4 sec^{-1} for 9 s where R_0 is the major radius and C_s is the ion sound speed. The value of $\rho^* = \rho_s/a$ is about 0.003 for both the time instances, where $\rho_s = c\sqrt{m_i T_e}/Z_i B$ and a is the minor radius. In the simulations, both the trapped and passing electrons are considered. For the simulations, 250 radial grid points, 2000 poloidal grid points, and 9 grid points in the parallel direction are used. The number of particles used per cell is 200.

Figure 4.3 shows the electrostatic potential on the poloidal plane in the linear phase of GTC simulations for 5 s case (4.3(a)) and 9 s (I) case (4.3(b)). The linear phase of the nonlinear simulations for the two cases shows the coexistence of ITG and TEM turbulence, propagating in the ion and electron diamagnetic directions, respectively. The ITG turbulence dominates inside the core, whereas TEM dominates at the edge for the two cases. ITG becomes unstable due to the negative density gradient and finite ion temperature gradient in the core for both 5 s and 9 s cases [189, 190]; however, $\eta_e > \eta_i$ excites the TEM near the edge (see Fig. 4.2), where η is the ratio of the temperature gradient to the density gradient. The linear eigenmode structure looks like a typical ballooning mode, localized on the outer mid-plane side where the curvature is bad. The ITG turbulence is maximum at the radial location $r \sim 0.5a$ for 5 s case and $r \sim 0.46a$ for 9 s case. However, the TEM is maximum at the radial location $r \sim 0.9a$ for 5 s case and $r \sim 0.95a$ for 9 s case. It also justifies the ex-

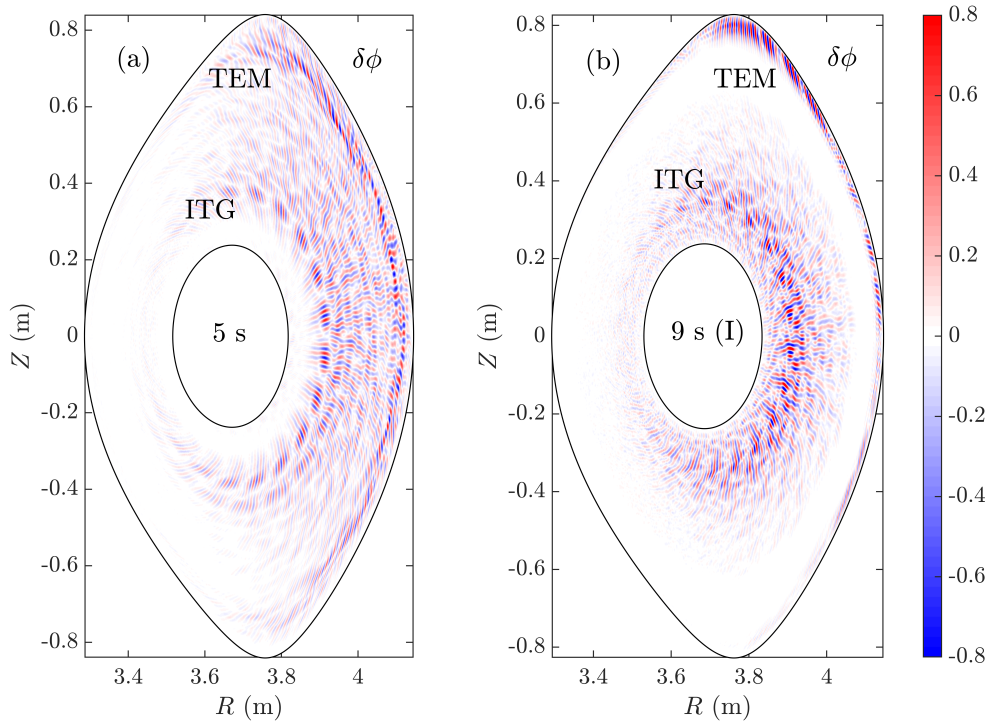

Figure 4.3 – The electrostatic potential on the poloidal plane in the linear phase for 5 s case (a) and 9 s (I) case (b). The black lines show the inner and outer simulation boundaries. The electrostatic potential $\delta\phi$ is normalized by the maximum value. For both cases, the ITG turbulence is located near the inner boundary, whereas the TEM dominates at the outer boundary.

tent of radial domain used in the simulations. Compared to the 5 s case, the radial width of the TEM for 9 s is smaller; however, the radial width of the ITG mode is large as compared to the TEM for both cases. The simulations' linear phase diagnosis has been performed at two radial locations where the ITG and TEM are dominant for each case. For the 5 s case, the diagnosis at radial location $r \sim 0.5a$ shows that the dominant ITG mode is $n = 50$, $m = 102$ with the linear growth rate of $0.44C_s/R_0$, and frequency $1.72C_s/R_0 \sim 20$ kHz. At the radial location $r \sim 0.95a$ where the TEM is dominant, the linear growth rate of the dominant TEM is $0.43C_s/R_0$, with the frequency of $7.18C_s/R_0 \sim 80$ kHz which corresponds to $n = 180$, $m = 145$ mode. For the 9 s (I) case, the diagnosis at the radial location $r \sim 0.5a$, the linear growth rate of the dominant ITG eigenmode is $0.48C_s/R_0$, with the frequency of $1.18C_s/R_0 \sim 13$ kHz, that corresponds to $n = 40$, $m = 85$ mode. At the radial location $r \sim 0.95a$ where the TEM is dominant, the linear growth rate of the dominant TEM is $0.72C_s/R_0$, with the frequency of $8.58C_s/R_0 \sim 100$ kHz, that corresponds to $n = 200$, $m = 169$ mode. The frequencies of the ITG and TEM for both 5 s and 9 s cases are in

good agreement with the experiment [86], where it has been discussed that the fluctuations spectrum, measured using phase contrast imaging setup, before boron powder injection, peak at ~ 20 kHz, identified as ITG turbulence, and TEM is observed at the plasma edge with the peak in spectrum at ~ 80 kHz. However, during boron powder injection peak corresponding to the ITG turbulence shifts to ~ 10 kHz, and at the edge plasma where TEM is dominant, a new peak emerges in the spectrum in the range $\sim 100 - 200$ kHz (see Fig. 5(c) in Ref. [86]).

To study the effect of boron impurities on microturbulence, GTC self-consistent simulations are carried out for the cases 9 s (I), (II), and (III) that represent the cases with a boron concentration of 4.29%, 2.28%, and 0% respectively. The linear simulation phase for 9 s (II), (III) shows the poloidal electrostatic potential similar to that of 9 s (I) as shown in Fig. 4.3(b). However, for the 9 s (II) case, the growth rate of the dominant ITG mode is $0.49C_s/R_0$ at radial location $r \sim 0.5a$, and the growth rate of the dominant TEM is $0.64C_s/R_0$ at $r \sim 0.95a$. Similarly, simulations of the 9 s (III) case show that the growth rate of the most dominant ITG mode is $0.56C_s/R_0$ at radial location $r \sim 0.5a$. In contrast, the growth rate of the most dominant TEM is $0.64C_s/R_0$ at radial location $r \sim 0.95a$. Thus, for the 9 s (I) case, the boron impurity reduces the ITG turbulence growth rate by $\sim 14\%$, and TEM by $\sim 5\%$. For the 9 s (II) case, the ITG turbulence growth rate is reduced by $\sim 12\%$ and TEM by $\sim 16\%$ due to the boron impurity.

In the nonlinear simulation phase, the turbulence spreads throughout the simulation domain due to the nonlinear coupling between the different toroidal modes and the turbulence interaction with the self-generated zonal flow $n = 0$ and $m = 0$. Figure 4.4 shows the electrostatic potential on the poloidal plane in the nonlinear phase of the simulation for 5 s case (4.4(a)) and 9 s (I) case (4.4(b)). It is important to note that the electrostatic potential on the poloidal plane is shown only for case 9 s (I), as the turbulent eddies look similar to Fig. 4.4(b) for 9 s (II) and (III) cases, though the fluctuations amplitudes are different. Also, Fig. 4.4 shows that the electrostatic fluctuations in the outer region $r > 0.73a$ are reduced.

Zonal flow and microturbulence are ubiquitous in fusion plasmas. The role of zonal flow on microturbulence is studied by artificially suppressing the zonal flow in the simulations. Figure 4.5 shows the ion heat conductivity with zonal flow (red lines) and without zonal flow (blue lines) for 5 s (dashed lines) and 9 s (solid lines) cases. The zonal flow substantially reduces the turbulent transport at the location where the ITG turbulence is dominant; however, it has a weak effect near the edge, where the TEM is dominant. The relatively weaker effect of zonal flow on TEM turbulent transport can also be seen in Fig. 4.4. For

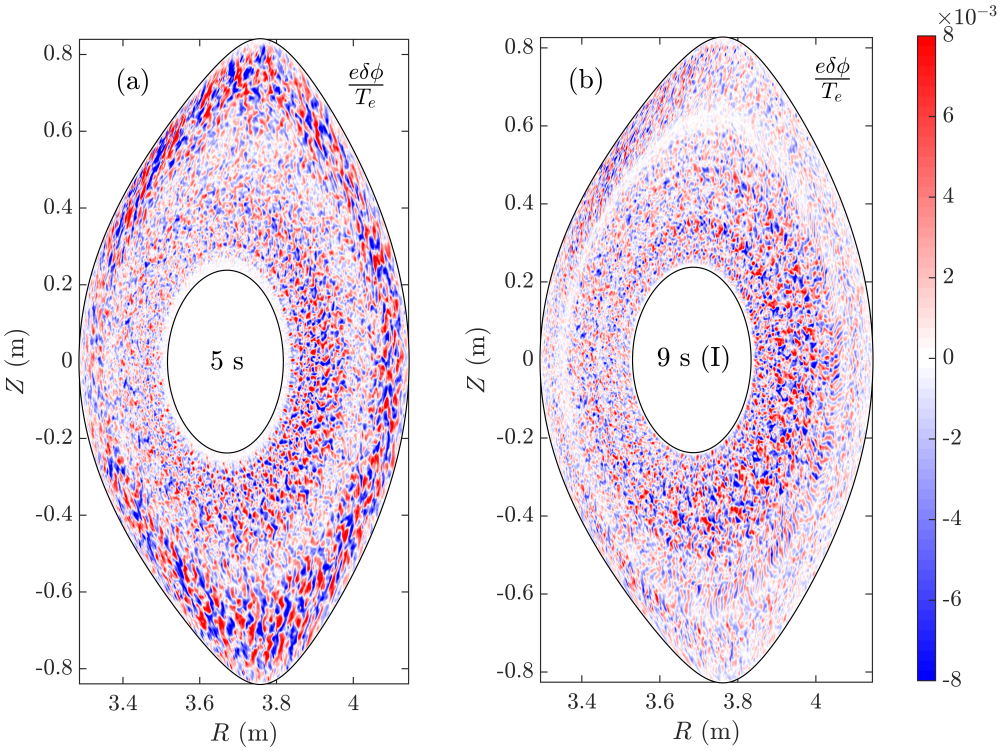

Figure 4.4 – The electrostatic potential on the poloidal plane in the nonlinear phase for 5 s (a) and 9 s (I) (b). The black lines show the inner and outer simulation boundaries. The electrrostatic potential is normalized by T_e/e. Compared to 5 s cases, the turbulence is reduced in the outer region $r > 0.73a$.

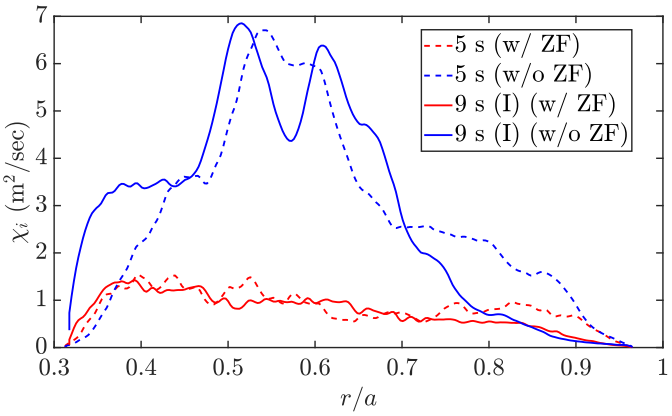

Figure 4.5 – The radial variation of the time-averaged ion heat conductivity for 5 s case (dashed lines) and 9 s (I) case (solid lines), with the zonal flow (red lines) and without zonal flow (blue lines).

example, as shown in the figure, the size of the electrostatic potential eddies is smaller in the core where the ITG is dominant as compared to eddies near the edge where TEM is dominant. Thus the zonal flow is more effective in

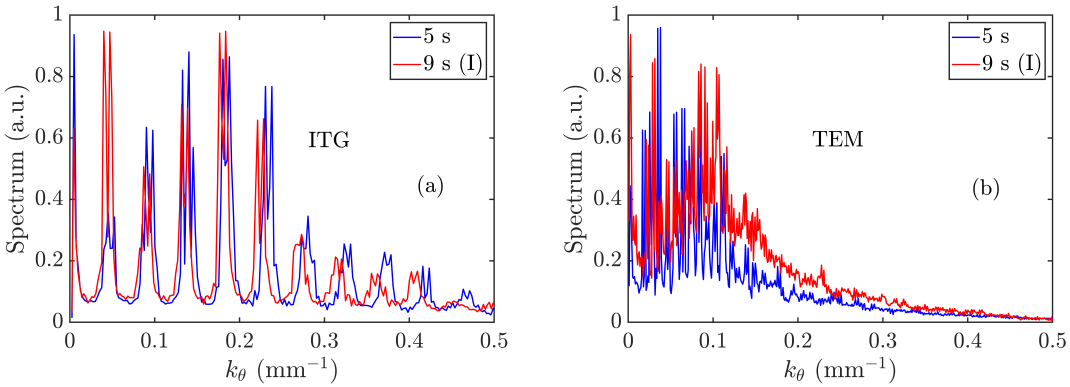

Figure 4.6 – The poloidal wave number spectrum for 5 s (blue) and 9 s (I) (red) cases for ITG (a) and TEM (b) turbulence.

breaking the potential eddies into finer eddies for ITG than TEM. These results are consistent with the earlier investigations [185], where it has been found that the zonal flow plays a crucial role in regulating the ITG turbulent transport. However, it has a relatively weaker effect on the TEM turbulent transport; the inverse cascade of the higher poloidal and toroidal modes to the lower ones dominates the nonlinear saturation. It is worth mentioning that there has been a significant discussion on the role of zonal flow on microturbulence for axis-symmetric tokamaks [135, 152, 160–165, 185] where it is shown that the zonal flow acts as a dominant mechanism for the ITG turbulence saturation, whereas it has a relatively weaker effect on TEM turbulence. It is also known that the role of TEM turbulence depends upon details of the plasma profile and several parameters for tokamak [166] and stellarator [167].

Figure 4.6 represents the time-averaged poloidal wave number spectrum in the nonlinear simulation phase corresponding to the ITG turbulence (4.6(a)) and TEM turbulence (4.6(b)) for 5 s (blue lines) and 9 s (I) (red lines) case. The poloidal spectrum is normalized with the maximum values. Case I is discussed for 9 s, as case II shows the poloidal wave number spectrum similar to the case I. It is essential to see that the wave number spectrum involves equally spaced discrete peaks, as the simulations use one-tenth of LHD torus. The separation between the peaks is proportional to the local safety factor value $q = 1/\iota$. The peaks are more closely spaced for TEM than for ITG, as the safety factor at the location where ITG is dominant is $q \sim 2.0$, whereas at the radial location where TEM is dominant, the safety factor $q \sim 0.8$. It is also worth discussing that in Fig. 4.6(a), there is a gradual shift in the peaks for 5 s and 9 s cases as k_θ increases. It is due to the slight difference in the rotational transform values for the two cases, as shown by the magenta lines in Fig. 4.2. The wave number spectrum is broad with $k_\theta \in [0, 0.5]$ mm^{-1} for ITG and $k_\theta \in [0, 0.25]$

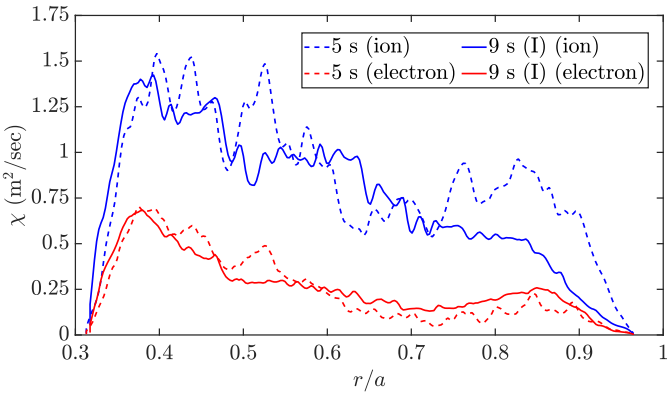

Figure 4.7 – The radial variation of the time-averaged ion (blue lines) and electron (red lines) heat conductivity for 5 s (dashed lines) and 9 s (I) (solid lines) cases.

mm^{-1} for TEM, for both 5 s and 9 s (I). The simulations show that a substantial fraction of the turbulent spectrum for ITG and TEM is for $k_\theta < 0.1$ mm^{-1}. While overall, this part of the spectrum does not seem to change much between the 5 s and 9 s cases. However, the phase contrast imaging diagnostic used in the measurements has a cut-off at about 0.1 mm^{-1} as shown in Figs. 4(c), 4(d) of Ref. [86], so that the measurements do not resolve the low wave number part of the spectrum [191]. It makes the direct comparison with the experimental measurement of turbulence fluctuations more challenging.

Figure 4.7 shows the radial variation of time-averaged ion (blue lines) and electron (red lines) heat conductivity at 5 s case (dashed lines) and 9 s (I) case (solid lines). In the nonlinear phase, the transport saturates due to nonlinear mode coupling between different toroidal and poloidal modes and due to the interaction of turbulence with the self-generated zonal flow. The heat conductivities are time-averaged over a time window of $12.5R_0/C_s$, in the nonlinear steady state. As shown in the figure, the ion heat conductivity substantially reduces during the boron injection (solid and dashed blue lines) in the radial range $r > 0.73a$, in the region where the TEM is dominant. However, in contrast to the experiments, the ion heat conductivity values are almost similar in the rest of the radial domain. The electron heat conductivity also shows similar values for 5 s and 9 s (I) cases.

It is essential to review the possible sources of the discrepancy. For example, MHD activity is present in the experiments both before and during powder injection, and the level of MHD activity is overall the same for the two cases. Therefore, a change in MHD activity is to be excluded as the cause of confinement improvement upon powder injection. The simulations also show that a substantial fraction of the turbulent spectrum for ITG and TEM is for $k_\theta < 0.1$ mm^{-1}. While overall, this part of the spectrum seems to stay mostly

the same between the 5 s and 9 s cases. Indeed, the phase contrast imaging diagnostic used in the measurements in Ref. [85] has a cut-off at about 0.1 mm^{-1}, so the measurements do not resolve the low wave number part of the spectrum [191]. It makes the direct comparison with the experimental measurement of turbulence fluctuations amplitude more challenging. As mentioned earlier, the radial electric field used in the gyrokinetic simulations is calculated using SFINCS [182], which shows that the E_r remains the same during boron powder injection [86]. However, these calculations are radially local and do not consider the impact of the flux surface variation of the electrostatic potential [192] as well as tangential magnetic drifts. It has been shown that the global effects and potential variation, which are challenging to incorporate in SFINCS simulations due to numerical complexity, can alter the calculated radial electric field [193]. So, there is a possibility that the ambipolar radial electric field also changes during boron injection and could affect the simulated turbulent transport, as the ambipolar radial electric field can significantly affect the transport due to $\vec{E} \times \vec{B}$ shear [113]. Also, due to the measurement limitations in the experiments, the density and temperature profile of boron impurity ions have been assumed to be the same as that of the thermal ions. The realistic boron profile could also affect the transport. Furthermore, the findings of this work are based on the global gyrokinetic simulations in the electrostatic limit. From Fig. 4.1, it is clear that the plasma β increases during boron powder injection. The electromagnetic effects can considerably affect the microturbulent transport depending upon the β values [194]. Though the overall β values for the analyzed discharge are relatively small to cause a transition from electrostatic turbulence to electromagnetic one, for example, ITG to KBM (kinetic ballooning mode) [195], it is still quite reasonable to expect that in the finite β limit, the gyrokinetic simulations could show a further reduction in turbulence and transport, due to an increase in β [159, 196] during boron injection. Moreover, the electromagnetic effects on microturbulence are more precisely described by the global simulations, as, in addition to the appearance of magnetic fluctuations, finite β effects lead to the modifications of the electrostatic fluctuations as well. These fluctuations have an additional component that varies substantially across the flux tubes. Thus the local simulations cannot accurately capture these effects and are best described by the global simulations.

To better understand the effect of boron on transport, further investigations are made. The nonlinear heat transport is compared for cases 9 s (I), (II), and (III), which correspond to different boron concentrations. Figure 4.8 shows the radial variation of the time-averaged ion (solid lines) and electron (dashed lines) heat conductivity for three different concentrations of boron, 0%

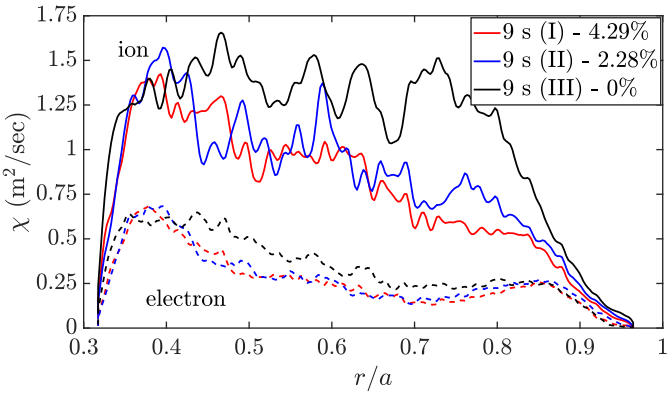

Figure 4.8 – The radial variation of the time-averaged ion (solid lines) and electron (dashed lines) heat conductivity for 9 s case with three different concentrations of boron impurities.

(black lines), 2.28% (blue lines), and 4.29% (red lines). The figure illustrates that the boron, as the impurities, substantially reduces the transport. In this context, earlier work by different researchers has shown that the impurities affect the ITG and TEM turbulence differently. It depends on parameters such as impurity concentration, the direction of the impurity density gradient, profile gradients, and change in shearing due to zonal flow [197]. For example, the recent gyrokinetic simulations show that the impurities reduce the ITG turbulent transport due to the dilution effect, where the impurity ions replace the thermal ions or by changing the $\vec{E} \times \vec{B}$ shearing due to zonal flow [198]. However, the heat conductivity values obtained from the simulations for 5 s and 9 s cases have similar values with and without zonal flow (see Fig. 4.5). Therefore, the reduction of transport in the region where the ITG is dominant is mainly due to the dilution of thermal ions by the boron impurities. Detailed analysis using the gyrokinetic integral eigenmode equations has shown that the effect of impurities on the TEM driven turbulence depends upon the parameters, for example, the electron temperature gradient and the peaking direction (inward/outward) of the impurity density profile [199]. However, the impurity ions stabilize the TEM turbulence in case of the large electron temperature gradient, irrespective of the peaking direction of the impurity density profile. As shown in Fig. 4.2, the electron temperature gradient is large for both 5 s and 9 s cases; hence the boron ions decrease the TEM transport. Thus the boron impurity ions reduce the turbulent transport.

Figure 4.9 shows the radial variation of the time-averaged ion (blue) and electron (red) heat conductivity for 5 s (dashed) and for 9 s (III) (solid), i.e., without taking into account boron impurity ions in the gyrokinetic simulations. As there is a change in plasma profile during boron powder injection (see Fig. 4.1), the heat conductivity values for both ions and electrons are in-

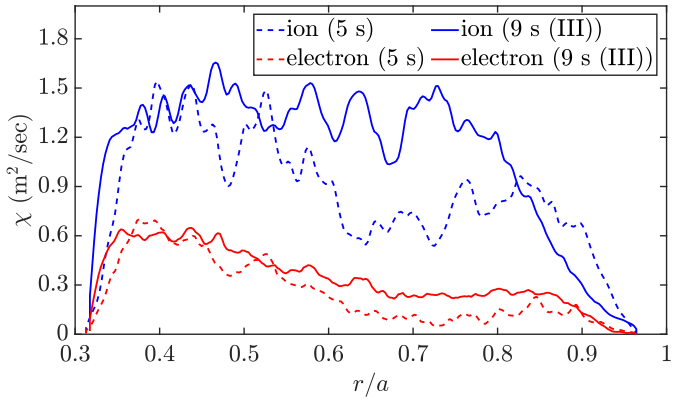

Figure 4.9 – The radial variation of the time-averaged ion (blue lines) and electron (red lines) heat conductivity for 5 s (dashed lines) and 9 s (III) (solid lines) cases, without considering boron impurity ions in gyrokinetic simulations.

creased during boron powder injection, except the reduction in ion heat transport for $r > 0.82a$, which is due to the reduction of TEM turbulent transport due to profile modification. These results are supported by recent findings of impurity injection studies in W7-X, where the confinement improvement has been attributed to the impurity-induced profile modifications [78].

Therefore, the effect of boron powder on turbulent transport is two-fold. First, boron powder changes the microturbulent transport dynamics due to impurity ions. Second, the boron powder injection leads to a change in the plasma profile, which changes the instability drive for the turbulence due to the change in profile gradient. Figs. 4.8 and 4.9 describe these effects, respectively. Thus, the reduction in transport during boron powder injection is a combined effect of the presence of boron as the impurities and the change in plasma profile due to boron.

Furthermore, Fig. 4.10 compares the effective heat conductivity from the experiment and simulations. The shaded region represents the experimental uncertainties in the heat conductivity values for 5 s and 9 s cases. Experimentally, the effective heat conductivity is computed by the DYTRANS code [200] using the following relationship

$$\chi_{\text{eff}} = \frac{Q_e + Q_i}{n_e dT_e/dr + n_i dT_i/dr},$$

where Q_e and Q_i are the electron and ion heat flux, r is the local minor radius. As discussed earlier, the simulation domain is restricted to $r \in [0.31, 0.97]a$, and the fluctuating quantities are enforced to zero using the Dirichlet boundary condition at the simulation boundaries. The simulations show the radial trend of the effective heat conductivity, similar to the observed trend in the experiments before and during powder injection. In addition, the χ_{eff} from

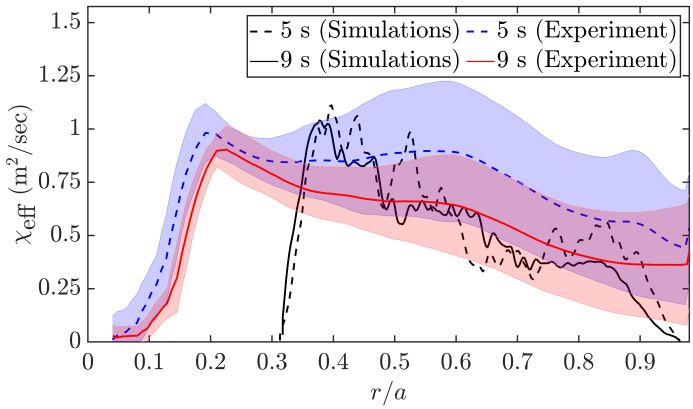

Figure 4.10 – Comparison of the radial variation of the effective heat conductivity from experiments and simulations. The experimental values are represented by a dashed blue line for 5 s and a solid red line for 9 s, with the shaded regions representing the measurement uncertainty in the experiment. The simulation results are shown by black lines (dashed line for 5 s and solid line for 9 s). The simulated values are enforced to vanish at the simulation boundaries by applying the Dirichlet boundary condition.

simulations and experiments are in the same ballpark estimate within the measurement uncertainty.

4.3 Conclusions and discussion

To summarize, in this work, we have carried out the global gyrokinetic simulations of the electrostatic microturbulent transport of the discharge # 166256 of the LHD stellarator in the presence of boron impurities, using the gyrokinetic toroidal code (GTC). The radial electric field has been considered in the simulations. When there is no boron, the reference case is represented by a snapshot status of the plasma state at time t = 5 s. It is contrasted with the state of the plasma during boron injection at t = 9 s. At both time instances, the experimental plasma profile and the corresponding LHD equilibrium have been used for the simulations. GTC simulations show the co-existence of ion temperature gradient (ITG) turbulence and the trapped electron mode (TEM) before and during boron powder injection. ITG turbulence is dominant in the core, whereas the TEM dominates near the edge. The linear eigenmode frequency of the dominant ITG mode is $\sim$ 20 kHz, that during boron injection, down-shifts to $\sim$ 13 kHz. The linear eigenmode frequency of the dominant TEM is $\sim$ 80 kHz, that during boron injection, up-shifts to $\sim$ 100 kHz. These results are in good agreement with the experiment. Boron impurities reduce both the linear growth rate and the nonlinear turbulent transport. The nonlinear simulations

by artificially suppressing the zonal flow show that the zonal flow substantially reduces the ITG turbulent transport; however, it has a comparatively weaker effect on the TEM transport for both cases. Comparison of the heat conductivity for different boron concentrations shows that the boron impurities reduce the transport. Comparison of the heat conductivity transport for the 9 s case with that of the 5 s case shows that the ion heat conductivity is substantially reduced in the radial range $r > 0.73a$. However, the average ion heat conductivity in the rest of the radial range and the electron heat conductivity in the whole radial range show similar values. The comparison of the effective heat conductivity between simulations and experiments is presented, and the values are in the same ballpark estimate within the measurement uncertainty. The discrepancy in the nonlinear transport between simulations and experiment is reviewed. For example, the neoclassical radial electric field is computed by SFINCS, which can differ from the actual electric field since effects such as self-organization due to turbulence and zonal flows are not included in the neoclassical simulations. In the experiments, MHD activity is present both before and during powder injection, and the level of MHD activity is overall the same for the two cases. Therefore, a change in MHD activity is to be excluded as the cause of confinement improvement upon powder injection. The reduction of transport due to impurities could differ from when an actual profile of boron ions is considered. Also, due to diagnosis limitations in the experiment, the wave number spectrum for the fluctuations below 0.1 mm^{-1} is unavailable. However, the simulations show considerable turbulence activity below 0.1 mm^{-1} for ITG and TEM, though it is similar before and during powder injection. This makes the direct comparison with the experimental measurement of turbulence fluctuations amplitude more challenging. In this work, the electrostatic simulations are presented; however, the experiments show an increase in β during boron powder injection though the analyzed discharge's overall β values are quite small. Thus, it is reasonable to expect a further reduction in transport (particularly of the ITG turbulence) due to the finite β effects.

Chapter 5

Electrostatic microturbulence in ADITYA-U tokamak

5.1 Introduction

In fusion reactors [2, 4], the energy and particle confinement time must be long enough to achieve a net energy balance between the energy supplied to heat the system and the energy produced by the fusion process in the plasma. The energy and particle losses observed in magnetic fusion experiments are significantly higher than predicted values for the collisional processes [44]. This so-called anomalous transport is believed to be primarily due to small-scale instabilities called micro-instabilities caused by the temperature and density gradient of plasma species [45]. Therefore, understanding the physics of turbulent transport is of paramount importance in magnetically confined plasma experiments. The design of future reactors relies on the extrapolation of the turbulent transport levels from current fusion experiments to much larger future experiments such as the International Thermonuclear Experimental Reactor (ITER) [11, 30].

Thanks to the spectacular advances in high-performance computing, it has become possible to carry out large-scale numerical simulations, using various plasma models, to study the characteristics of turbulence and transport. For example, simulation results using sophisticated gyrokinetic codes [103] have shown good agreement with experimental observations from tokamaks. An important objective of these simulations is to find a physical basis for the empirical scaling of the turbulent transport levels from first-principles, state-of-the-art numerical modeling [88, 128, 201]. Advanced gyrokinetic simulation codes enable an in-depth study of small-scale turbulence, such as that arising from drift waves, that is widely believed to be the cause of anomalous transport [45]. Various simulation codes treat the problem at different levels of complexity to

capture some of the crucial physics features, related to the small-scale modes like the ion temperature gradient (ITG) and the trapped electron mode (TEM).

Many gyrokinetic simulations of electrostatic microturbulence using realistic device geometry and experimental plasma profiles have found the signatures of ITG/TEM turbulence. For example, a comparison of the experimentally measured plasma fluctuations and turbulent transport is made against the local electrostatic gyrokinetic simulations of L-mode discharge of the DIII-D tokamak using the GS2 code [64], in which the ITG turbulence was investigated. The nonlinear electrostatic gyrokinetic simulations of L-mode discharge of DIII-D using the GYRO code show similar electron temperature and density fluctuations in the ITG/TEM unstable plasma, consistent with the experimental observations [65]. Similarly, a validation study of the gyrokinetic electrostatic simulations using GYRO code has been done for the ITG and TEM dominated L-mode plasmas of Alcator C-Mod tokamak [109].

Collisions and zonal flow can significantly affect the turbulence and transport in tokamaks. The zonal flow interaction with the turbulence has been extensively studied. For example, it is widely accepted that the zonal flow plays an essential role in regulating the ITG turbulent tranpsort [49, 93]. However, in contrast to the ITG turbulence, the effect of zonal flow on the TEM turbulent transport is found to depend on the parameters such as the electron to ion temperature ratio, magnetic shear, the electron temperature gradient scale length, and the ratio of electron temperature gradient to density gradient [152, 163–166]. The collisions can effect the turbulence and transport directly by affecting the linear microturbulence drive or indirectly by affecting the coherent phase space structure. It has been found that the collisional effects can reduce the ITG turbulence growth rate, can lead to the stabilization of TEM turbulence, or can lead to a transition from TEM to ITG turbulence by the de-trapping of electrons [151–153]. The recent gyrokinetic simulations using gyrokinetic toroidal code (GTC) have shown the effects of collisions on the ITG and TEM dominant discharges of the DIII-D tokamak [154].

GTC has been applied extensively to tokamaks [93] to study turbulent transport. Recently, GTC was upgraded to simulate turbulence in the 3D devices called stellarators [114, 157, 185], as discussed in Chapters 3 and 4. In the present work, we have used GTC to study the microturbulence in the ADITYA-U tokamak. ADITYA-U is a medium-sized, air-core tokamak, that has recently been upgraded from the ADITYA tokamak [70–73] to incorporate a new set of divertor coils for shaped plasma operations with a new vacuum vessel along with a new toroidal belt limiter. Since its commissioning, several experiments relevant to the operation of future fusion devices such as ITER have been per-

formed [71–73], including experiments on generation, transport and control of runaway electrons [72,73], plasma disruption [72,73], transient transport phenomena such as cold-pulse propagation [73,74] and plasma detachment [73]. However, there are very few simulation studies on the ADITYA-U tokamak, and even the global simulation studies of the microturbulence by state-of-the-art codes like GTC are yet to be established.

In the present work, self-consistent gyrokinetic simulations have been carried out using GTC to investigate the role of electrostatic microturbulence, such as ITG and TEM, in driving the turbulent transport in the circular plasmas (limiter plasmas) of the ADITYA-U tokamak. The ion diffusivity and electron heat conductivity values estimated from the experiments are in fair agreement with the values obtained from the simulations. The turbulent fluxes are found to be driven by TEM in ADITYA-U. The simulated frequency spectra of electrostatic fluctuations match well with those measured using Langmuir probes in the edge region of the plasma. The simulations with and without collisions show that the collisional effects suppress the turbulence and transport to a certain extent. The nonlinear simulations show that the zonal flow is not playing a crucial role in the nonlinear saturation, which is dominated by the inverse cascade of the higher poloidal and toroidal modes to the lower ones. These simulation findings could be helpful in setting up future experiments in the ADITYA-U tokamak. The present work is the first ever simulation study to understand the turbulence and transport in ADITYA-U. As a first step, electrostatic simulations have been carried out. The electromagnetic effects could have a significant impact on turbulence and transport [194]. It could be a future work to discuss the electromagnetic simulations of microturbulence in ADITYA-U.

This chapter is presented as follows: the geometry, equilibrium quantities, and experimental results for the ADITYA-U tokamak discharge # 33536 are discussed in section 5.2. In section 5.3, linear and nonlinear simulations of the microturbulence are discussed. In section 5.4, the conclusions have been made.

5.2 ADITYA-U experiment

ADITYA-U is a medium-sized tokamak with a major radius of 0.75 m and a minor radius of 0.25 m [70–73]. For the present simulation, a hydrogen (main ion) plasma discharge # 33536 has been used, in which the plasma is operated in the limiter configuration. The plasma parameters of the discharge are plasma current ~ 150 kA, central chord-averaged density $\sim 2.3\times10^{19}$ m^{-3}, central chord-averaged electron temperature ~ 250 eV and ion temperature ~ 80 eV. The radial profile of plasma density has been obtained from a multi-channel

microwave interferometer [74, 202]. The radial profile of electron temperature is reconstructed using multi-chord soft X-ray emission intensity measurements in the core plasma region, and the Langmuir probe (single/triple) is used for the spectral analysis of edge temperatures [74]. The core ion temperature is measured using spectroscopic diagnostics [203]. The radial profile of ion temperature is assumed to be the same as the plasma pressure profile. Figure 5.1a shows the equilibrium mesh on the poloidal plane for discharge # 33536 obtained with IPREQ code [144]. The black lines in the figure represent the curves of a constant poloidal angle, while the contours represent the poloidal flux normalized with the value at the last closed flux surface, ψ_X. Figure 5.2 illustrates the 3D real space contour plot of the magnetic field amplitude normalized to the value on the axis at flux surface with $\psi = 0.88\psi_X$. The on-axis magnetic field B_0 is 1.44 T, the distance at the magnetic axis R_0 is 0.7641 m. Figure 5.1b shows the safety factor profile obtained from the equilibrium simulations carried out using IPREQ code [144] and the normalized minor radius as a function of normalized poloidal flux. The equilibrium quantities for the ADITYA-U discharge are written in cylindrical coordinates that are transformed to magnetic Boozer coordinates to be used as input to GTC. The edge region (region near to the last closed flux surface) of the ADITYA-U tokamak is thoroughly diagnosed by several sets of Langmuir probes [74]. A broadband fluctuation spectrum is observed in the frequency range of ~ 0 to 50 kHz in the measured density fluctuations sampled at 100 kHz. The rack-Langmuir probes [74] are also used for measurements of the radial profile of density in the edge regions. The density fluctuations are measured using both single and triple Langmuir probes in ADITYA-U. The density in the edge region in the present study is measured from the ion-saturation current drawn by the probe. Density fluctuations are generally large in magnitude in comparison to the temperature fluctuations and hence the temperature fluctuations are ignored in the density fluctuations estimation [204]. Ion-saturation current measurements represent the density fluctuations quite well, especially close to the last closed flux surface ψ_X of the tokamak [205]. The
variation in the magnitude and frequency of density fluctuations from shot-to-shot measurements in the set of represented discharges of ADITYA-U remains within 10%. For the simulations, the mean density and temperature profiles are used. The particle diffusivity of ~ 0.2 m^2/sec in the edge region is derived from these measured density profiles [206], which are further cross-checked with UEDGE code simulations [207]. The energy confinement time is calculated by $\tau_E = W/(P - dW/dt)$, which is the ratio of stored energy to the input power (ohmic minus the power transferred to the plasma), that gives $\tau_E \sim 10$ msec

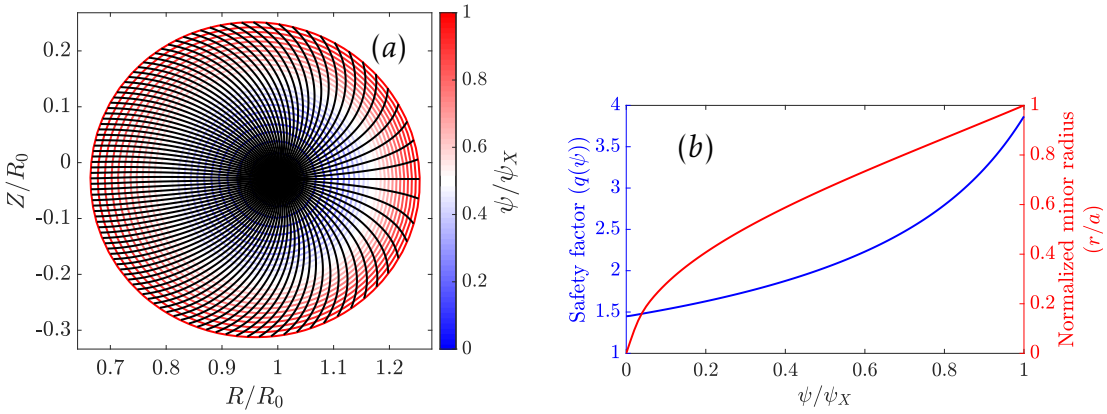

Figure 5.1 – Equilibrium mesh on the poloidal plane (a). The contours show the poloidal flux normalized to the value at the last closed flux surface ψ_X and the black lines are the curves of constant poloidal angle and the safety factor (blue curve) and normalized minor radius (red curve) as a function of the normalized poloidal flux (b) for ADITYA-U discharge # 33536.

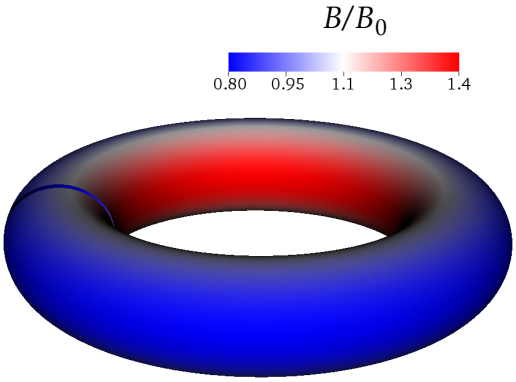

Figure 5.2 – The 3D real space contour plot of the magnetic field amplitude normalized to the value on the axis on the flux surface with $\psi = 0.88\psi_X$ for ADITYA-U discharge # 33536.

Minor radius	0.25 m
Major radius	0.75 m
On-axis magnetic field	1.44 T
On-axis electron temperature	250 eV
On-axis ion temperature	80 eV
On-axis electron density	2.3×10^{19} m^{-3}
Energy confinement time	$\sim$ 10 msec
Ion acoustic speed	1.55×10^{5} m/sec
Ion gyro-radius	6.34×10^{-4} m
Electron gyro-radius	2.61×10^{-5} m
Ion thermal velocity	8.76×10^{4} m/sec
Electron thermal velocity	6.63×10^{6} m/sec

Table 5.1 – ADITYA-U tokamak and plasma parameters for a typical experimental discharge.

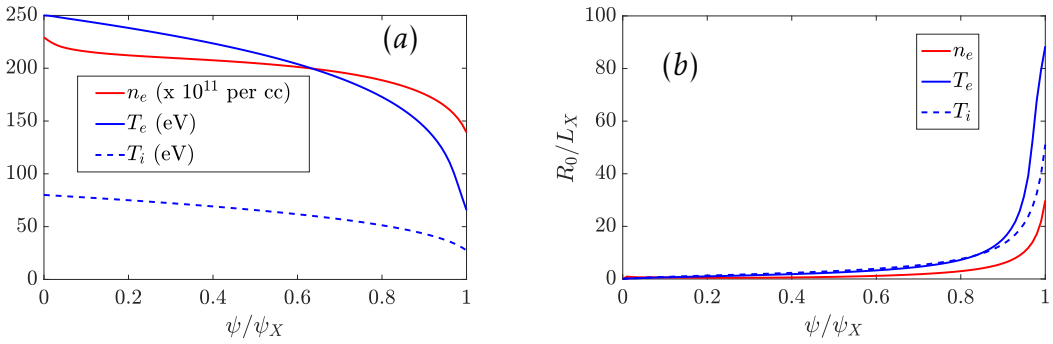

Figure 5.3 – The profiles (a) and the corresponding normalized gradient (b) being used for the microturbulence simulations of ADITYA-U discharge # 33536.

[206]. A ballpark estimate of the electron heat conductivity, which is based on the diffusive transport, is given by the scaling of the energy confinement time with plasma size: $\tau_E \sim a^2/4\chi_e$ [208], which gives $\chi_e \sim 1.5$ m^2/sec. The various ADITYA-U parameters and plasma parameters are shown in Table 5.1 for a typical experimental discharge.

5.3 Microturbulence simulations

This section presents the electrostatic gyrokinetic simulations of the low-frequency drift wave instabilities driven by the gradient in the plasma density and temperature, performed using GTC. Figure 5.3 shows the plasma profile (6.1) and the corresponding normalized gradient R_0/L_X (5.3b) used in simulations, where L_X is the profile gradient scale length given by $1/L_X = -\partial(\ln X)/\partial r$, r is the local minor radius. The gradient in the plasma profile is steep at the last closed

flux surface (LCFS), which can drive electrostatic instabilities such as ion temperature gradient (ITG) instability, trapped electron mode (TEM) instability. The simulation domain is from $\psi_{\text{inner}} = 0.1\psi_X$ to $\psi_{\text{outer}} = 1.0\psi_X$, where the poloidal flux ψ values are normalized to the value at the last closed flux surface ψ_X. The ion species is the proton, and their dynamics is described by the gyrokinetic equations, and the electrons are treated kinetically, according to the fluid-kinetic hybrid model, as described in Chapter 2. Both the passing and trapped electrons have been included in the simulations. The proton to electron mass ratio is $m_p/m_e = 1836$. GTC uses three meshes: equilibrium mesh, as shown in Fig. 5.1a, turbulence mesh, and neoclassical mesh. For the simulations, 200 radial grid points, 3000 poloidal grid points, and 32 grid points in the parallel direction are used for the turbulence mesh. The microturbulences under investigation are ITG and TEM that satisfy $k_{\|} << k_{\perp}$, thus the turbulence mesh requires fewer grid points in the parallel direction as compared to the radial and poloidal grid points. The radial, poloidal, and toroidal grid numbers used for the neoclassical mesh are 64, 64, and 32, respectively, based on the convergence studies. First, the time step convergence is done, followed by the convergence of electron subcycles, and finally, the convergence for particle number is done. The time step size used is $0.025R_0/C_s$, where C_s/R_0 is 2.0258×10^5 sec^{-1} and $C_s = \sqrt{T_e/m_i}$ is the ion-acoustic wave speed. The plasma is represented by the marker particles that are loaded uniformly throughout the simulation domain. From the convergence test, 50 marker particles per cell are used, and the number of electron subcycles is 2. The system size in this work is set as $a = 175\rho_i$, where ρ_i is the ion gyro-radius.

The effective charge number Z_{eff} is taken as 1.0 while considering the collisions in the simulations. The on-axis effective collision frequency ν^* is 0.04 for electrons and 0.26 for ions. The turbulent transport and the zonal flow physics are the universal aspects of the drift wave instabilities [45, 88]. To study the effect of zonal flow on turbulent transport, an additional nonlinear simulation is run by artificially suppressing the zonal flow during the simulation. Figure 5.4 shows the poloidal cross-sections of the electrostatic potential at different simulation times for the two nonlinear simulations. Figure 5.4a shows the contour plot of the electrostatic potential in the linear phase of the simulation at time $t = 3.5R_0/C_s$. The linear eigenmode structure that peaks near the flux surface with $\psi \sim \psi_X$ looks like a typical ballooning mode which is localized on the outer mid-plane side where the curvature is bad in the region of steep profile gradient with the eddies elongated along the direction of the profile gradient. Figure 5.4b shows the enlarged view of the mode structure on the poloidal plane. The mode propagates in the electron diamagnetic direction, in-

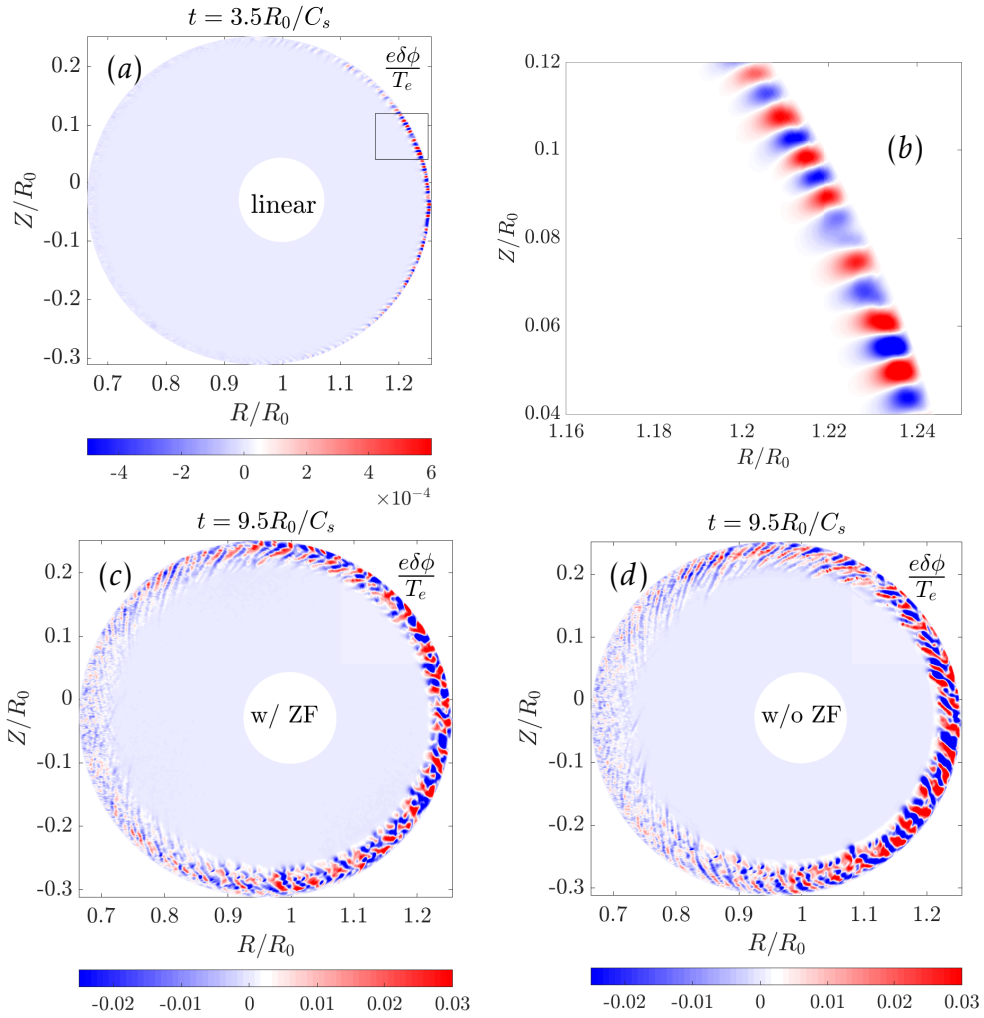

Figure 5.4 – The electrostatic perturbed potential on the poloidal plane in the linear phase at time $t = 3.5R_0/C_s$ (a), and the enlarged view of the linear eigenmode structure (b). The electrostatic potential in the nonlinear phase at time $t = 9.5R_0/C_s$ with zonal flow (c), and without zonal flow (d).

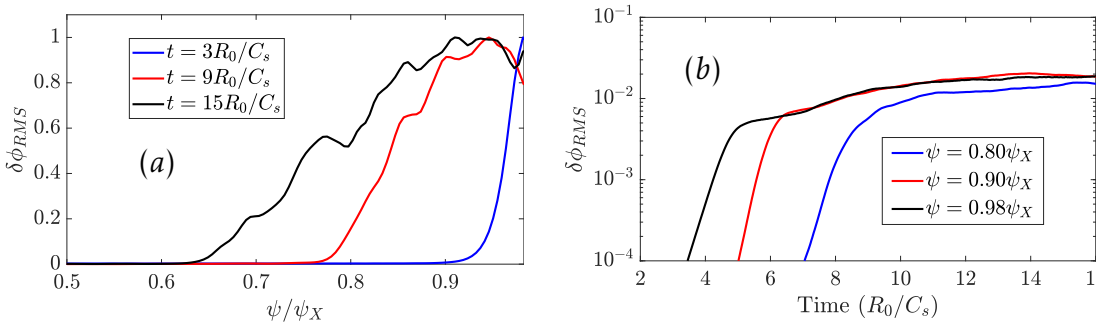

Figure 5.5 – (a) The radial variation of the root-mean-squared electrostatic perturbed potential normalized to the maximum value at three different times $3R_0/C_s$ (blue), $9R_0/C_s$ (red) and $15R_0/C_s$ (black), and (b) the time history of the root-mean-squared perturbed electrostatic potential in the region of turbulence spreading at three different flux surfaces with $0.80\psi_X$ (blue), $0.90\psi_X$ (red), and $0.98\psi_X$ (black).

dicating that the TEM turbulence is unstable, which is also consistent with the earlier gyrokinetic simulations of the DIII-D pedestal with steep profile gradients using GTC [172]. These findings are similar to the earlier investigations made for the reversed field pinch (REP) [209], tokamak [210–215] and stellarator [216, 217] plasmas in the region of steep plasma profile gradients. Figures 5.4c and 5.4d show the contour plot of the electrostatic potential in the nonlinear phase of the simulation at time $t = 9.5R_0/C_s$ with zonal flow (5.4c) and without zonal flow (5.4d). In the nonlinear phase, the coupling between various toroidal modes and the interaction with the self-generated zonal flow leads to the turbulence spreading from the edge to the core of the tokamak. It illustrates that the global effects play an important role in linking the turbulent transport from the edge to the core of the tokamak.

The radial-time variation of the root-mean-squared electrostatic potential has been shown in Fig. 5.5. Figure 5.5a shows the radial variation of root-mean-squared electrostatic potential at three different times $t = 3R_0/C_s$ (blue), $9R_0/C_s$ (red) and $15R_0/C_s$ (black). It is clear that in the nonlinear stage, turbulence structures spread far away from the location of the linear eigenmode. The turbulence spreading takes place in the radial range $\psi \in [0.68, 1.0]\psi_X$ over the simulation time. Figure 5.5b shows the time history of the root-mean-squared electrostatic potential in the region of turbulence spreading at three different flux surfaces with $\psi = 0.80\psi_X$ (blue), $0.90\psi_X$ (red), and $0.98\psi_X$ (black). Thus, in the region of turbulence spreading TEM turbulence is unstable.

The role of zonal flow in regulating the turbulence and transport is shown in Fig. 5.6. Figure 5.6a shows the time history of root-mean-squared electrostatic potential without zonal flow (blue), with zonal flow (red) and the radial electric

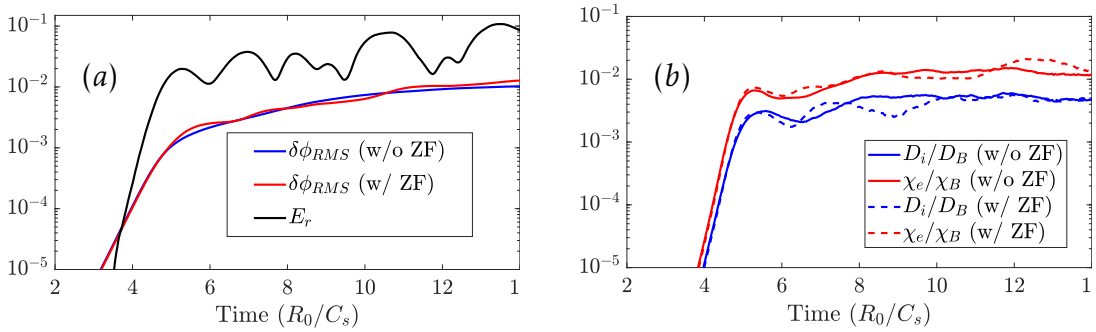

Figure 5.6 – (a) The time history of the root-mean-squared electrostatic perturbed potential without zonal flow (blue), with zonal flow (red) and the radial electric field resulting from the turbulence (black) at $\psi \sim \psi_X$. The root-mean-squared electrostatic potential is normalized by T_e/e, and the radial electric field is normalized by $\sqrt{T_e/e}$. (b) The time history of the ion diffusivity (blue) and electron heat conductivity (red) in the Bohm units, with (dashed) and without (solid) zonal flow at $\psi \sim \psi_X$.

field resulting from the turbulence (black) at the flux surface with $\psi = 0.98\psi_X$. The blue and red lines are almost overlapping with each other, which shows that the zonal flow is not playing an important role in suppressing the turbulence. Furthermore, as shown in Fig. 5.6b, the time histories of the ion diffusivity (blue) and electron heat conductivity (red) show similar saturation levels with zonal flow (dashed) and without the zonal flow (solid). So, the zonal flow does not have any effect on the transport as well. The nonlinear saturation is dominated by the inverse cascade of the higher toroidal and poloidal modes to the lower one, which is also clear from the comparison of Figs. 5.4c and 5.4d, as there is not much difference in the turbulence structure. These results are supported by the earlier findings by the local simulations, stating that the zonal flow has an important contribution to the turbulent transport driven by TEM instability only when $\eta_e = \nabla \ln T_e / \nabla \ln n_e \lesssim 1$ [164] and for the current discharge of ADITYA-U, $\eta_e \sim 4.0$ at $\psi \sim \psi_X$. Yet another global simulation study using GTC has shown that the zonal flow can play a crucial role in the case with $T_e = T_i$ [166], while in ADITYA-U the electron temperature is about three times the ion temperature. Similarly, the flux-tube (local) simulations using GENE have shown that the zonal flow has little effect on the TEM turbulence saturation for the cases with strong electron temperature gradient and $T_e = 3T_i$ [165], which is the case for ADITYA-U.

The dominant eigenmode is $n = 73$, $m = 271$ with the growth rate of $\gamma = 2.98 C_s/R_0$ and the real frequency of $\omega = 2.79 C_s/R_0$. The wave number corresponding to the dominant mode is $k_\perp \rho_i \sim 0.7$. The simulations show that the collisions reduce the linear growth rate of the dominant mode by almost 9%

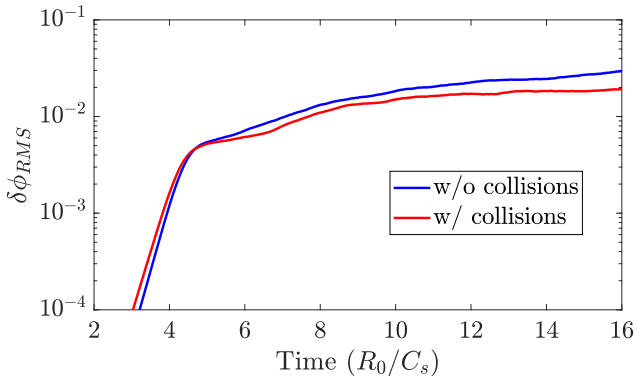

Figure 5.7 – The time history of the root-mean-squared electrostatic potential without collisions (blue) and with collisions (red) at $\psi = 0.98\psi_X$.

	with collisions	without collisions
γ	2.98	3.24
$\delta\phi_{RMS}$	0.0169	0.0229
D_i	0.25	0.67
D_e	0.32	0.64
χ_i	0.89	1.80
χ_e	1.20	1.28

Table 5.2 – The effect of collisions on the tubulence growth rate γ in units of C_s/R_0, the root-mean-squared electrostatic potential $\delta\phi_{RMS}$ in units of T_e/e and the transport coefficients D_α, χ_α ($\alpha = i,\ e$) in units of $\mathrm{m}^2/\mathrm{sec}$.

and suppress the electrostatic fluctuations by almost 36%.

The comparison of the root-mean-squared electrostatic potential without and with collisions is made in Fig. 5.7. Furthermore, the collisional effects reduce the ion heat conductivity by half, the ion diffusivity by more than half, the electron heat conductivity by $\sim 7\%$, and the electron diffusivity by half. The effect of collisions on various quantities have been shown in Table 5.2. The root-mean-squared electrostatic potential and transport coefficients are averaged over times $t \in [10, 15]R_0/C_s$. Usually, the collisions have a stabilization effect on the TEM turbulence [153], but due to the smaller collision frequency for the trapped electrons TEM remains unstable even in the presence of collisions. The TEM turbulence and transport suppression (to some extent) caused by the collisional effects are due to the de-trapping of electrons.

Figure 5.8 shows the 2D spectrum ($|\delta\phi_{mn}|$) of the electrostatic perturbed potential on the flux surface with $\psi = 0.98\psi_X$ in the linear phase at time $t = 3.5R_0/C_s$ (5.8a) and in the nonlinear phase averaged over times $t \in [10, 15]R_0/C_s$ (5.8b). Because of the ballooning feature of the microturbulence and the exten-

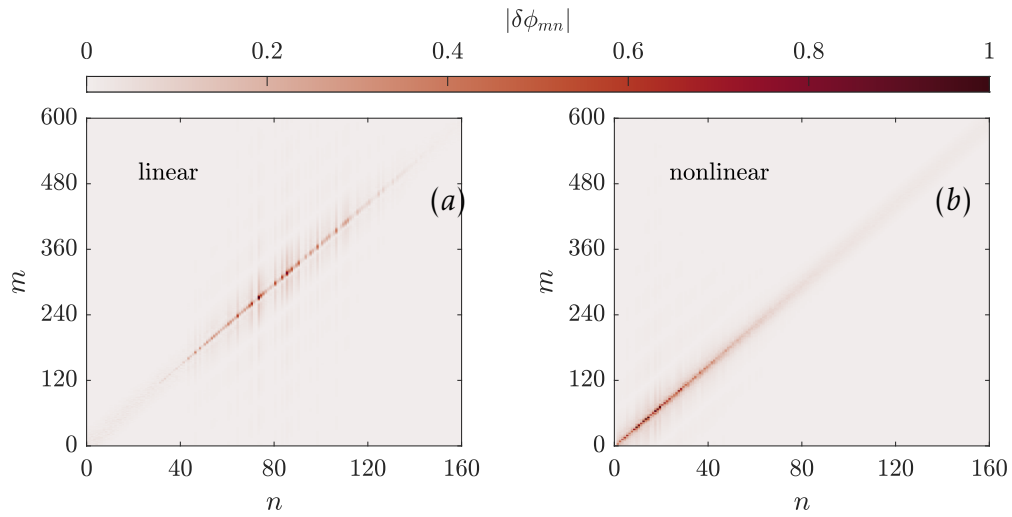

Figure 5.8 – The 2D spectrum of the electrostatic potential on the flux surface $\psi = 0.98\psi_X$ in the linear phase at time $t = 3.5R_0/C_s$ (a) and in the nonlinear phase averaged over times $t \in [10, 15]R_0/C_s$ (b).

sion of the potential in the direction parallel to the magnetic field while confining in the perpendicular direction, the spectrum peaks on the mode rational surface (along the $m = nq$ line) in the spectral domain. On the diagnosed flux surface $\psi = 0.98\psi_X$, the value of safety factor is $q = 3.71$. The spectrum in the linear phase is wide with a range $n \in [40, 125]$, $m \in [160, 460]$ with the most dominant mode at $n = 73$, $m = 271$. The nonlinear coupling of the turbulent modes leads to the inverse cascade of the linearly unstable modes from high to low poloidal and toroidal modes. The spectrum in the nonlinear phase is averaged over the times $t \in [10, 15]R_0/C_s$ that has a range $n \in [0, 50]$, $m \in [0, 190]$. The transport coefficients are calculated in GTC as

$$\chi_\alpha = \frac{1}{\langle|\nabla\psi|^2\rangle n_{0\alpha}\frac{\partial T_{0\alpha}}{\partial\psi}}\left\langle\int d^3v\delta f_\alpha\left(\frac{1}{2}m_\alpha v^2 - \frac{3}{2}T_{0\alpha}\right)\vec{v}_E\cdot\nabla\psi\right\rangle$$

and

$$D_\alpha = \frac{1}{\langle|\nabla\psi|^2\rangle\frac{\partial n_{0\alpha}}{\partial\psi}}\left\langle\int d^3v\delta f_\alpha\vec{v}_E\cdot\nabla\psi\right\rangle,$$

where the angle bracket $\langle\cdots\rangle$ represents the flux-surface average and $|\cdots|$ represents the amplitude of the vector. GTC gives the conductivity (D_α) and heat diffusivity (χ_α) normalized by the Bohm values; $D_B = \chi_B = cT_e/eB$. The time history of the ion and electron diffusivities and heat conductivity averaged over $\psi \in [0.68, 1.0]\psi_X$ is shown in Fig. 5.9a. The transport coefficients first increase

(m^2/sec)	Experiment	Simulation
D_i	0.2	0.25
χ_e	1.5	1.20

Table 5.3 – Comparison of the transport from the experiment with the simulations near LCFS.

exponentially in the linear phase and then saturate in the nonlinear phase due to mode coupling. Figure 5.9b shows the radial variation of the ion and electron diffusivities and heat conductivities averaged over time $t \in [10, 15]R_0/C_s$ at each radial grid point. The turbulence which is localized at $\psi \sim \psi_X$ where the gradient in the profile is maximum, in the nonlinear phase spreads throughout the simulation domain due to the nonlinear mode coupling. As there is not much turbulence spreading near the magnetic axis, the central region $\psi \in [0, 0.1]\psi_X$ has been excluded from the simulation domain.

Figure 5.10 shows the comparison of the spectrum of electrostatic fluctuations between experiment and simulation that spans from $\sim$ 0kHz to 50kHz, plotted on the outer mid-plane side of the flux surface with $\psi = 0.98\psi_X$. The experimentally recorded spectrum of electrostatic fluctuations shows a broadband of frequencies from $\sim$ 0 to 50 kHz (red) that matches well with the findings of the gyrokinetic simulations (blue) of ADITYA-U tokamak using GTC. The ion diffusivity near to the LCFS of tokamak predicted from the self-consistent simulations using GTC (see Fig. 5.9) is in good agreement with the value $\sim$ 0.2 m^2/sec derived from the density profile [206], which is further cross-checked with UEDGE code simulations [207]. Due to the diagnostic limitations at the present time, the realistic experimental value of the electron heat conductivity is not avaliable. The experimental value of the electron heat conductivity is estimated by assuming a diffusive transport and using an energy confinement time from power balance as $\chi_e \sim a^2/4\tau_E$, where a is the minor radius (0.25 m) and τ_E is the energy confinement time [208]. Experimentally, τ_E is obtained by the usual method of dividing the stored energy by the power input, that gives $\tau_E \sim 10$ msec [206]. This estimate of the electron heat conductivity obtained from the experiment is $\chi_e \sim 1.5$ m^2/sec, which is within 20% of the value $\chi_e \sim 1.2$ m^2/sec obtained from the simulations (see Fig. 5.9). Table 5.3 shows the comparison of the transport between the experiment and simulation near to the LCFS.

All these findings illustrate that trapped electron mode (TEM) driven microturbulence is one of the dominant channels for driving the turbulent transport in the ADITYA-U tokamak. These results may be important in setting up future

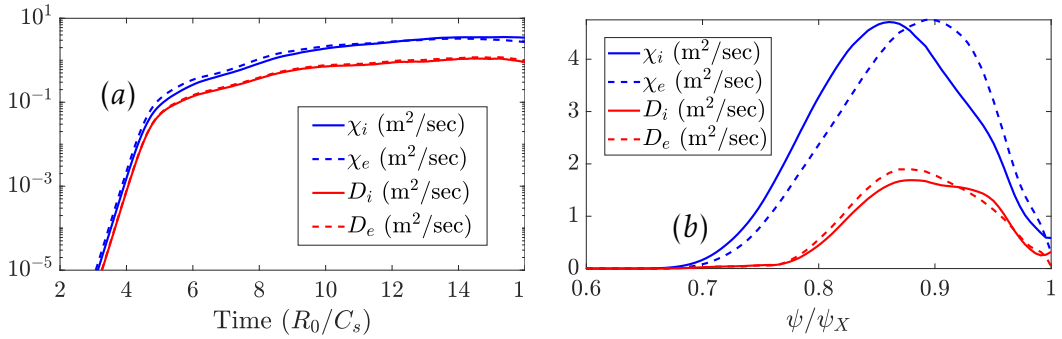

Figure 5.9 – The time history (a) and radial variation (b) of the transport coefficients for ions and electrons.

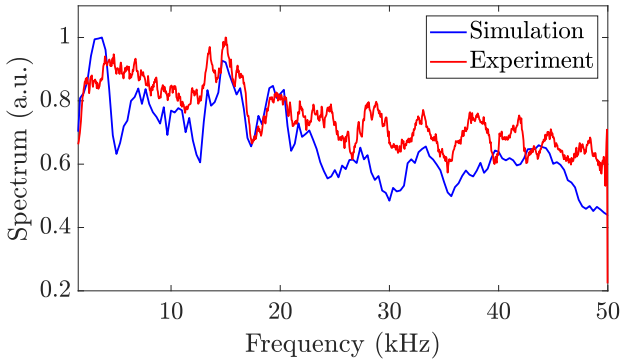

Figure 5.10 – The comparison of the spectra of the electrostatic fluctuations from simulation (blue) and experiment (red) near the LCFS.

ADITYA-U experiments.

5.4 Conclusions and discussion

To summarize, in this chapter, global gyrokinetic simulations of the electrostatic microturbulence in the ADITYA-U tokamak for discharge # 33536 are carried out in the presence of collisions using gyrokinetic toroidal code (GTC). The linear eigenmode structure is dominated by a trapped electron driven instability, propagating in the electron diamagnetic direction with a real frequency of $\sim 2.79 C_s/R_0$, and the growth rate of $\sim 2.98 C_s/R_0$, that lies on the low wave number side with $k_\perp \rho_i \sim 0.7$. The simulations with and without collisions show that the collisional effects suppress the turbulence and transport to a certain extent. The nonlinear simulations of the microturbulence predict the ion diffusivity value, which agrees well with the experimentally measured value of ~ 0.2 m^2/sec. The electron heat conductivity estimated from the experimentally measured energy confinement time is also within 20% of the sim-

ulated value ~ 1.2 m^2/sec. Further, the spectrum of electrostatic fluctuations shows broadband of frequencies from ~ 0 to 50 kHz which also agrees with the spectrum obtained from the experiment. The nonlinear simulations show that the zonal flow is not playing an important role in the turbulence saturation, while the nonlinear saturation is dominated by the inverse cascade of the high poloidal and toroidal modes to the lower one. Furthermore, the global effects play an important role in linking the turbulence and transport from the edge to the core of the tokamak. Thus, the electrostatic microturbulence driven by the trapped electrons in the presence of collisions acts as one of the dominant channels for driving the anomalous turbulent transport in the ADITYA-U tokamak. The current work is the first step to understanding the turbulence and transport in ADITYA-U. From the experimental perspective, the insights gained from this electrostatic microturbulence study may be useful in setting up future ADITYA-U experiments. In the future, we plan to study the impurity transport by the electrostatic microturbulence, effects of equilibrium radial electric fields, and electromagnetic effects in ADITYA-U.

Chapter 6

Microturbulent transport in ADITYA-U tokamak with impurities

6.1 Introduction

Microturbulence is witnessed as one of the major causes of the degradation of plasma confinement [45]. Therefore, reducing microturbulent transport is the main objective for the viability of nuclear fusion from burning plasmas. Over the years, several studies, with the injection of light impurities to increase plasma confinement, have gained considerable attention [78, 86, 176, 177]. For example, neon seeding experiments in DIII-D have shown an improvement in plasma confinement due to the suppression of core turbulence and transport [66].

In this direction, impurity seeding experiments have been performed in ADITYA-U tokamak, which is a medium-sized, air-core tokamak, that has recently been upgraded from the ADITYA tokamak [70–73] to incorporate a new set of divertor coils for shaped plasma operations with a new vacuum vessel along with a new toroidal belt limiter. The experiments performed in ADITYA-U are relevant to the primary long-term goals of future fusion devices such as ITER [71–73], including experiments on generation, transport, and control of runaway electrons [72, 73], plasma disruption [72, 73], transient transport phenomena such as cold-pulse propagation [73, 74] and plasma detachment [73]. The recent GTC gyrokinetic analysis has shown electrostatic microturbulence as one of the dominant transport channels in ADITYA-U [135]. Argon puffing experiments in ADITYA-U have shown reduced turbulence fluctuations and transport [218]. However, the underlying mechanism for the observed transport is not apparent and demands dedicated gyrokinetic simulations to gain insight into the matter.

In the present work, global gyrokinetic simulations of microturbulent trans-

port are carried out in the presence of argon impurities. The effect of the radial electric field, which is determined from the toroidal rotation [203], is also studied on the turbulence and transport. Based on current analysis, the dominant instability is found to share the characteristics of both ITG and TEM driven turbulences depending upon its propagation direction and response to the self-generated zonal flow. The radial electric field reduces the turbulence fluctuations due to the increased $\vec{E} \times \vec{B}$ shear. The comparison of the transport before and after argon puffing in the nonlinear phase of the simulations shows a reduction in the transport, which is majorly due to the change in the linear drive of the turbulence due to the change in the plasma profile. However, it demands further study to understand the underlying process for the change in profile after argon puffing in ADITYA-U.

This chapter is organized as follows: in Sec. 6.2, the argon puffing experiment is described in ADITYA-U. In Sec. 6.3, the electrostatic microturbulence simulations are presented using GTC, and in Sec. 6.4 conclusions are made.

6.2 Argon puffing experiment in ADITYA-U

This section briefly describes the argon puffing experiment in ADITYA-U tokamak. Experimental discharge # 34528 is analyzed using GTC. The plasma profile and turbulence fluctuations are measured using various diagnoses, and then the argon gas is puffed/injected from the edge of the tokamak. Argon gas diffuses inside the plasma and gets ionized, and following this, the state of the plasma is again recorded. The typical time difference between these two sets of measurements is about 20 ms. Experiments show increased plasma confinement due to reduced fluctuations after argon puffing. Figure 6.1 shows the plasma profile before (dashed lines) and after (solid lines) argon puffing. The plasma temperature and total density increase by about 10% due to improved plasma confinement after argon puffing. Figure 6.2 shows the normalized plasma profile gradient, safety factor profile (6.2a), and the radial electric field (6.2b) estimated from the toroidal rotation [203]. In the figure, $1/L_X = \frac{\partial \ln X}{\partial r}$ is the inverse gradient scale length, where r is the local minor radius.

6.3 Microturbulence simulations

In this section, the gyrokinetic simulations of electrostatic microturbulence are carried out using GTC in the presence of argon impurities with the plasma profiles described in Sec. 6.2. The simulation parameters are fixed by performing the convergence studies. The time step size is $0.025 R_0/C_s$, the number of par-

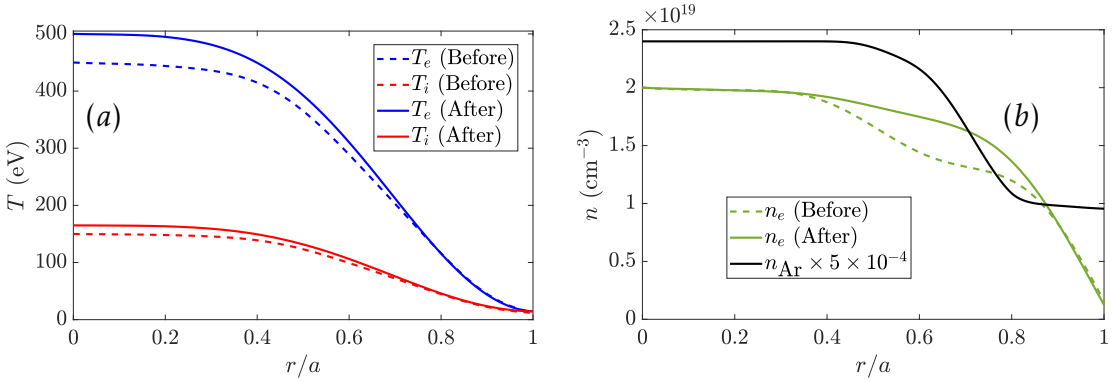

Figure 6.1 – The radial profile for the plasma temperature (a) and density (b) before (dashed lines) and after (solid lines) argon puffing for the discharge # 34528.

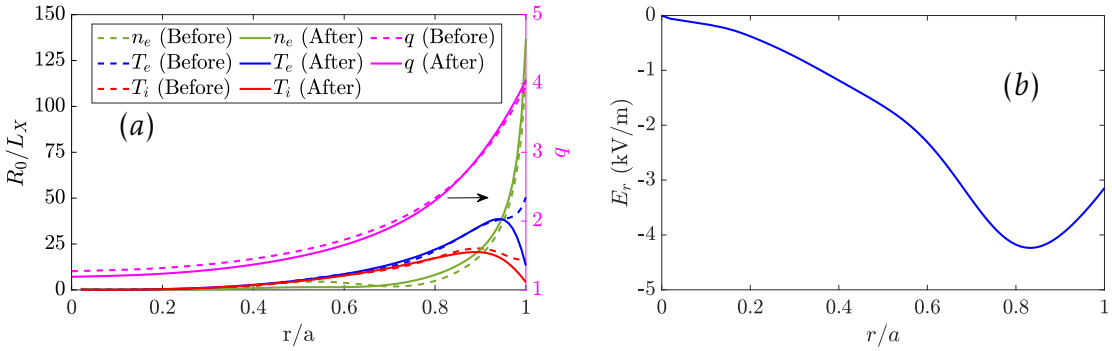

Figure 6.2 – The radial variation of (a) the gradient in plasma profile and safety factor before (dashed lines) and after (solid lines) argon puffing, and (b) the radial electric field.

ticles per cell is 50, and the number of electron subcycles is 2. The simulation grid uses 200 radial grid points, 3000 poloidal grid points, and 32 grid points in the parallel direction. The simulation domain is set as $r \in [0.27, 1.0]a$ that translates to $\psi \in [0.1, 1.0]\psi_X$, where ψ is the poloidal flux and ψ_X is the value at the last closed flux surface (LCFS). The effective charge of the plasma is $Z_{\mathrm{eff}} = 2.5$, which does not change after argon puffing. Before argon puffing, the plasma is described as the thermal ions and electrons, whereas after argon puffing, the plasma is composed of thermal ions, argon impurity ions, and electrons.

Firstly, the gyrokinetic simulations have been performed for instance, before the argon puffing (using the profiles shown with the dashed lines in Fig. 6.1). Figure 6.3 shows the poloidal electrostatic potential in the linear (6.3a) and nonlinear (6.3b) phases of the nonlinear simulation. The electrostatic potential is normalized with T_e/e. The linear eigenmode structure is quite broad and spreads throughout the simulation domain in the nonlinear phase due to the nonlinear mode coupling and interaction with the self-generated zonal flow. Based on the linear eigenmode's propagation direction, the turbulence is char-

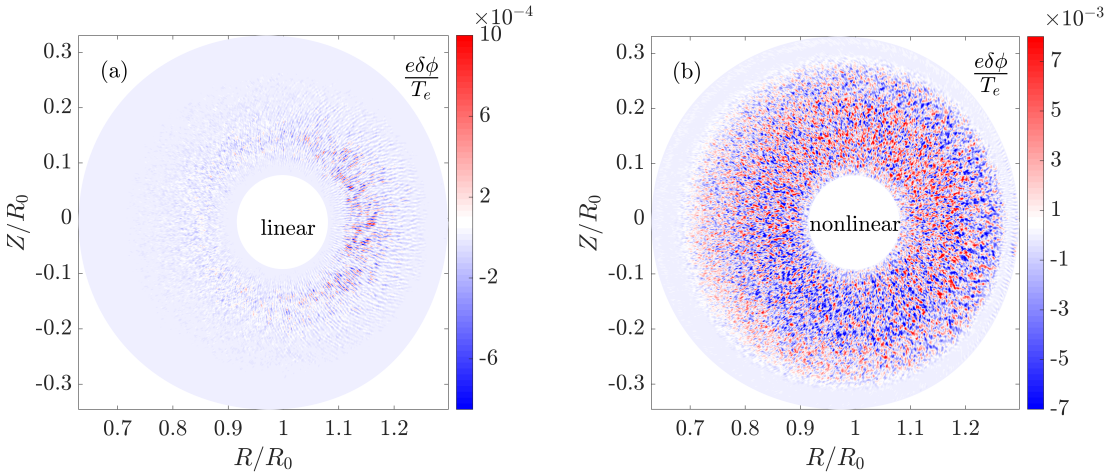

Figure 6.3 – The electrostatic potential on the poloidal plane in the linear (a) and nonlinear (b) phase before argon gas puffing.

acterized as TEM. The dominant eigenmode is $n = 100$, $m = 202$ at the radial location $r \sim 0.7a$ with a frequency of ~ 6 kHz. However, the nonlinear simulations show a broad frequency spectrum, as seen in the recent study [135]. For the case after argon puffing, the electrostatic potential on the poloidal plane (not shown here) shows a similar structure, though the amplitude of the fluctuations is different.

To study the role of zonal flow on turbulence, an additional simulation is carried out by artificially suppressing the zonal flow. Figure 6.4 shows the radial variation of the root-mean-squared electrostatic potential with and without zonal flow. The root-mean-squared electrostatic potential is normalized with T_e/e. The radial quantities presented in this chapter are time-averaged. Zonal flow substantially reduces the turbulence in the whole radial range. Earlier investigations by different studies have shown that the zonal flow plays a vital role in regulating ITG turbulence. In contrast, its effect is weak on TEM driven turbulence [152, 160–166]. Based on these observations, it is found that for the current scenario, the turbulence shares the features of both the ITG and TEM driven turbulence. In support of our results, the earlier investigations by different researchers have also shown the co-existence of ITG and TEM driven turbulences depending upon the local plasma parameters [219–221]. However, a more detailed systematic stability analysis is required to conclude the nature of turbulence for the analyzed discharge of ADITYA-U.

For the effect of the radial electric field on microturbulence, simulations are performed by including the radial electric field as shown in Fig. 6.2b. Figure 6.5 shows the radial profile of the root-mean-squared electrostatic potential with and without the radial electric field for the case before argon puffing. The

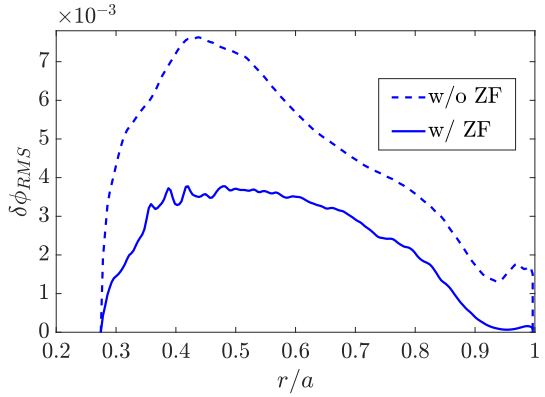

Figure 6.4 – The radial profile of the root-mean-squared electrostatic potential with and without zonal flow.

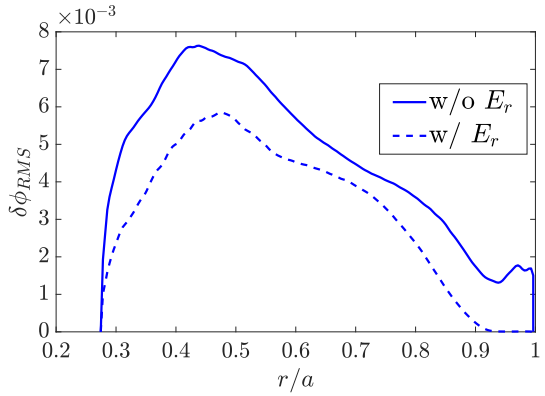

Figure 6.5 – The radial profile of the root-mean-squared electrostatic potential with and without the radial electric field.

turbulent potential is reduced substantially due to the increased $\vec{E} \times \vec{B}$ shear that decorrelates the turbulent eddies. In addition, the convection due to E_r stabilizes TEM by dislocating the trapped electrons and turbulent fluctuations to the region of favorable curvature.

Figure 6.6 shows the comparison of the radial variation of the root-mean-squared electrostatic potential before (dashed line) and after (solid line) argon puffing. The turbulent potential is substantially reduced in the radial range $r < 0.6a$ due to the different plasma profiles and, thus, different instability drives. The ion heat conductivity and ion diffusivity are compared in Fig. 6.7 before and after argon puffing. The ion heat conductivity shows a noticeable reduction inside the core, whereas the diffusivities increase around $r \sim 0.5a$.

Finally, the role of argon as the impurities in the gyrokinetic simulations is investigated by carrying out the gyrokinetic simulations using the plasma profile recorded after argon puffing while eliminating the argon impurities from the simulations. Figure 6.8 shows the radial variation of the root-mean-squared

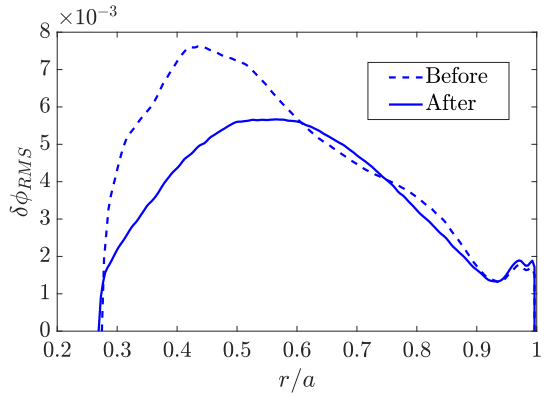

Figure 6.6 – The radial profile of the root-mean-squared electrostatic potential before and after argon puffing.

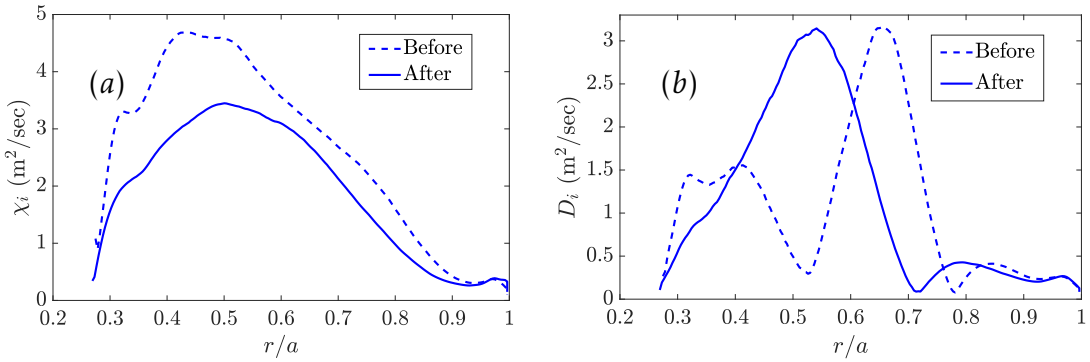

Figure 6.7 – The radial variation of the ion heat conductivity (a) and ion diffusivity (b) before (dashed line) and after (solid line) argon puffing.

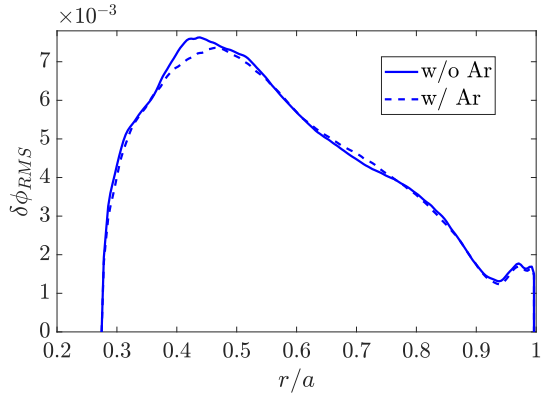

Figure 6.8 – The radial profile of the root-mean-squared electrostatic potential with the profiles after argon puffing, with and without argon impurities.

electrostatic potential for the case after argon puffing, with and without argon impurity ions. As shown in Fig. 6.1b, the concentration of argon impurity ions is relatively small compared to the thermal ions. Therefore, including argon impurities in the gyrokinetic simulations does not affect the turbulent dynam-

ics. Furthermore, the observed change in the turbulence and transport after argon puffing is solely due to the change in plasma profile leading to different turbulence drives for both cases. However, it would be essential to investigate the underlying process for the change in plasma profile after argon puffing, which could be a future study.

6.4 Conclusions and discussion

In this chapter, global gyrokinetic simulations of the electrostatic microturbulent transport in the ADITYA-U tokamak are performed in the presence of argon impurity and radial electric field determined from the toroidal rotation. The dominant instability shares the characteristics of ITG turbulence and TEM depending upon its direction of propagation and response to the zonal flow. However, we need a more systematic study to identify the dominant transport channel. The radial electric field suppresses turbulence and transport by changing the $\vec{E} \times \vec{B}$ shear. However, due to their low concentration, including argon ions in the gyrokinetic simulations does not affect the transport. A comparison of the simulations before and after argon puffing shows that the primary mechanism responsible for the reduction in transport is due to the change in plasma profile after argon puffing, which changes the linear instability drive due to the change in the profile gradient. Further simulation studies would be necessary to decipher the underlying mechanism for the change in plasma profile after argon puffing.

Chapter 7

Gyrokinetic toroidal code using X-point

7.1 Introduction

One of the important challenges in achieving a viable operating regime for ITER and future fusion reactors is associated with the nonlinear turbulent dynamics of the plasma in the scrape-off layer (SOL) [127]. The plasma characteristics in SOL can significantly affect the overall confinement properties of the device and also regulate the heat load to the tokamak wall. It can also influence the level of fusion ash, impurity dynamics, sheath physics, and plasma shaping effects. Furthermore, the SOL dynamics can degrade the current drive performance of radio frequency (RF) waves through their impact on the density threshold conditions for the onset of parametric decay instabilities [222]. An in-depth understanding of the mechanisms determining the width of the SOL layer remains an outstanding open problem.

A study of the SOL plasma dynamics is challenging due to the multiple spatial and temporal scales associated with different energy sources (instabilities) in that region. Fluid simulation transport codes such as UEDGE [223] and SOLPS [224] are generally used to simulate the SOL dynamics. These fluid codes use a set of fluid transport equations that are based on the Braginskii equations [225]. However, the results show several discrepancies between experimental findings and fluid simulations, especially in the characteristics of the radial electric field, parallel ion flow, impurity radiation, etc. [226–228]. It is believed that kinetic effects could be a significant contributor in the SOL to processes like ion orbit losses [229], X-point losses [230], nonlocal turbulent transport [231], plasma sheath dynamics [232], parametric decay instabilities [222, 233], etc. To correctly model many of these effects, one requires a kinetic approach that covers the closed and open field line regions across the

separatrix and includes the realistic SOL physics and tokamak geometry, such as DIII-D, as shown in Fig. 7.1.

Due to the difficulty in the accessibility of diagnostics in the SOL region, such global kinetic simulations can help develop valuable insights for predicting the plasma dynamics in that region for present and future reactors such as ITER and DEMO (DEMOnstration Power Station). A laudable effort in this direction has been the development of the massively parallel kinetic simulation code XGC-1 [234], which takes an approach based on first-principles and has emerged as an efficient method for describing the complex physics of turbulent transport. Another widely used and successful tool, the gyrokinetic toroidal code (GTC), has continuously developed for the past two decades and has been applied to studying plasma transport in the core region [93].

GTC is a well-benchmarked, first-principles code that has been extensively applied to the investigation of neoclassical transport [235], microturbulence [120], mesoscale Alfvén eigenmodes excited by energetic particles [236], macroscopic MHD modes [237] (kink and tearing modes), and radio frequency (RF) waves [238] in the core region. However, the assumptions used in studying turbulence in the core region may not be valid in the SOL region. GTC uses conventional magnetic flux coordinates, in which the equations of motion encounter a mathematical singularity of the metric on the magnetic separatrix surface. It is due to the vanishing of the poloidal magnetic field near the X-point and singular behaviors of the safety factor and Jacobian of Boozer coordinates near the separatrix. Recently, the GTC was extended to separately study instabilities in the SOL and core regions of a field reversed configuration (FRC) using Boozer coordinates. However, the code still did not have the capability to couple these two regions [239]. The difficulty lay in the discontinuity of the poloidal angle across the separatrix in the Boozer coordinates. This limitation restricted the codes usage to electrostatic simulations in either the core or the SOL region, with no cross-separatrix coupling.

In this chapter, a significant enhancement of the GTC, called the gyrokinetic toroidal code using the X-point (GTC-X), is presented through the development of a new global nonlinear particle simulation model that couples the tokamak core and SOL regions. The formulation and testing of the modules developed in GTC-X to simulate the low frequency drift wave instabilities are discussed. These capabilities are tested by benchmarking the zonal flow in the core of a tokamak.

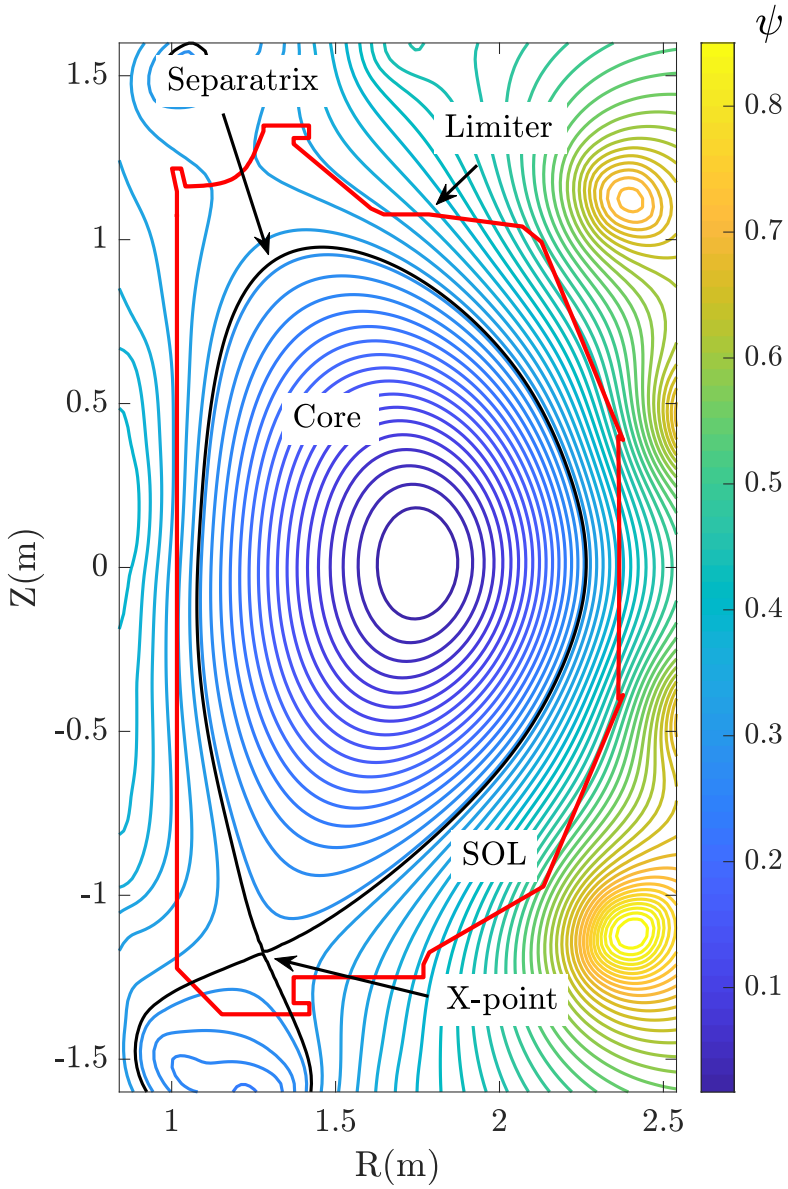

Figure 7.1 – Representation of the magnetic flux surfaces on the poloidal plane of DIII-D tokamak discharge # 158103. The colormap shows the poloidal flux ψ in web/rad. The separatrix surface is shown in black, and the limiter is shown with the red boundary.

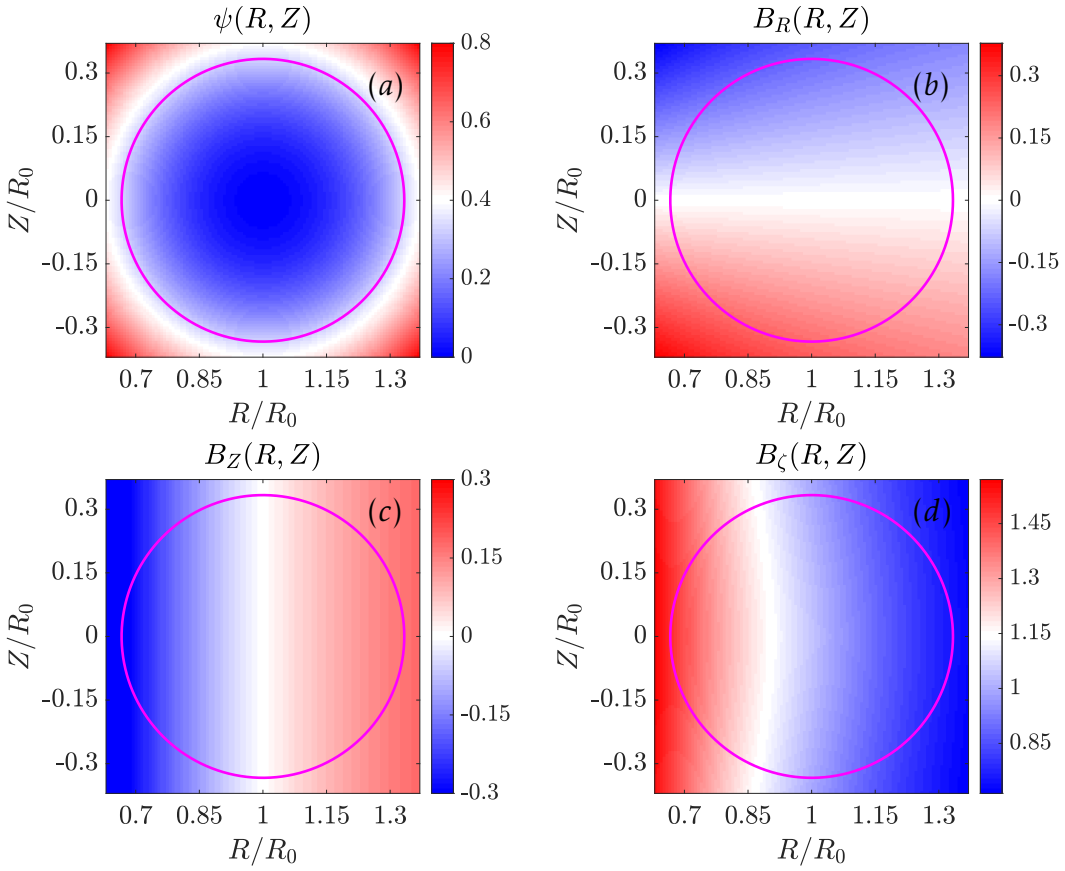

Figure 7.2 – Circular Tokamak Equilibrium being used for code benchmarking and testing. The poloidal magnetic flux (a) is normalized with the value at the wall or limiter ψ_w represented by the magenta curve, and the magnetic field components (b, c, d) are presented in Tesla.

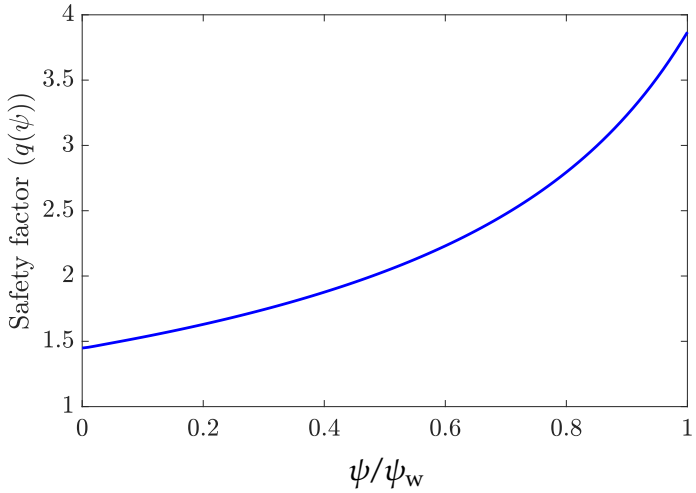

Figure 7.3 – The safety factor profile for the circular tokamak equilibrium being used for code benchmarking and testing. The poloidal flux is normalized with the value at the wall.

7.2 Equilibrium used for code benchmarking and verification

Before dealing with the more general magnetic geometry, a circular tokamak equilibrium generated using EFIT [143] is adopted to benchmark the code and test various modules developed in the following sections. The various parameters of the tokamak are comparable to that of the realistic tokamak, such as ADITYA-U [73] described in Chapters 5 and 6. Figure 7.2 shows the poloidal magnetic flux $\psi(R,Z)$ for the circular tokamak in the upper left panel. The magenta curve represents the limiter that coincides with the last closed flux surface (LCFS). For axisymmetric devices such as tokamaks, the magnetic field is represented as

$$\vec{B} = \nabla\psi(R,Z) \times \nabla\zeta + \frac{F(\psi)}{R}\hat{\zeta}, \tag{7.1}$$

where $F(\psi)$ is the poloidal current function. The individual magnetic field components are calculated as follows:

$$B_R = -\frac{1}{R}\frac{\partial\psi}{\partial Z}, \quad B_Z = \frac{1}{R}\frac{\partial\psi}{\partial R}, \quad B_\zeta = \frac{F(\psi)}{R}. \tag{7.2}$$

The magnetic field components are shown in Fig. 7.2 on the poloidal plane in the cylindrical coordinates. Figure 7.3 shows the safety factor profile as a function of the poloidal flux ψ normalized with the value at the wall or limiter ψ_w for the tokamak equilibrium shown in Fig. 7.2. Given the equilibrium magnetic configuration, the spline interpolation maps the coarse equilibrium mesh to the fine computational mesh to achieve desirable numerical accuracy and computational efficiency.

7.3 Particle dynamics

To simulate the turbulence arising from the low frequency drift waves such as ITG/TEM, equations of motion of the guiding center of the particle are solved in cylindrical coordinates. The gyrokinetic Vlasov equation representing the phase space distribution of the particles in 5D is given by

$$\left(\frac{\partial}{\partial t} + \dot{\vec{X}}\cdot\nabla + \dot{v}_\parallel\frac{\partial}{\partial v_\parallel}\right) f_\alpha(\vec{X}, \mu, v_\parallel, t) = 0, \tag{7.3}$$

where $\vec{X}$, $v_\parallel$ are the position and parallel velocity of the guiding center position of the particle, respectively, f_α is the guiding center distribution function, and α labels the plasma species.

$$\dot{\vec{X}} = \frac{\vec{B}^*}{B_\parallel^*} v_\parallel + \vec{v}_E + \vec{v}_c + \vec{v}_g, \tag{7.4}$$

$$\vec{v}_E = \frac{c\hat{b} \times \nabla\phi}{B_\parallel^*}, \tag{7.5}$$

$$\vec{v}_c = \frac{B}{B_\parallel^*} \frac{v_\parallel^2}{\Omega_\alpha} \nabla \times \hat{b}, \tag{7.6}$$

$$\vec{v}_g = \frac{\mu_\alpha}{m_\alpha \Omega_\alpha} \frac{\vec{B} \times \nabla B}{B_\parallel^*}, \tag{7.7}$$

where $\vec{B}^* = B_\parallel^* \left(\hat{b} + \frac{v_\parallel}{\Omega_{c\alpha}} \nabla \times \hat{b} \right)$ is the magnetic field at the guiding center position of the particle, $\hat{b}$ is the unit vector along the magnetic field, $B_\parallel^* = \hat{b} \cdot \vec{B}^*$, $\mu_\alpha = m_\alpha v_\perp^2 / 2B$ is the magnetic moment of the particle, $\Omega_{c\alpha}$ is the cyclotron frequency of the plasma particle α, Z_α, m_α, and μ_α are the charge, mass, and magnetic moment of the species α, ϕ is the electrostatic potential, $B_\parallel^*$ is the magnetic field amplitude at the guiding center parallel to the magnetic field, $\vec{v}_E$, $\vec{v}_c$, and $\vec{v}_g$ are the $\vec{E} \times \vec{B}$ drift, curvature drift, and drift due to gradient in magnetic field, respectively.
The individual components of the guiding center are given by

$$\dot{R} = v_\parallel b_R - \frac{v_\parallel^2}{\Omega_{c\alpha}} \frac{\partial b_\zeta}{\partial Z} + \frac{\mu_\alpha}{m_\alpha \Omega_{c\alpha}} b_\zeta \frac{\partial B}{\partial Z} + \frac{c}{B} \left(b_\zeta \frac{\partial \phi}{\partial Z} - \frac{b_Z}{R} \frac{\partial \phi}{\partial \zeta} \right), \tag{7.8}$$

$$\dot{Z} = v_\parallel b_Z + \frac{v_\parallel^2}{R\Omega_{c\alpha}} \frac{\partial}{\partial R}(R b_\zeta) - \frac{\mu_\alpha}{m_\alpha \Omega_{c\alpha}} b_\zeta \frac{\partial B}{\partial R} + \frac{c}{B} \left(\frac{b_R}{R} \frac{\partial \phi}{\partial \zeta} - b_\zeta \frac{\partial \phi}{\partial R} \right), \tag{7.9}$$

$$\begin{aligned} \dot{\zeta} = \frac{1}{R} \Bigg[v_\parallel b_\zeta + \frac{v_\parallel^2}{\Omega_{c\alpha}} \left(\frac{\partial b_R}{\partial Z} - \frac{\partial b_Z}{\partial R} \right) + \frac{\mu_\alpha}{m_\alpha \Omega_{c\alpha}} \left(b_Z \frac{\partial B}{\partial R} - b_R \frac{\partial B}{\partial Z} \right) \\ + \frac{c}{B} \left(b_Z \frac{\partial \phi}{\partial R} - b_R \frac{\partial \phi}{\partial Z} \right) \Bigg]. \end{aligned} \tag{7.10}$$

The equation for the parallel velocity is given by

$$\dot{v_\parallel} = -\frac{1}{m_\alpha} \frac{\vec{B}^*}{B_\parallel^*} \cdot (Z_\alpha \nabla\phi + \mu_\alpha \nabla B), \tag{7.11}$$

$$\dot{v_\parallel} = -\frac{Z_\alpha}{m_\alpha} \hat{b}.\nabla\phi - \frac{\mu_\alpha}{m_\alpha} \hat{b} \cdot \nabla B - \frac{v_\parallel}{m_\alpha \Omega_{c\alpha}} \left[(\nabla \times \hat{b}).(Z_\alpha \nabla\phi + \mu_\alpha \nabla B) \right],$$

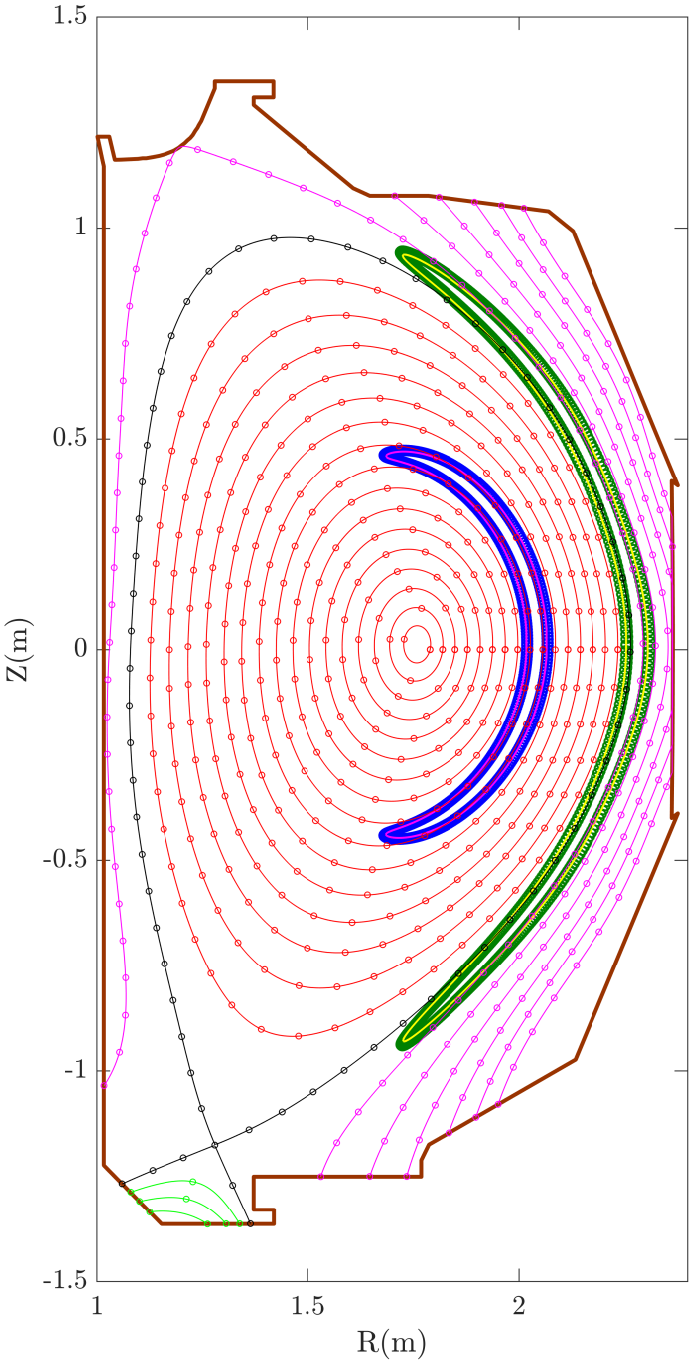

Figure 7.4 – GTC-X computations of fully kinetic (blue and green) and guiding center (magenta and yellow) orbits of the trapped particles in the core and cross-separatrix on the poloidal plane for DIII-D discharge # 158103 at 3050 ms. Field-aligned mesh is represented by grids drawn on the flux surfaces.

where the individual terms are simplified as follows:

$$-\frac{Z_\alpha}{m_\alpha}\hat{b}\cdot\nabla\phi = -\frac{Z_\alpha}{m_\alpha}\left(b_R\frac{\partial\phi}{\partial R}+b_Z\frac{\partial\phi}{\partial Z}+\frac{b_\zeta}{R}\frac{\partial\phi}{\partial\zeta}\right),$$

$$-\frac{\mu_\alpha}{m_\alpha}\hat{b}\cdot\nabla B = -\frac{\mu_\alpha}{m_\alpha}\left(b_R\frac{\partial B}{\partial R}+b_Z\frac{\partial B}{\partial Z}+\frac{b_\zeta}{R}\frac{\partial B}{\partial\zeta}\right),$$

$$\begin{aligned}-\frac{v_\parallel}{m_\alpha\Omega_{c\alpha}}&\left[(\nabla\times\hat{b})\cdot(Z_\alpha\nabla\phi+\mu_\alpha\nabla B)\right]\\ &=-\frac{v_\parallel}{m_\alpha\Omega_{c\alpha}}\left[-\frac{\partial b_\zeta}{\partial Z}\left(Z_\alpha\frac{\partial\phi}{\partial R}+\mu_\alpha\frac{\partial B}{\partial R}\right)+\frac{1}{R}\frac{\partial}{\partial R}(Rb_\zeta)\left(Z_\alpha\frac{\partial\phi}{\partial Z}+\mu_\alpha\frac{\partial B}{\partial Z}\right)\right.\\ &\left.+\frac{1}{R}\left(\frac{\partial b_R}{\partial Z}-\frac{\partial b_Z}{\partial R}\right)\left(Z_\alpha\frac{\partial\phi}{\partial\zeta}+\mu_\alpha\frac{\partial B}{\partial\zeta}\right)\right].\end{aligned}$$

GTC-X also incorporates the fully kinetic particle integrator to study the high frequency phenomenon, such as the physics of radio frequency waves. These equations of motion are solved using the Boris push method [92]. For the verification of the particle orbits in the core and especially in the cross-separatrix region, DIII-D discharge # 158103 at 3050 ms is used. Figure 7.4 shows the fully kinetic and trapped particle orbits calculated using GTC-X for DIII-D discharge # 158103. Fully kinetic orbits are presented in blue and green, and guiding center orbits are drawn in magenta and yellow. The fully kinetic and guiding center integrators correctly capture the trapped particle orbits and agree well with each other. The details can be found in Ref. [240]. For the calculations of fluctuating quantities such as density and field, GTC-X uses field-aligned mesh that is represented by grids drawn on the flux surfaces shown in Fig. 7.4.

7.4 Field solver

As the plasma particles are drifted maximally along the field lines, the parallel and perpendicular dynamics can be separated out, and hence the 3D Poisson equation can be approximated as a 2D partial differential equation that can be solved over the poloidal plane. To solve the 2D Poisson equation for the electrostatic simulations, a new finite element based field solver is developed and incorporated in GTC-X. The finite element solver has the advantage over the finite difference solver as the latter one loses its capability on the magnetic axis and X-point. For finite element solver, finite element mesh is required, which is generated using *Triangle* code [241], which uses constrained Delaunay triangulation (CDT) to triangulate the grid points. This code precisely takes

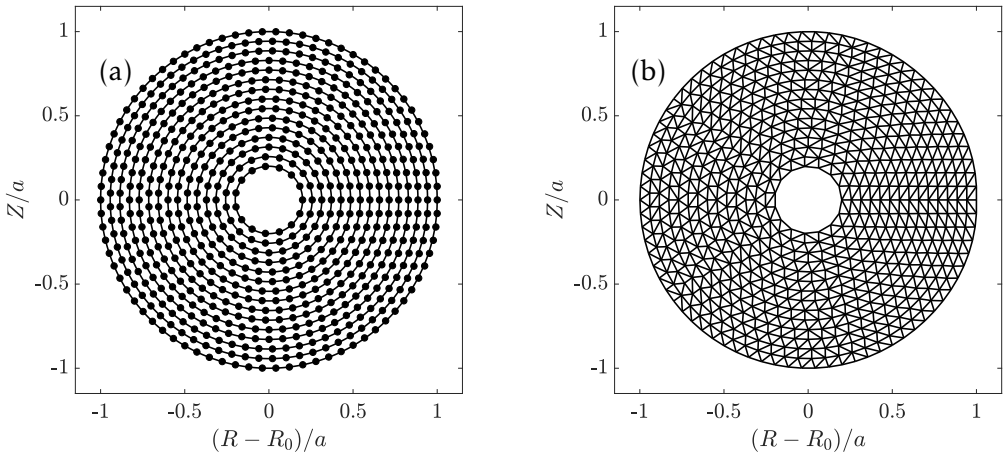

Figure 7.5 – Circular tokamak equilibrium representing first 15 flux surfaces with inner radius $a_0 = 0.2$ and outer radius $a_1 = 1.0$, a and R_0 are the minor and major radii, respectively. Field-aligned grids consisting of 694 grid points (a) and the triangular mesh constructed from the grids using *Triangle* code consisting of 1295 elements (b).

care of the constraints of the simulation procedure. Figure 7.5 shows the field-aligned grids (a) and triangular mesh (b) generated from *Triangle* code.

The formulation of the field solver based on the finite element method is adopted from Ref. [242]. Firstly, the given domain is discretized into a collection of preselected elements, and then the Poisson equation is written into its weak form. The local matrix is constructed for each of the elements, and then the global matrix is constructed for the whole problem. The boundary conditions are imposed over the boundaries of the simulation domain. Then the resulting matrix equation is solved using state-of-the-art toolkits PETSc [149] or HYPRE [150].

Figure 7.6 shows the structure of the global matrix constructed using the above procedure. For the verification of the finite element solver, a test function of the form shown in Fig. 7.7 is applied to the solver, and the resulting solution is compared with the analytical solution. This comparison is shown in Fig. 7.8. Figure 7.9 shows the comparison between analytical and numerical solutions on the outer midplane side. The numerical solution from GTC-X agrees well with the analytical solution.

7.5 Low noise δf method

To reduce the particle noise from the Monte Carlo sampling of marker particles, a low noise δf simulation method [97] is implemented in GTC-X, where the total particle distribution is decomposed into an equilibrium part, and a

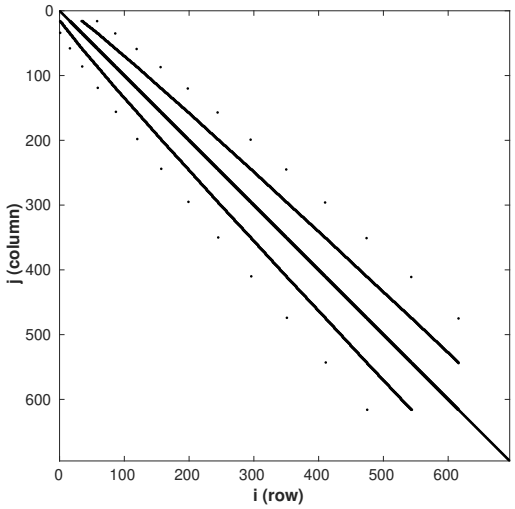

Figure 7.6 – The shape of the sparse matrix (694 x 694) for the field-aligned grids constructed on the circular equilibrium resulting from the 2D Poisson solver based on the finite element method. The Dirichlet boundary condition is included on the inner and outer flux surfaces.

fluctuating part and only the later part is represented using the marker particle distribution resulting into the reduction in simulation noise. An additional dynamical variable, particle weight, is introduced and evolved along with the equations of motion. The following equations are solved in GTC-X for the δf simulations of low frequency drift wave turbulence:

$$\frac{d\mathrm{w}_\alpha}{dt} = (1-\mathrm{w}_\alpha)\Big(\mathrm{w}_{\mathrm{drive}} + \mathrm{w}_{\mathrm{para}} + \mathrm{w}_{\mathrm{drift}}\Big), \tag{7.12}$$

where the individual terms are described as follows:

$$\mathrm{w}_{\mathrm{drive}} = -\vec{v}_E \cdot \frac{\nabla f_{\alpha 0}}{f_{\alpha 0}}, \tag{7.13}$$

$$\mathrm{w}_{\mathrm{para}} = -\frac{Z_\alpha}{T_{\alpha 0}} v_\parallel \hat{b} \cdot \nabla\phi, \tag{7.14}$$

$$\mathrm{w}_{\mathrm{drfit}} = -\frac{Z_\alpha}{T_{\alpha 0}} \left(\vec{v}_c + \vec{v}_g\right) \cdot \nabla\phi, \tag{7.15}$$

where $f_{\alpha 0}$ is the particle distribution, and $T_{\alpha 0}$ is the temperature profile of the plasma species. $f_{\alpha 0}$ is the Maxwellian, solution to the Vlasov equation to the lowest order, given by

$$f_{\alpha 0} = n_{\alpha 0}\sqrt{\frac{m_\alpha}{2\pi T_{\alpha 0}}}\exp\left[-\frac{m_\alpha v_\parallel^2 + 2\mu_\alpha B}{2T_{\alpha 0}}\right].$$

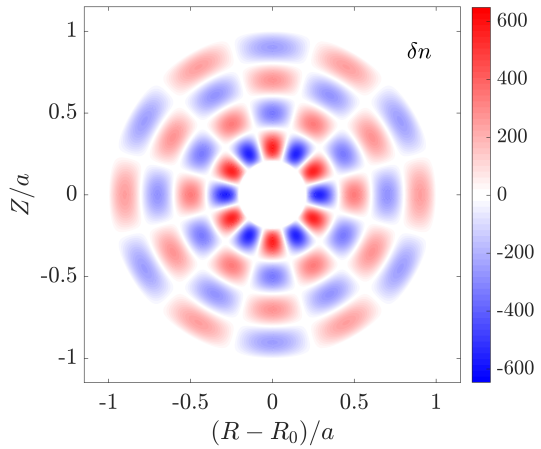

Figure 7.7 – 2D contour plot of the source term $\delta n(R,Z)$ on the poloidal plane adapted for the verification of 2D Poisson solver based on the finite element method.

Each of the weight terms can be expressed as:

$$w_{\text{para}} = -\frac{Z_\alpha}{T_{\alpha 0}}\frac{v_\parallel}{B}\left[B_R\frac{\partial\phi}{\partial R} + B_Z\frac{\partial\phi}{\partial Z} + \frac{B_\zeta}{R}\frac{\partial\phi}{\partial\zeta}\right], \tag{7.16}$$

$$\begin{aligned} w_{\text{drift}} = -\frac{Z_\alpha}{m_\alpha T_{\alpha 0}\Omega_{c\alpha}}\Bigg[&\left(\mu_\alpha b_\zeta\frac{\partial B}{\partial Z} - m_\alpha v_\parallel^2\frac{\partial b_\zeta}{\partial Z}\right)\frac{\partial\phi}{\partial R} + \left(\frac{m_\alpha v_\parallel^2}{R}\frac{\partial(Rb_\zeta)}{\partial R} - \mu_\alpha b_\zeta\frac{\partial B}{\partial R}\right)\\ &\frac{\partial\phi}{\partial Z} + \frac{1}{R}\left(m_\alpha v_\parallel^2\left(\frac{\partial b_R}{\partial Z} - \frac{\partial b_Z}{\partial R}\right) + \mu_\alpha\left(b_Z\frac{\partial B}{\partial R} - b_R\frac{\partial B}{\partial Z}\right)\right)\frac{\partial\phi}{\partial\zeta}\Bigg], \end{aligned} \tag{7.17}$$

and,

$$\begin{aligned} w_{\text{drive}} = &\left[\frac{\partial\phi}{\partial\zeta}\left(b_R^2 + b_Z^2\right) - Rb_\zeta\left(\frac{\partial\phi}{\partial Z}b_Z + \frac{\partial\phi}{\partial R}b_R\right)\right]\\ &\left(\frac{1}{n_{\alpha 0}}\frac{\partial n_{\alpha 0}}{\partial\psi} + \left(\frac{\varepsilon}{T_{\alpha 0}} - \frac{3}{2}\right)\frac{1}{T_{\alpha 0}}\frac{\partial T_{\alpha 0}}{\partial\psi}\right), \end{aligned} \tag{7.18}$$

where

$$\varepsilon = \frac{1}{2}m_\alpha v_\parallel^2 + \mu_\alpha B$$

is the energy of the particle.

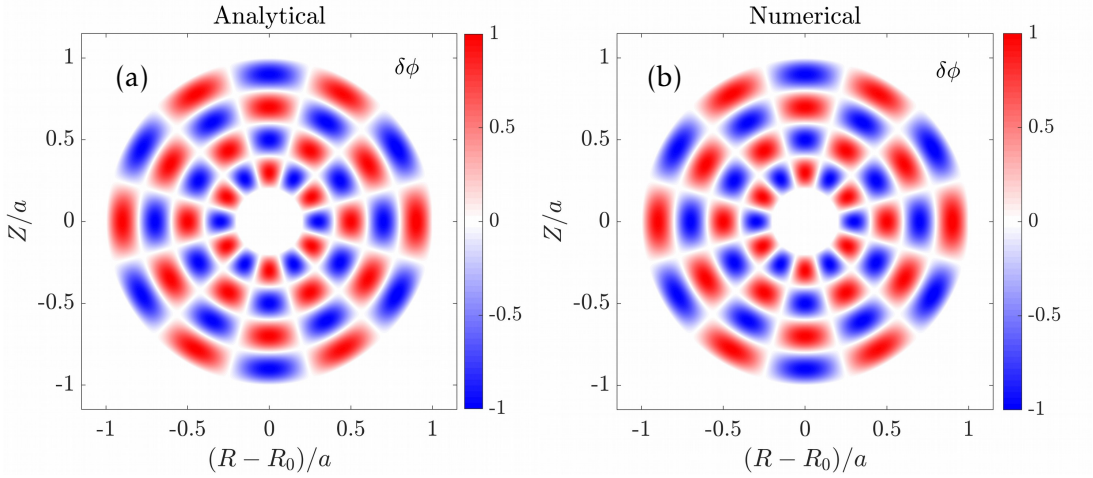

Figure 7.8 – Verification of the 2D Poisson solver based on finite element method by comparing the analytical (a) and the numerical (b) solutions on the poloidal plane.

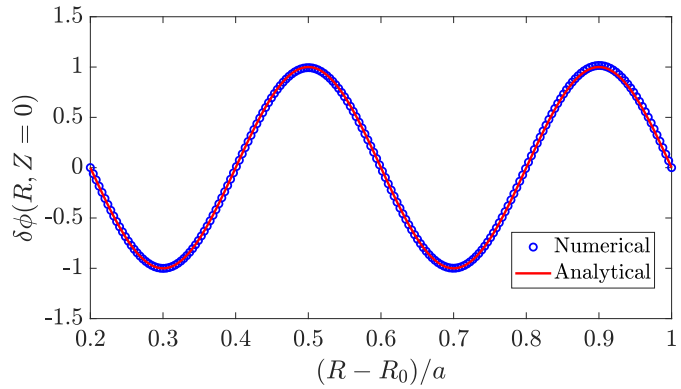

Figure 7.9 – Verification of the 2D Poisson solver based on the finite element method by comparing the analytical and the numerical solutions on the outer mid-plane.

7.6 Particle-grid interpolation

To interpolate the fluctuating quantities from the particle position to the computational grids and vice versa, a new particle-grid interpolation is incorporated into GTC-X. In contrast to GTC, which uses Boozer coordinates (straight field line coordinates) and the poloidal grids are rotated in going from one poloidal plane to the other for the calculation of the fluctuation quantities along the field line; in GTC-X, instead of rotating the grid points, the interpolation itself is done along the magnetic field lines as shown in Fig. 7.10 (Note: θ is not the flux coordinate angle used in traditional GTC, instead, is the geometrical angle calculated as $\tan\theta = Z/(R-R_0)$). As in cylindrical coordinates, the mag-

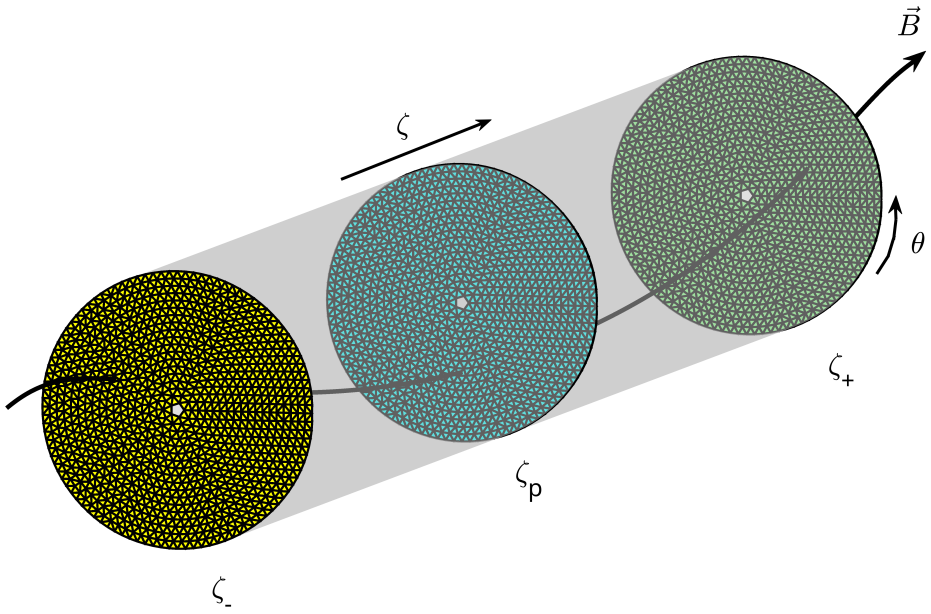

Figure 7.10 – Illustration of particle-grid interpolation in 3D.

netic field lines are not straight and can have the form shown in Fig. 7.11; the linear interpolation scheme may not be enough. So, for the interpolation along the field line, the field line passing through the particle position (at ζ_p plane) is first drawn using the following equations:

$$\frac{dR}{d\zeta} = R\frac{B_R}{B_\zeta},$$
$$\frac{dZ}{d\zeta} = R\frac{B_Z}{B_\zeta},$$

and then its intersection is found with the lower (ζ_-) and upper (ζ_+) poloidal planes. The corresponding weights are calculated on each of the poloidal planes. Once the particle is located on the lower and upper poloidal planes, the particle is then located on the flux surfaces, and the particle weights are calculated onto the two flux surfaces. Then the particle is located along the poloidal direction, and the corresponding particle weights are calculated on the poloidal grids.

Figure 7.12 shows the projection of particle-grid interpolation (Fig. 7.10) on the 2D poloidal plane. The field-aligned interpolation reflects in the change in poloidal angle θ in going from the particle position (middle point on the yellow curve) to the interpolated particle position on the lower and upper poloidal plane, respectively (lower and upper points on the yellow curve). Furthermore,

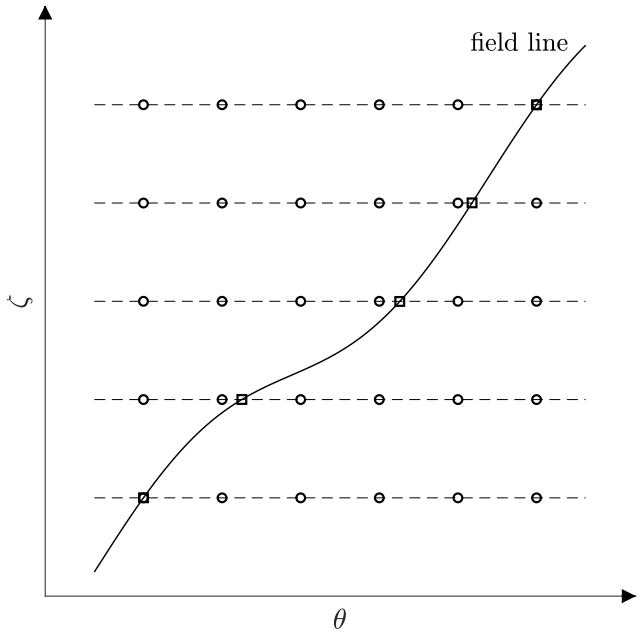

Figure 7.11 – Illustration of particle-grid interpolation on the flux surface.

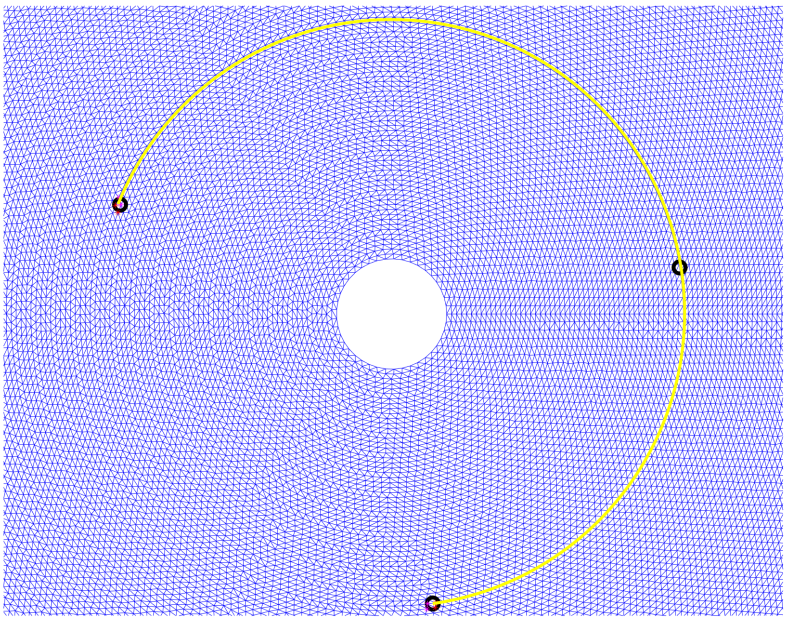

Figure 7.12 – Projection of particle-grid interpolation on the poloidal plane.

since the particle-grid interpolation is a performance bottleneck in PIC simulations, hybrid parallelization (MPI/OpenMP) is exploited in GTC-X by using

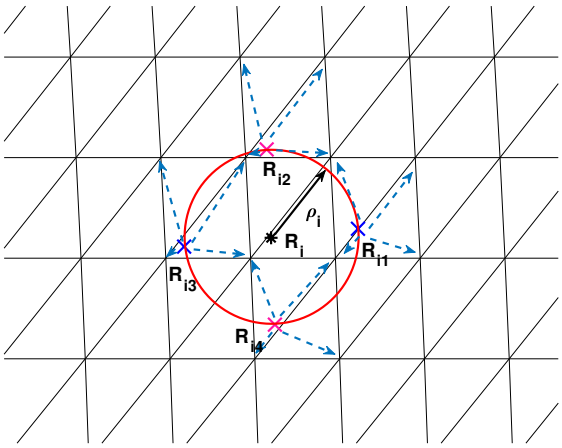

Figure 7.13 – Schematic of four-point gyro-averaging on the poloidal plane.

the toroidal and particle domain decompositions to speedup the computations, similar to GTC.

7.7 Gyro-averaging

The fast cyclotron motion is averaged out while simulating the low frequency drift wave instabilities using the gyrokinetic model, considering only the guiding center dynamics. This transformation from particle position to the guiding center position of the particle involves a Fourier transform kind of relationship between the fluctuating quantities. It needs to be taken care of numerically by considering the average over the charge ring called gyro-orbit or gyro-ring. This procedure is called gyro-averaging. A finite number of points are used to represent this charge ring. As the ratio of the poloidal magnetic field to the toroidal magnetic field is very small, the angle between the gyro-plane and the poloidal plane is very small, so the gyro-averaging is performed over the poloidal plane itself. Figure 7.13 shows the schematic of gyro-averaging using a four-point approximation of gyro-orbit. Two points (blue and magenta) are constructed along the field line, and the remaining two (red and green) are constructed perpendicular to the field line. GTC-X computations of four-point gyro-averaging and particle weights onto the poloidal plane are shown in Fig. 7.14. A particle (represented by a solid black circle) is loaded randomly in the 3D torus, and the points on the gyro-ring and their weights on the poloidal and toroidal grids are calculated as shown in the figure.

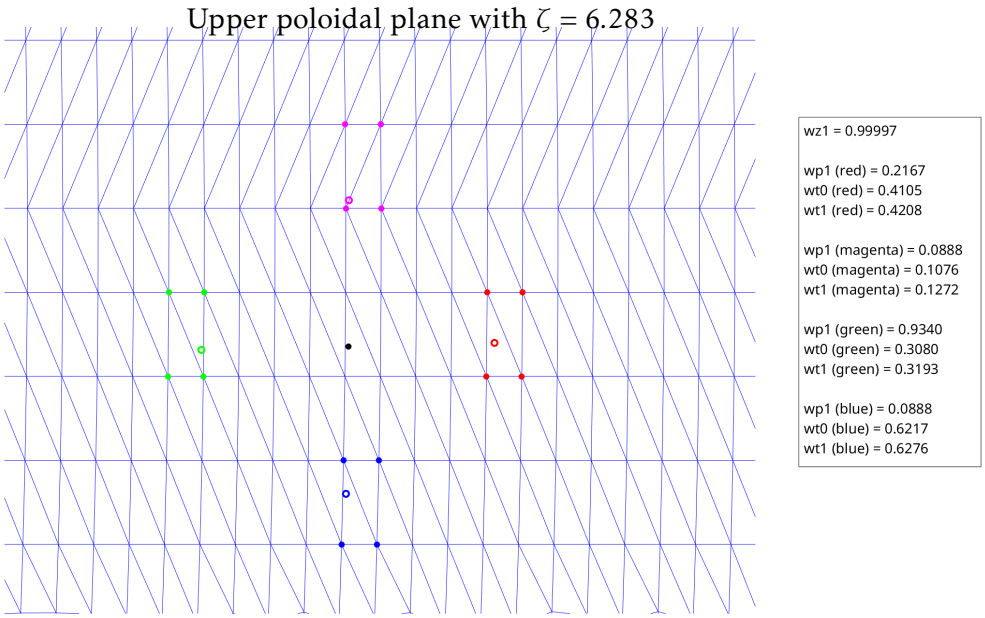

Figure 7.14 – Four-point gyro-averaging and calculation of weights on the nearest grid points on the poloidal plane. Here, wij represents the particle weights where i = p, t, z represents the indices corresponding to the ψ, θ, and ζ directions; and j = 0 or 1 represents the lower and upper poloidal plane, respectively.

7.8 Code benchmark

In this section, the above capabilities are tested by verifying the zonal flow in the core region of tokamak. Zonal potential and field are computed by solving the following equation in GTC-X using traditional integration:

$$\frac{\partial\langle\phi\rangle}{\partial\psi} = \frac{T_i}{n_i Z_i^2 e^2}\frac{\partial\langle\rho_c\rangle}{\partial\psi} - \frac{1}{g^{\psi\psi}J_0(\psi)}\int \mathrm{d}\psi \frac{T_i}{n_i Z_i^2 e^2}\left\langle\frac{1}{\rho_i^2}\right\rangle\langle\rho_c\rangle J_0(\psi), \tag{7.19}$$

where $\langle\rho_c\rangle = e(Z_i\langle\bar{n}_i\rangle - \langle n_e\rangle)$ is the flux surface averaged total charge density, $\bar{n}_i$ is the ion guiding center density, $J_0(\psi)$ is the Jacobian calculated at each flux surface, and $g^{\psi\psi}$ is the contravariant geometric tensor [131]. Zonal flow is excited by an external source, such as an antenna, that leads to sinusoidal potential perturbations in the plasma. The equations of motion of the plasma particles and electrostatic fields are calculated self-consistently using the PIC algorithm. To bring the out-of-boundary particles back to the simulation domain, energy conserving particle boundary condition is implemented in the pusher that involves: $\psi_i \to 2\psi_{0,1} - \psi_i$, $\theta_i \to 2\pi - \theta_i$, $\zeta_i \to \zeta_{i-1}$, $v_{\|}^i \to -v_{\|}^{i-1}$; where ψ_0 and ψ_1 correspond to the innermost and outermost flux surfaces describing the simulation boundaries. When the external source is switched off, the elec-

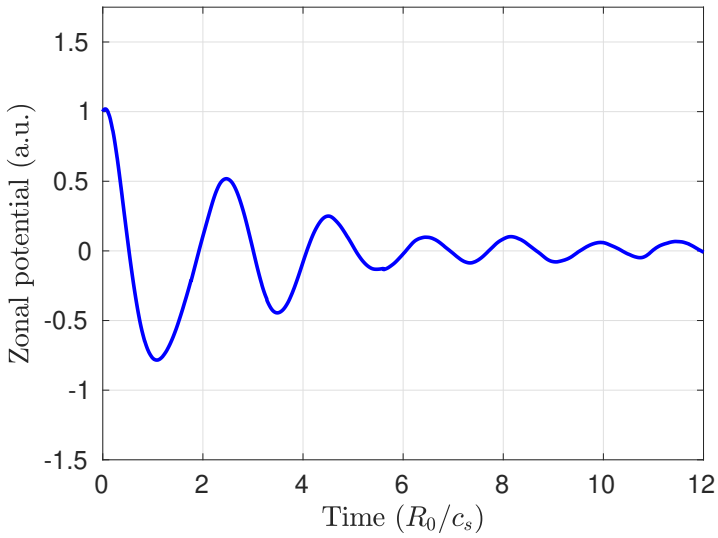

Figure 7.15 – Time history of the zonal potential on a given flux surface computed using GTC-X.

trostatic potential at any given flux surface is recorded. Figure 7.15 shows the time history of the zonal potential at any given flux surface.

7.9 Conclusions and discussion

In this chapter, a significant enhancement of GTC called the gyrokinetic toroidal code using the X-point (GTC-X) is presented by developing a new global nonlinear particle simulation model that couples the tokamak core and scrape-off layer (SOL) regions. A guiding center pusher has been implemented to simulate the low frequency drift wave instabilities such as ITG. In contrast to the finite difference scheme, which loses its capabilities at the magnetic axis and X-point, a finite-element-based field solver is incorporated in GTC-X for the whole-volume gyrokinetic simulations of fusion plasmas. A new particle-grid interpolation is implemented that uses interpolation along the magnetic field lines to calculate the fluctuating quantities on the simulation grid points. The formulation and modules implemented in GTC-X to study the low frequency drift wave instabilities are briefly described. In its present form, GTC-X is benchmarked by performing the self-consistent simulations of zonal flow using the low noise δf method in the core of a tokamak. In the future, GTC-X will be verified by benchmarking the ITG turbulence in the core of a tokamak.

Chapter 8

Conclusions and future work

8.1 Conclusions

The performance of fusion reactors is limited by the microturbulence that acts as one of the dominant channels for losing the heat and particle fluxes from the device's core. In the attempt to gain an understanding of the transport due to the electrostatic microturbulence in the core of the fusion devices, self-consistent global gyrokinetic simulation studies of the electrostatic microturbulence, mainly the ion temperature gradient (ITG) and trapped electron mode (TEM) driven turbulence, are performed in the core of LHD (Large Helical Device) stellarator and ADITYA-U tokamak using the state-of-the-art gyrokinetic toroidal code (GTC).

Firstly, in the LHD stellarator, the micro-instabilities are excited by using the numerically-generated monotonic smooth plasma profiles, and the role of zonal flow is studied in regulating the microturbulent transport. The linear eigenmode structure for ITG and TEM driven turbulence share similar characteristics. ITG turbulence simulations show that the kinetic electrons increase the growth rate and transport compared to the simulations with adiabatic electrons. Zonal flow plays a vital role in regulating the ITG turbulent transport. In contrast, its effect is weak on the transport driven by the TEM, which is rather dominated by the inverse cascade of higher toroidal and poloidal mode numbers to the lower ones. In this direction, a validation study is carried out by analyzing a realistic experimental discharge of LHD with boron impurities. Simulations show the co-existence of ITG and TEM turbulence, with their linear eigenmode frequencies matching well with the experimental findings. Nonlinear simulations show the broad poloidal wave number spectrum consistent with the experiments. The effective heat conductivities before and during boron injection are in the same ballpark estimates obtained from the experiments. However, the discrepancies in the simulated transport compared with

the experiments have been attributed to the experimental uncertainties in measurements and simplifications made in the gyrokinetic simulation model.

Secondly, in ADITYA-U tokamak, microturbulence simulations have been carried out using realistic geometry and experimental plasma profile with GTC. The dominant instability is TEM, depending upon the linear eigenmode structure and its propagation in the electron diamagnetic direction. Collisional effects reduce turbulence and transport to some extent. However, the zonal flow is not playing a vital role in the nonlinear saturation of the turbulence. The transport coefficients are found to be in the same ballpark estimates obtained from the experiments. In addition, the spectrum of electrostatic fluctuations shows a broadband similar to the one found in experiments. Following this, the effect of argon impurities and radial electric field determined from the toroidal rotation have been studied by carrying out the GTC self-consistent of electrostatic microturbulence. The radial electric field and its shear decrease the transport due to the increase in $\vec{E} \times \vec{B}$ shear. The comparison of the simulations before and after argon puffing shows that the reduction in the transport is due to the change in plasma profile after argon puffing that leads to a change in linear turbulence drive due to the change in profile gradient. However, a detailed study is essential to understand the underlying process that leads to the profile change after argon puffing.

Finally, a novel framework has been described in the cylindrical coordinates, representing the considerable enhancement of the capabilities of GTC by developing the gyrokinetic toroidal code using X-point (GTC-X). This framework has the potential for the whole-volume gyrokinetic simulations of fusion plasmas by coupling the plasma core to the scrape-off layer (SOL) without encountering the singularities in the safety factor and Jacobian at X-point in Boozer coordinates based formulations such as GTC.

To summarize, this thesis has talked about the global gyrokinetic simulations of electrostatic microturbulence in LHD stellarator and ADITYA-U tokamak using GTC. The presented studies based on GTC simulations have not only shed light on the understanding and controlling microturbulent transport but have also affirmed that the gyrokinetics represents an accurate description of the microturbulence in the fusion plasmas based on the validation studies presented in this thesis.

8.2 Future work

In this section, relevant to the progress towards the understanding and control of the turbulent transport in fusion plasmas, possible research directions are

discussed as follows:

8.2.1 Electromagnetic simulations of turbulent transport in the LHD stellarator

In the analysis of the boron powder injection experiment presented in Chapter 4 using GTC simulations in the electrostatic limit, the discrepancy between the simulations and experimental results has been attributed by pointing out the measurement uncertainties in the experiment and some of the critical physics that have not been included in the gyrokinetic simulations, which are present in the experiments. Most importantly, the magnetic field fluctuations must be incorporated into the simulations to represent a realistic scenario. In principle, the electromagnetic effects can significantly affect turbulence and transport due to the finite β effects. It has been shown by several studies that in the finite β limit, the ITG turbulence growth rate [159] and nonlinear transport [196] are significantly reduced. In the future, GTC simulations could be extended to the electromagnetic simulations of microturbulence in stellarators.

8.2.2 Electromagnetic simulations of turbulent transport in the ADITYA-U tokamak

In Chapters 5 and 6, to begin with, the electrostatic simulations of microturbulent transport have been presented in ADITYA-U using GTC. However, the electromagnetic effects could play an essential role in the microturbulent transport. In particular, the electromagnetic effects show a considerable reduction in growth rate and nonlinear transport of ITG turbulence, depending upon the values of β [159, 194, 196]. Even for sufficiently higher values of β, the ITG turbulence shows a transition to kinetic ballooning mode (KBM) [195]. It could be a future study to explore such possibilities.

8.2.3 Further analysis of argon puffing experiment in ADITYA-U tokamak

The discussion in Chapter 6 was closed with the conclusion that the detailed study is essential for identifying the process underlying the change of plasma profile after argon puffing and, hence, the reduction in turbulent transport. For this, a set of gyrokinetic simulations needs to be carried out by choosing the outwardly peaked argon density profiles and assigning a charge state to the argon ions depending on the width of the impurity density profile. Such scenarios represent the instances earlier than when the complete plasma profile

modification occurs. It could also be possible to evolve the density profile for the main plasma species for a given outwardly peaked impurity density profile to reproduce the experimentally recorded plasma profile after argon puffing. It would confirm that the argon puffing leads to the change in plasma profile primarily due to the collective dynamics of impurity ions and microturbulence. Also, it would be interesting to look at the role of different impurities, for example, neon, carbon, etc., on microturbulent transport.

8.2.4 Microturbulence simulations using GTC-X

GTC-X is aimed at whole-volume fusion plasma simulations by coupling the plasma core with the SOL. So far, GTC-X has been benchmarked by verifying the zonal flow in the core of a tokamak [240], as discussed in Chapter 7. However, in field reversed configuration (FRC) that lacks the toroidal magnetic field, GTC-X has been utilized to simulate the global ITG turbulence [243] and demonstrated the cross-separatrix coupling of turbulent transport [244]. In a similar direction, GTC-X will simulate the ITG turbulence in the tokamak core and SOL. It will be further extended to simulate the microturbulence due to electrons such as TEM using a fluid-kinetic hybrid model [119]. GTC-X, in its current form, is an electrostatic code. It would be essential to carry out whole-volume electromagnetic simulations of microturbulence.

8.2.5 Alfvén eigenmodes and energetic particle transport in stellarators

Several experiments with auxiliary heating in fusion plasmas have shown the presence of Alfvén eigenmodes (AEs) [245], which are driven unstable due to wave-particle resonance of shear Alfvén waves and energetic particles (EPs) during the slowing-down process and enhance the radial transport of α-particles produced during fusion. Due to this, the EPs are lost before delivering their entire energy to the core plasma. Apart from this, the loss of α-particles also leads to localized heating of plasma-facing components, thus degrading the device's performance. Therefore, the good confinement of α-particles is desirable in both tokamaks and stellarators for efficient heating of the fusion fuel and better performance. These EP-driven instabilities are extensively studied in neutral beam injection (NBI) experiments of LHD [246]. However, the underlying physical mechanisms behind the transport due to AEs are yet to be understood adequately. For this purpose, global gyrokinetic simulation studies are required to shed light on the matter. For example, one of the fascinating future directions to explore will be the interaction of microturbulence and AEs [67].

Fundings and resources

The work presented in this thesis is supported by the National Supercomputing Mission (NSM), Science and Engineering Research Board (SERB), Infosys grant, and Board of Research in Nuclear Sciences (BRNS) project by the Department of Atomic Energy, India. This work is partially supported by the US Department of Energy, Office of Science, Office of Advanced Scientific Computing Research, and Office of Fusion Energy Sciences, Scientific Discovery through Advanced Computing (SciDAC). The results presented in this thesis are simulated on the ANTYA cluster at the Institute of Plasma Research, Gujarat, India, SahasraT and Param Pravega supercomputers at the Indian Institute of Science, Bangalore, India, and the US National Energy Research Scientific Computing Center (NERSC).

Bibliography

[1] H. A. Bethe, "Energy production in stars," Physical Review, vol. 55, pp. 103–103, Jan 1939. 1

[2] J. Wesson and D. J. Campbell, Tokamaks. Oxford University Press, 2018. 1, 4, 6, 8, 9, 73

[3] R. Betti and O. A. Hurricane, "Inertial-confinement fusion with lasers," Nature Physics, vol. 12, no. 5, pp. 435–448, 2016. 1

[4] J. Ongena, R. Koch, R. Wolf, and H. Zohm, "Magnetic-confinement fusion," Nature Physics, vol. 12, no. 5, pp. 398 – 410, 2016. 1, 9, 73

[5] D. Clery, "Explosion marks laser fusion breakthrough," Science, vol. 378, pp. 1154–1155, 2022. 2

[6] E. Gibney, "Nuclear-fusion reactor smashes energy record," Nature, vol. 602, p. 371, 2022. 2

[7] "Department of energy announces $50 million for a milestone-based fusion development program." https://www.energy.gov/science/, 2022. 2

[8] "STEP: Spherical Tokamak Energy Production." https://step.ukaea.uk/, 2023. 2

[9] "Fusion energy breakthrough at the world-leading Joint European Torus facility." https://research-and-innovation.ec.europa.eu/news/all-research-and-innovation-news_en, 2022. 2

[10] "Amid renewed interest in nuclear fusion, Japan's research reaches critical stage." https://www.japantimes.co.jp/news/2023/02/19/national/science-health/japan-nuclear-fusion-research-critical-stage/, 2023. 3

[11] "ITER: International Thermonuclear Experimental Reactor.." http://www.iter.org/, 2021. 3, 4, 10, 73

[12] Y. Xu, "A general comparison between tokamak and stellarator plasmas," Matter and Radiation at Extremes, vol. 1, pp. 192–200, 07 2016. 3

[13] M. Kikuchi, "A review of fusion and tokamak research towards steady-state operation: A JAEA Contribution," Energies, vol. 3, no. 11, pp. 1741 – 1789, 2010. 4

[14] D. A. Spong, "3D toroidal physics: Testing the boundaries of symmetry breaking," Physics of Plasmas, vol. 22, no. 5, p. 055602, 2015. 5, 13, 37, 55

[15] L. Spitzer, "The stellarator concept," The Physics of Fluids, vol. 1, no. 4, pp. 253–264, 1958. 5, 13, 37, 55

[16] A. H. Boozer, "Non-axisymmetric magnetic fields and toroidal plasma confinement," Nuclear Fusion, vol. 55, p. 025001, Jan 2015. 5, 13, 37, 55

[17] J. Nührenberg and R. Zille, "Quasi-helically symmetric toroidal stellarators," Physics Letters A, vol. 129, no. 2, pp. 113–117, 1988. 5, 37, 55

[18] A. H. Boozer, "Quasi-helical symmetry in stellarators," Plasma Physics and Controlled Fusion, vol. 37, no. 11A, pp. A103–A117, 1995. 5, 37, 55

[19] C. D. Beidler, H. M. Smith, A. Alonso, J. Baldzuhn, M. N. A. Beurskens, M. Borchardt, S. A. Bozhenkov, K. J. Brunner, H. Damm, M. Drevlak, O. P. Ford, G. Fuchert, J. Geiger, P. Helander, U. Hergenhahn, M. Hirsch, U. Höfel, Y. O. Kazakov, R. Kleiber, M. Krychowiak, S. Kwak, A. Langenberg, H. P. Laqua, U. Neuner, N. A. Pablant, E. Pasch, A. Pavone, T. S. Pedersen, K. Rahbarnia, J. Schilling, E. R. Scott, T. Stange, J. Svensson, H. Thomsen, Y. Turkin, F. Warmer, R. C. Wolf, D. Zhang, and the W7-X Team, "Demonstration of reduced neoclassical energy transport in Wendelstein 7-X," Nature, vol. 596, pp. 221–226, 2021. 5, 13, 37, 55

[20] J. H. E. Proll, Trapped-particle instabilities in quasi-isodynamic stellarators. PhD thesis, Max Plank Institute for Plasma Physics, Greifswald, Germany, 2013. 5

[21] J. H. E. Proll, P. Helander, J. W. Connor, and G. G. Plunk, "Resilience of quasi-isodynamic stellarators against trapped-particle instabilities," Physical Review Letters, vol. 108, p. 245002, Jun 2012. 5

[22] J. D. Lawson, "Some criteria for a power producing thermonuclear reactor," Proceedings of the Physical Society. Section B, vol. 70, p. 6, Jan 1957. 6

[23] J. McNally Jr, "Nuclear data in science and technology," in Proceedings of the International Conference, Paris, vol. 2, p. 41, 1973. 6

[24] J. R. McNally, "The ignition parameter tnτ and the energy multiplication factor k for fusioning plasmas," Nuclear Fusion, vol. 17, p. 1273, Dec 1977. 6

[25] "World highest fusion triple product marked in high-βp H-mode plasmas." https://www.qst.go.jp/site/jt60-english/5583.html, 2018. 6, 11

[26] R. J. Hawryluk, "Results from D-T experiments on TFTR and implications for achieving an ignited plasma," Philosophical Transactions of the Royal Society A, pp. 439–469, Mar 1999. 6

[27] JET Team, "Fusion energy production from a deuterium-tritium plasma in the JET tokamak," Nuclear Fusion, vol. 32, p. 187, Feb 1992. 6

[28] K. M. McGuire et al., "Review of deuterium-tritium results from the Tokamak Fusion Test Reactor," Physics of Plasmas, vol. 2, pp. 2176–2188, 06 1995. 6

[29] M. Keilhacker, A. Gibson, C. Gormezano, P. J. Lomas, P. R. Thomas, M. L. Watkins, P. Andrew, B. Balet, D. Borba, C. D. Challis, I. Coffey, G. A. Cottrell, H. P. L. D. Esch, N. Deliyanakis, A. Fasoli, C. W. Gowers, H. Y. Guo, G. T. A. Huysmans, T. T. C. Jones, W. Kerner, R. W. T. König, M. J. Loughlin, A. Maas, F. B. Marcus, M. F. F. Nave, F. G. Rimini, G. J. Sadler, S. E. Sharapov, G. Sips, P. Smeulders, F. X. Söldner, A. Taroni, B. J. D. Tubbing, M. G. von Hellermann, D. J. Ward, and JET Team, "High fusion performance from deuterium-tritium plasmas in JET," Nuclear Fusion, vol. 39, p. 209, Feb 1999. 6

[30] B. Bigot, "Progress toward ITER's first plasma," vol. 59, p. 112001, Jun 2019. 7, 10, 73

[31] A. J. Creely, M. J. Greenwald, S. B. Ballinger, D. Brunner, J. Canik, J. Doody, T. Fülöp, D. T. Garnier, R. Granetz, T. K. Gray, and et al., "Overview of the SPARC tokamak," Journal of Plasma Physics, vol. 86, no. 5, p. 865860502, 2020. 7

[32] S. E. Wurzel and S. C. Hsu, "Progress toward fusion energy breakeven and gain as measured against the Lawson criterion," Physics of Plasmas, vol. 29, 06 2022. 062103. 7

[33] "EUROfusion, The demonstration power plant: DEMO." https://euro-fusion.org/programme/demo/?hilite=DEMO, 2019. 7

[34] R. Alba, R. Iglesias, and M. Á. Cerdeira, "Materials to be used in future magnetic confinement fusion reactors: A review," Materials, vol. 15, no. 19, 2022. 8

[35] P. Helander, M. Drevlak, M. Zarnstorff, and S. C. Cowley, "Stellarators with permanent magnets," Physical Review Letters, vol. 124, p. 095001, Mar 2020. 8

[36] H. Zohm, Magnetohydrodynamic Stability of Tokamaks. Wiley-VCH, 2015. 8

[37] Y. Todo, "Introduction to the interaction between energetic particles and Alfvén eigenmodes in toroidal plasmas," Reviews of Modern Plasma Physics, vol. 3, 2019. 8

[38] F. C. Schuller, "Disruptions in tokamaks," Plasma Physics and Controlled Fusion, vol. 37, p. A135, Nov 1995. 8

[39] L. E. Zakharov, S. A. Galkin, S. N. Gerasimov, and J.-E. contributors, "Understanding disruptions in tokamaks," Physics of Plasmas, vol. 19, 05 2012. 055703. 8

[40] P. L. Taylor, A. G. Kellman, T. E. Evans, D. S. Gray, D. A. Humphreys, A. W. Hyatt, T. C. Jernigan, R. L. Lee, J. A. Leuer, S. C. Luckhardt, P. B. Parks, M. J. Schaffer, D. G. Whyte, and J. Zhang, "Disruption mitigation studies in DIII-D," Physics of Plasmas, vol. 6, pp. 1872–1879, 05 1999. 9

[41] J. Vega, A. Murari, S. Dormido-Canto, and et al., "Disruption prediction with artificial intelligence techniques in tokamak plasmas," Nature Physics, vol. 18, no. 5, pp. 741 – 750, 2022. 9

[42] F. Wagner, G. Becker, K. Behringer, D. Campbell, A. Eberhagen, W. Engelhardt, G. Fussmann, O. Gehre, J. Gernhardt, G. v. Gierke, G. Haas, M. Huang, F. Karger, M. Keilhacker, O. Klüber, M. Kornherr, K. Lackner, G. Lisitano, G. G. Lister, H. M. Mayer, D. Meisel, E. R. Müller, H. Murmann, H. Niedermeyer, W. Poschenrieder, H. Rapp, H. Röhr, F. Schneider, G. Siller, E. Speth, A. Stäbler, K. H. Steuer, G. Venus, O. Vollmer, and Z. Yü, "Regime of improved confinement and high beta in neutral-beam-heated divertor discharges of the ASDEX tokamak," Physical Review Letters, vol. 49, pp. 1408–1412, Nov 1982. 9

[43] Z. Sun, A. Diallo, R. Maingi, Y. Z. Qian, K. Tritz, Y. F. Wang, Y. M. Wang, A. Bortolon, A. Nagy, L. Zhang, Y. M. Duan, Y. Ye, H. L. Zhao, H. Q. Wang, X. Gu, G. Z. Zuo, W. Xu, M. Huang, C. L. Li, X. C. Meng, C. Zhou, H. Q. Liu, Q. Zang, L. Wang, J. P. Qian, G. S. Xu, X. Z. Gong, J. S. Hu, and EAST team, "Suppression of edge localized modes with real-time boron injection using the tungsten divertor in EAST," Nuclear Fusion, vol. 61, p. 014002, Dec 2020. 9, 17

[44] A. J. Wootton, B. A. Carreras, H. Matsumoto, K. McGuire, W. A. Peebles, C. P. Ritz, P. W. Terry, and S. J. Zweben, "Fluctuations and anomalous transport in tokamaks," Physics of Fluids B: Plasma Physics, vol. 2, no. 12, pp. 2879–2903, 1990. 9, 73

[45] W. Horton, "Drift waves and transport," Reviews of Modern Physics, vol. 71, pp. 735–778, Apr 1999. 10, 23, 56, 73, 79, 89

[46] R. J. Goldston and P. H. Rutherford, Introduction to Plasma Physics. CRC Press, 1995. 10

[47] P. N. Guzdar, L. Chen, W. M. Tang, and P. H. Rutherford, "Ion-temperature-gradient instability in toroidal plasmas," The Physics of Fluids, vol. 26, no. 3, pp. 673–677, 1983. 10

[48] B. Coppi and G. Rewoldt, "New trapped-electron instability," Physical Review Letters, vol. 33, pp. 1329–1332, Nov 1974. 10

[49] P. H. Diamond, S.-I. Itoh, K. Itoh, and T. S. Hahm, "Zonal flows in plasma—a review," Plasma Physics and Controlled Fusion, vol. 47, pp. R35–R161, Apr 2005. 10, 14, 74

[50] "JT-60SA construction." https://www.qst.go.jp/site/jt60-english/6599.html, 2020. 11

[51] A. Isayama, "Overview of JT-60U results towards the resolution of key physics and engineering issues in ITER and JT-60SA," Nuclear Fusion, vol. 51, p. 094010, Aug 2011. 11

[52] "JT-60SA research plan." https://www.jt60sa.org/, 2018. 11

[53] G. Giruzzi et al., "Advances in the physics studies for the JT-60SA tokamak exploitation and research plan," Plasma Physics and Controlled Fusion, vol. 62, p. 014009, Oct 2019. 11

[54] S. Coda, A. Iantchenko, S. Brunner, M. Toussaint, and K. Tanaka, "A phase-contrast-imaging core fluctuation diagnostic and first-principles turbulence modeling for JT-60SA," Nuclear Fusion, vol. 61, p. 106022, Sep 2021. 11

[55] L. Horton and JET Contributors, "Joint European Torus," in Magnetic Fusion Energy (G. H. Neilson, ed.), pp. 215–259, Woodhead Publishing, 2016. 11

[56] B. Baiocchi, J. Garcia, M. Beurskens, C. Bourdelle, F. Crisanti, C. Giroud, J. Hobirk, F. Imbeaux, I. Nunes, J. Contributors, and EU-ITM ITER Scenario Modelling Group, "Turbulent transport analysis of JET H-mode and hybrid plasmas using QuaLiKiz and Trapped Gyro Landau Fluid," Plasma Physics and Controlled Fusion, vol. 57, p. 035003, Mar. 2015. 11

[57] J. Citrin, F. Jenko, P. Mantica, D. Told, C. Bourdelle, J. Garcia, J. W. Haverkort, G. M. D. Hogeweij, T. Johnson, and M. J. Pueschel, "Nonlinear stabilization of tokamak microturbulence by fast ions," Physical Review Letters, vol. 111, p. 155001, Oct 2013. 11

[58] J. G. Cordey, D. G. Muir, V. V. Parail, G. Vayakis, S. Ali-Arshad, D. V. Bartlett, D. J. Campbell, A. L. Colton, A. E. Costley, R. D. Gill, A. Loarte, S. V. Neudachin, L. Porte, A. C. C. Sips, E. M. Springmann, P. M. Stubberfield, A. Taroni, K. Thomsen, and M. G. V. Hellermann, "Evolution of transport through the L-H transition in JET," Nuclear Fusion, vol. 35, p. 505, May 1995. 11

[59] B. Wan (on behalf of EAST Team), "Experimental Advanced Superconducting Tokamak," in Magnetic Fusion Energy (G. H. Neilson, ed.), pp. 409–437, Woodhead Publishing, 2016. 11

[60] G. M. Cao, Y. D. Li, Q. Li, X. D. Zhang, P. J. Sun, G. J. Wu, L. Q. Hu, , and the EAST Team, "Characterization of core microturbulence in L-mode and H-mode regimes on the EAST superconducting tokamak," Physica Scripta, vol. 90, p. 025603, Jan 2015. 11

[61] P. J. Sun, Y. D. Li, Y. Ren, X. D. Zhang, G. J. Wu, L. Q. Xu, R. Chen, Q. Li, H. L. Zhao, J. Z. Zhang, T. H. Shi, Y. M. Wang, B. Lyu, L. Hu, J. Li, and EAST Team, "Experimental identification of nonlinear coupling between (intermediate, small)-scale microturbulence and an MHD mode in the core of a superconducting tokamak," Nuclear Fusion, vol. 58, p. 016003, Nov 2017. 11

[62] P. J. Sun, Y. D. Li, Y. Ren, X. D. Zhang, G. J. Wu, B. Lyu, T. H. Shi, L. Q. Xu, F. D. Wang, Q. Li, J. Z. Zhang, L. Q. Hu, J. G. Li, and the EAST team, "Experimental study of the effect of 2/1 classical tearing mode on (intermediate, small)-scale microturbulence in the core of an EAST L-mode plasma," Plasma Physics and Controlled Fusion, vol. 60, p. 025019, Jan 2018. 11

[63] Y. Song, X. Zou, X. Gong, A. Becoulet, R. Buttery, P. Bonoli, T. Hoang, R. Maingi, J. Qian, X. Zhong, A. Liu, E. Li, R. Ding, J. Huang, Q. Zang, H. Liu, L. Wang, L. Zhang, G. Li, Y. Sun, A. Garofalo, T. Osborne, T. Leonard, S. G. Baek, G. Wallace, L. Xu, B. Zhang, S. Wang, Y. Chu, T. Zhang, Y. Duan, H. Lian, X. Zhang, Y. Jin, L. Zeng, B. Lyu, B. Xiao, Y. Huang, Y. Wang, B. Shen, N. Xiang, Y. Wu, J. Wu, X. Wang, B. Ding, M. Li, X. Zhang, C. Qin, W. Xi, J. Zhang, L. Huang, D. Yao, Y. Hu, G. Zuo, Q. Yuan, Z. Zhou, M. Wang, H. Xu, Y. Xie, Z. Wang, J. Chen, G. Xu, J. Hu, K. Lu, F. Liu, X. Wu, B. Wan, J. Li, and EAST Team, "Realization of thousand-second improved confinement plasma with super I-mode in Tokamak EAST," Science Advances, vol. 9, no. 1, p. eabq5273, 2023. 12

[64] D. W. Ross and W. Dorland, "Comparing simulation of plasma turbulence with experiment. II. Gyrokinetic simulations," Physics of Plasmas, vol. 9, no. 12, pp. 5031–5035, 2002. 12, 16, 23, 56, 74

[65] A. E. White, L. Schmitz, G. R. McKee, C. Holland, W. A. Peebles, T. A. Carter, M. W. Shafer, M. E. Austin, K. H. Burrell, J. Candy, J. C. DeBoo, E. J. Doyle, M. A. Makowski, R. Prater, T. L. Rhodes, G. M. Staebler, G. R. Tynan, R. E. Waltz, and G. Wang, "Measurements of core electron temperature and density fluctuations in DIII-D and comparison to nonlinear gyrokinetic simulations," Physics of Plasmas, vol. 15, no. 5, p. 056116, 2008. 12, 16, 23, 56, 74

[66] G. McKee, K. Burrell, R. Fonck, G. Jackson, M. Murakami, G. Staebler, D. Thomas, and P. West, "Impurity-induced suppression of core turbulence and transport in the DIII-D tokamak," Physical Review Letters, vol. 84, pp. 1922–1925, Feb 2000. 12, 17, 55, 89

[67] P. Liu, X. Wei, Z. Lin, G. Brochard, G. J. Choi, W. W. Heidbrink, J. H. Nicolau, and G. R. McKee, "Regulation of Alfvén eigenmodes by microturbulence in fusion plasmas," Physical Review Letters, vol. 128, p. 185001, May 2022. 12, 118

[68] S. Coda, M. Porkolab, and K. H. Burrell, "Decorrelation of edge plasma turbulence at the transition from low- to high-confinement mode in the DIIID tokamak," Physics Letters A, vol. 273, no. 1, pp. 125–131, 2000. 12

[69] P. B. Snyder, J. W. Hughes, T. H. Osborne, C. Paz-Soldan, W. Solomon, M. Knolker, D. Eldon, T. Evans, T. Golfinopoulos, B. A. Grierson, R. J. Groebner, A. E. Hubbard, E. Kolemen, B. LaBombard, F. M. Laggner, O. Meneghini, S. Mordijck, T. Petrie, S. Scott, H. Q. Wang, H. R. Wilson, and Y. B. Zhu, "High fusion performance in Super H-mode experiments on Alcator C-Mod and DIII-D," Nuclear Fusion, vol. 59, p. 086017, Jun 2019. 12

[70] R. L. Tanna, J. Ghosh, H. Raj, R. Kumar, S. Aich, V. Ranjan, K. A. Jadeja, K. M. Patel, S. B. Bhatt, K. Sathyanarayana, P. K. Chattopadhyay, M. N. Makwana, K. S. Shah, C. N. Gupta, V. K. Panchal, P. Edappala, B. Arambhadiya, M. Shah, V. Raulji, M. B. Chowdhuri, S. Banerjee, R. Manchanda, D. Raju, P. K. Atrey, U. Nagora, J. Raval, Y. S. Joisa, K. Tahiliani, S. K. Jha, and M. V. Gopalkrishana, "Plasma production and preliminary results from the ADITYA upgrade tokamak," Plasma Science and Technology, vol. 20, p. 074002, May 2018. 12, 74, 75, 89

[71] R. L. Tanna, J. Ghosh, P. K. Chattopadhyay, H. Raj, S. Patel, P. Dhyani, C. N. Gupta, K. A. Jadeja, K. M. Patel, S. B. Bhatt, V. K. Panchal, N. C. Patel, C. Chavda, E. V. Praveenlal, K. S. Shah, M. N. Makawana, S. K. Jha, M. V. Gopalkrishana, K. Tahiliani, D. Sangwan, D. Raju, U. Nagora, S. K. Pathak, P. K. Atrey, S. Purohit, J. Raval, Y. S. Joisa, C. V. S. Rao, M. B. Chowdhuri, S. Banerjee, N. Ramaiya, R. Manchanda, J. Thomas, A. Kumar, A. Kumar, P. K. Sharma, S. V. Kulkarni, K. Sathyanarayana, B. K. Shukla, A. Das, R. Jha, Y. C. Saxena, A. Sen, P. K. Kaw, D. Bora, and the ADITYA Team, "Overview of recent experimental results from the ADITYA tokamak," Nuclear Fusion, vol. 57, p. 102008, Jun 2017. 12, 74, 75, 89

[72] R. L. Tanna, H. Raj, J. Ghosh, R. Kumar, S. Aich, T. Macwan, D. Kumawat, K. A. Jadeja, K. M. Patel, M. B. Kalal, D. S. Varia, D. H. Sadharakiya, S. B. Bhatt, K. Sathyanarayana, B. K. Shukla, P. K. Chattopadhyay, M. N. Makawana, K. S. Shah, S. Gupta, V. Ranjan, V. Balakrishnan, C. N. Gupta, V. K. Panchal, P. Edappala, B. Arambhadiya, M. Shah, V. Raulji, M. B. Chowdhuri, S. Banerjee, R. Manchanda, G. Shukla, K. Shah, R. Dey, N. Yadava, S. Patel, N. Bisai, D. Raju, P. K. Atrey, S. K. Pathak, U. Nagora, J. Raval, Y. S. Joisa, M. Kumar, K. Tahiliani, S. K. Jha, M. V. Gopalkrishana, and A. Sen, "Overview of operation and experiments

in the ADITYA-U tokamak," Nuclear Fusion, vol. 59, p. 112006, Jun 2019. 12, 74, 75, 89

[73] R. L. Tanna, T. Macwan, J. Ghosh, K. A. Jadeja, R. Kumar, S. Aich, K. M. Patel, H. Raj, K. Singh, S. Dolui, A. Kumar, B. K. Shukla, P. K. Chattopadhyay, M. N. Makwana, K. S. Shah, S. Gupta, V. Balakrishnan, C. N. Gupta, V. K. Panchal, P. Edappala, B. Arambhadiya, M. Shah, P. Gautam, V. Raulji, P. Shukla, R. Rajpal, U. C. Nagora, K. Patel, N. Yadava, S. Patel, N. Ramaiya, M. B. Chowdhuri, R. Manchanda, R. Dey, G. Shukla, K. Shah, S. Varsha, J. Raval, S. Purohit, K. Tahiliani, D. Kumawat, S. K. Jha, N. Bisai, P. K. Atrey, S. K. Pathak, M. K. Gupta, M. V. Gopalkrishana, B. R. Doshi, D. Sharma, R. Srinivasan, D. Raju, C. Chauhan, Y. C. Saxena, A. Sen, R. Pal, and S. Chaturvedi, "Overview of recent experimental results from the ADITYA-U tokamak," Nuclear Fusion, vol. 62, p. 042017, Feb 2022. 12, 74, 75, 89, 101

[74] T. Macwan, H. Raj, K. Singh, S. Dolui, S. Patel, A. Kumar, P. Gautam, J. Ghosh, R. L. Tanna, K. A. Jadeja, K. M. Patel, R. Kumar, S. Aich, V. K. Panchal, U. Nagora, M. B. Chowdhuri, R. Manchanda, N. Yadava, R. Dey, K. Patel, J. Raval, S. K. Pathak, M. K. Gupta, K. Tahiliani, P. K. Chattopadhyay, A. Sen, Y. C. Saxena, R. Pal, and ADITYA-U Team, "Gas-puff induced cold pulse propagation in ADITYA-U tokamak," Nuclear Fusion, vol. 61, p. 096029, Aug 2021. 12, 75, 76, 89

[75] H. Sugama and T.-H. Watanabe, "Erratum: collisionless damping of zonal flows in helical systems [phys. plasmas 13, 012501 (2006)]," Physics of Plasmas, vol. 14, no. 7, p. 079902, 2007. 13, 37, 55

[76] A. Mishchenko, P. Helander, and A. Knies, "Collisionless dynamics of zonal flows in stellarator geometry," Physics of Plasmas, vol. 15, no. 7, p. 072309, 2008. 13, 37, 55

[77] E. M. Edlund, M. Porkolab, Z. Huang, O. Grulke, L.-G. Böttger, C. von Sehren, and A. von Stechow, "Overview of the Wendelstein 7-X phase contrast imaging diagnostic," Review of Scientific Instruments, vol. 89, no. 10, p. 10E105, 2018. 13, 16, 37

[78] R. Lunsford, C. Killer, A. Nagy, D. A. Gates, T. Klinger, A. Dinklage, G. Satheeswaran, G. Kocsis, S. A. Lazerson, F. Nespoli, N. A. Pablant, A. von Stechow, A. Alonso, T. Andreeva, M. Beurskens, C. Biedermann, S. Brezinsek, K. J. Brunner, B. Buttenschn, D. Carralero, G. Cseh, P. Drewelow, F. Effenberg, T. Estrada, O. Ford, O. Grulke, U. Hergenhahn, U. Höfel, J. Knauer, M. Krause, M. Krychowiak, S. Kwak, A. Langenberg, U. Neuner, D. Nicolai, A. Pavone, A. Puig Sitjes, K. Rahbarnia, J. Schilling, J. Svensson, T. Szepesi, H. Thomsen, T. Wauters, T. Windisch, V. Winters, D. Zhang, and L. Zsuga, "Characterization

of injection and confinement improvement through impurity induced profile modifications on the Wendelstein 7-X stellarator," Physics of Plasmas, vol. 28, no. 8, p. 082506, 2021. 13, 17, 55, 69, 89

[79] "Wendelstein 7-X reaches milestone: Power plasma with gigajoule energy turnover generated for eight minutes." https://www.ipp.mpg.de/5322229/01_23?c=5322195, 2023. 13

[80] S. Murakami, A. Wakasa, H. Maaßberg, C. D. Beidler, H. Yamada, K. Y. Watanabe, and L. Experimental Group, "Neoclassical transport optimization of LHD," Nuclear Fusion, vol. 42, p. L19, Sep 2002. 13, 55

[81] K. Tanaka, C. Michael, L. Vyacheslavov, H. Funaba, M. Yokoyama, K. Ida, M. Yoshinuma, K. Nagaoka, S. Murakami, A. Wakasa, T. Ido, A. Shimizu, M. Nishiura, Y. Takeiri, O. Kaneko, K. Tsumori, K. Ikeda, M. Osakabe, K. Kawahata, and L. E. Group, "Turbulence response in the high T_i discharge of the LHD," Plasma and Fusion Research, vol. 5, p. S2053, 2010. 13, 16, 37

[82] M. Nunami, T.-H. Watanabe, H. Sugama, and K. Tanaka, "Linear gyrokinetic analyses of ITG modes and zonal flows in LHD with high ion temperature," Plasma and Fusion Research, vol. 6, pp. 1403001–1403001, 2011. 13, 16, 37, 55

[83] M. Nunami, T.-H. Watanabe, H. Sugama, and K. Tanaka, "Gyrokinetic turbulent transport simulation of a high ion temperature plasma in large helical device experiment," Physics of Plasmas, vol. 19, no. 4, p. 042504, 2012. 13, 16, 37, 55

[84] K. Tanaka, M. Nakata, Y. Ohtani, T. Tokuzawa, H. Yamada, F. Warmer, M. Nunami, S. Satake, T. Tala, T. Tsujimura, Y. Takemura, T. Kinoshita, H. Takahashi, M. Yokoyama, R. Seki, H. Igami, Y. Yoshimura, S. Kubo, T. Shimozuma, T. Akiyama, I. Yamada, R. Yasuhara, H. Funaba, M. Yoshinuma, K. Ida, M. Goto, G. Motojima, M. Shoji, S. Masuzaki, C. A. Michael, L. N. Vacheslavov, M. Osakabe, and T. M. and, "Extended investigations of isotope effects on ECRH plasma in LHD," Plasma Physics and Controlled Fusion, vol. 62, p. 024006, Dec 2019. 13, 16, 37

[85] F. Nespoli, N. Ashikawa, E. P. Gilson, R. Lunsford, S. Masuzaki, M. Shoji, T. Oishi, C. Suzuki, A. Nagy, A. Mollen, N. A. Pablant, K. Ida, M. Yoshinuma, N. Tamura, D. A. Gates, and T. Morisaki, "First impurity powder injection experiments in LHD," Nuclear Materials and Energy, vol. 25, p. 100842, 2020. 13, 17, 55, 67

[86] F. Nespoli, S. Masuzaki, K. Tanaka, N. Ashikawa, M. Shoji, E. P. Gilson, R. Lunsford, T. Oishi, K. Ida, M. Yoshinuma, Y. Takemura, T. Kinoshita, G. Motojima, N. Kenmochi, G. Kawamura, C. Suzuki, A. Nagy, A. Bortolon, N. A. Pablant,

A. Mollen, N. Tamura, D. A. Gates, and T. Morisaki, "Observation of a reduced-turbulence regime with boron powder injection in a stellarator," Nature Physics, vol. 18, no. 3, pp. 350–356, 2022. 13, 17, 55, 56, 59, 63, 66, 67, 89

[87] R. M. Magee, K. Ogawa, T. Tajima, and et al., "First measurements of $p^{11}b$ fusion in a magnetically confined plasma," Nature Communications, vol. 18, p. 6, 2023. 13

[88] X. Garbet, Y. Idomura, L. Villard, and T.-H. Watanabe, "Gyrokinetic simulations of turbulent transport," Nuclear Fusion, vol. 50, p. 043002, Mar 2010. 14, 26, 73, 79

[89] A. J. Brizard and T. S. Hahm, "Foundations of nonlinear gyrokinetic theory," Reviews of Modern Physics, vol. 79, pp. 421–468, Apr 2007. 14, 25, 27

[90] J. R. Cary, "Lie transform perturbation theory for Hamiltonian systems," Physics Reports, vol. 79, no. 2, pp. 129–159, 1981. 15

[91] J. R. Cary and R. G. Littlejohn, "Noncanonical Hamiltonian mechanics and its application to magnetic field line flow," Annals of Physics, vol. 151, no. 1, pp. 1–34, 1983. 15

[92] C. K. Birdsall, Plasma theory and simulation. Defense Technical Information Center, 1985. 15, 28, 104

[93] Z. Lin, T. S. Hahm, W. W. Lee, W. M. Tang, and R. B. White, "Turbulent transport reduction by zonal flows: Massively parallel simulations," Science, vol. 281, no. 5384, pp. 1835–1837, 1998. 15, 23, 38, 74, 98

[94] S. Jolliet, A. Bottino, P. Angelino, R. Hatzky, T. M. Tran, B. F. Mcmillan, O. Sauter, K. Appert, Y. Idomura, and L. Villard, "A global collisionless PIC code in magnetic coordinates," Computer Physics Communications, vol. 177, no. 5, pp. 409–425, 2007. 15, 23

[95] W. X. Wang, T. S. Hahm, W. W. Lee, G. Rewoldt, J. Manickam, and W. M. Tang, "Nonlocal properties of gyrokinetic turbulence and the role of EB flow shear," Physics of Plasmas, vol. 14, 07 2007. 072306. 15

[96] Y. Idomura, S. Tokuda, and Y. Kishimoto, "Global gyrokinetic simulation of ion temperature gradient driven turbulence in plasmas using a canonical Maxwellian distribution," Nuclear Fusion, vol. 43, p. 234, Mar 2003. 15

[97] S. E. Parker and W. W. Lee, "A fully nonlinear characteristic method for gyrokinetic simulation," Physics of Fluids B: Plasma Physics, vol. 5, no. 1, pp. 77–86, 1993. 15, 23, 24, 28, 39, 105

[98] R. Courant, K. Friedrichs, and H. Lewy, "On the Partial Difference Equations of Mathematical Physics," Math. Ann., vol. 100, 12 1928. 15

[99] M. Kotschenreuther, G. Rewoldt, and W. M. Tang, "Comparison of initial value and eigenvalue codes for kinetic toroidal plasma instabilities," Computer Physics Communications, vol. 88, no. 2, pp. 128–140, 1995. 15

[100] W. Dorland, F. Jenko, M. Kotschenreuther, and B. N. Rogers, "Electron temperature gradient turbulence," Physical Review Letters, vol. 85, pp. 5579–5582, Dec 2000. 15

[101] T.-H. Watanabe and H. Sugama, "Velocity–space structures of distribution function in toroidal ion temperature gradient turbulence," Nuclear Fusion, vol. 46, pp. 24–32, Dec 2005. 15, 23

[102] A. G. Peeters and D. Strintzi, "The effect of a uniform radial electric field on the toroidal ion temperature gradient mode," Physics of Plasmas, vol. 11, pp. 3748–3751, 06 2004. 15

[103] J. Candy and R. E. Waltz, "Anomalous transport scaling in the DIII-D tokamak matched by supercomputer simulation," Physical Review Letters, vol. 91, p. 045001, Jul 2003. 15, 73

[104] F. Jenko, W. Dorland, M. Kotschenreuther, and B. N. Rogers, "Electron temperature gradient driven turbulence," Physics of Plasmas, vol. 7, no. 5, pp. 1904–1910, 2000. 15, 23

[105] Y. Idomura, M. Ida, T. Kano, N. Aiba, and S. Tokuda, "Conservative global gyrokinetic toroidal full-f five-dimensional Vlasov simulation," Computer Physics Communications, vol. 179, no. 6, pp. 391–403, 2008. 15

[106] M. Brunetti, V. Grandgirard, O. Sauter, J. Vaclavik, and L. Villard, "A semi-Lagrangian code for nonlinear global simulations of electrostatic drift-kinetic ITG modes," Computer Physics Communications, vol. 163, no. 1, pp. 1–21, 2004. 16

[107] V. Grandgirard, M. Brunetti, P. Bertrand, N. Besse, X. Garbet, P. Ghendrih, G. Manfredi, Y. Sarazin, O. Sauter, E. Sonnendrücker, J. Vaclavik, and L. Villard, "A drift-kinetic semi-Lagrangian 4D code for ion turbulence simulation," Journal of Computational Physics, vol. 217, no. 2, pp. 395–423, 2006. 16

[108] V. Grandgirard, Y. Sarazin, P. Angelino, A. Bottino, N. Crouseilles, G. Darmet, G. Dif-Pradalier, X. Garbet, P. Ghendrih, S. Jolliet, G. Latu, E. Sonnendrücker, and L. Villard, "Global full-f gyrokinetic simulations of plasma turbulence," Plasma Physics and Controlled Fusion, vol. 49, pp. B173–B182, Nov 2007. 16, 23

[109] N. T. Howard, A. E. White, M. L. Reinke, M. Greenwald, C. Holland, J. Candy, and J. R. Walk, "Validation of the gyrokinetic model in ITG and TEM dominated L-mode plasmas," Nuclear Fusion, vol. 53, p. 123011, Nov 2013. 16, 56, 74

[110] T.-H. Watanabe, H. Sugama, and S. Ferrando-Margalet, "Reduction of turbulent transport with zonal flows enhanced in helical systems," Physical Review Letters, vol. 100, p. 195002, May 2008. 16, 37, 57

[111] M. Nakata, M. Nunami, H. Sugama, and T.-H. Watanabe, "Impact of hydrogen isotope species on microinstabilities in helical plasmas," Plasma Physics and Controlled Fusion, vol. 58, p. 074008, Jun 2016. 16, 37, 41, 46, 49, 57

[112] M. Nakata, M. Nunami, H. Sugama, and T.-H. Watanabe, "Isotope effects on trapped-electron-mode driven turbulence and zonal flows in helical and tokamak plasmas," Physical Review Letters, vol. 118, p. 165002, Apr 2017. 16, 37, 41, 46, 49, 57

[113] J. Riemann, R. Kleiber, and M. Borchardt, "Effects of radial electric fields on linear ITG instabilities in W7-X and LHD," Plasma Physics and Controlled Fusion, vol. 58, p. 074001, May 2016. 17, 38, 39, 48, 57, 67

[114] H. Y. Wang, I. Holod, Z. Lin, J. Bao, J. Y. Fu, P. F. Liu, J. H. Nicolau, D. Spong, and Y. Xiao, "Global gyrokinetic particle simulations of microturbulence in W7-X and LHD stellarators," Physics of Plasmas, vol. 27, no. 8, p. 082305, 2020. 17, 24, 38, 40, 41, 45, 46, 57, 74

[115] J. Y. Fu, J. H. Nicolau, P. F. Liu, X. S. Wei, Y. Xiao, and Z. Lin, "Global gyrokinetic simulation of neoclassical ambipolar electric field and its effects on microturbulence in W7-X stellarator," Physics of Plasmas, vol. 28, no. 6, p. 062309, 2021. 17, 38, 57

[116] M. D. J. Cole, T. Moritaka, R. Hager, J. Dominski, S. Ku, and C. S. Chang, "Nonlinear global gyrokinetic delta-f turbulence simulations in a quasi-axisymmetric stellarator," Physics of Plasmas, vol. 27, no. 4, p. 044501, 2020. 17, 38, 57

[117] A. B. Navarro, G. Merlo, G. G. Plunk, P. Xanthopoulos, A. von Stechow, A. D. Siena, M. Maurer, F. Hindenlang, F. Wilms, and F. Jenko, "Global gyrokinetic simulations of ITG turbulence in the magnetic configuration space of the Wendelstein 7-X stellarator," Plasma Physics and Controlled Fusion, vol. 62, p. 105005, Aug 2020. 17, 38, 41

[118] J. L. V. Lewandowski, G. Rewoldt, S. Ethier, W. W. Lee, and Z. Lin, "Global particle-in-cell simulations of microturbulence with kinetic electrons," Physics of Plasmas, vol. 13, no. 7, p. 072306, 2006. 17, 38, 42, 57

[119] Z. Lin, Y. Nishimura, Y. Xiao, I. Holod, W. L. Zhang, and L. Chen, "Global gyrokinetic particle simulations with kinetic electrons," Plasma Physics and Controlled Fusion, vol. 49, pp. B163–B172, Nov 2007. 17, 29, 38, 42, 57, 118

[120] Y. Xiao and Z. Lin, "Turbulent transport of trapped-electron modes in collisionless plasmas," Physical Review Letters, vol. 103, p. 085004, Aug 2009. 17, 24, 38, 39, 57, 98

[121] H. W. Kugel, M. G. Bell, H. Schneider, J. P. Allain, R. E. Bell, R. Kaita, J. Kallman, S. Kaye, B. P. LeBlanc, D. Mansfield, R. E. Nygren, R. Maingi, J. Menard, D. Mueller, M. Ono, S. Paul, S. Gerhardt, R. Raman, S. Sabbagh, C. H. Skinner, V. Soukhanovskii, J. Timberlake, and L. E. Zakharov, "Lithium coatings on NSTX plasma facing components and its effects on boundary control, core plasma performance, and operation," Fusion Engineering and Design, vol. 85, no. 6, pp. 865–873, 2010. Proceedings of the 1st International Workshop on Lithium Applications for the Boundary Control in Fusion Devices. 17

[122] E. P. Gilson, H. H. Lee, A. Bortolon, W. Choe, A. Diallo, S. H. Hong, H. M. Lee, J. Lee, R. Maingi, D. K. Mansfield, A. Nagy, S. H. Park, I. W. Song, J. I. Song, S. W. Yun, S. W. Yoon, and R. Nazikian, "Wall conditioning and ELM mitigation with boron nitride powder injection in KSTAR," Nuclear Materials and Energy, vol. 28, p. 101043, 2021. 17

[123] A. Bortolon, R. Maingi, A. Nagy, J. Ren, J. D. Duran, A. Maan, D. C. Donovan, J. A. Boedo, D. L. Rudakov, A. W. Hyatt, T. W. Wilks, M. W. Shafer, C. M. Samuell, M. E. Fenstermacher, E. P. Gilson, R. Lunsford, D. K. Mansfield, T. Abrams, and R. Nazikian, "Observations of wall conditioning by means of boron powder injection in DIII-D H-mode plasmas," Nuclear Fusion, vol. 60, p. 126010, Sep 2020. 17

[124] R. Lunsford, V. Rohde, A. Bortolon, R. Dux, A. Herrmann, A. Kallenbach, R. M. McDermott, P. David, A. Drenik, F. Laggner, R. Maingi, D. K. Mansfield, A. Nagy, R. Neu, E. Wolfrum, and the ASDEX Upgrade team, "Active conditioning of asdex upgrade tungsten plasma-facing components and discharge enhancement through boron and boron nitride particulate injection," Nuclear Fusion, vol. 59, p. 126034, Oct 2019. 17

[125] Z. Sun, R. Maingi, J. S. Hu, W. Xu, G. Z. Zuo, Y. W. Yu, C. R. Wu, M. Huang, X. C. Meng, L. Zhang, L. Wang, S. T. Mao, F. Ding, D. K. Mansfield, J. Canik, R. Lunsford, A. Bortolon, and X. Z. Gong, "Real time wall conditioning with lithium powder injection in long pulse H-mode plasmas in EAST with tungsten divertor," Nuclear Materials and Energy, vol. 19, pp. 124–130, 2019. 17

[126] R. Maingi, D. P. Boyle, J. M. Canik, S. M. Kaye, C. H. Skinner, J. P. Allain, M. G. Bell, R. E. Bell, S. P. Gerhardt, T. K. Gray, M. A. Jaworski, R. Kaita, H. W. Kugel,

B. P. LeBlanc, J. Manickam, D. K. Mansfield, J. E. Menard, T. H. Osborne, R. Raman, A. L. Roquemore, S. A. Sabbagh, P. B. Snyder, and V. A. Soukhanovskii, "The effect of progressively increasing lithium coatings on plasma discharge characteristics, transport, edge profiles and elm stability in the national spherical torus experiment," Nuclear Fusion, vol. 52, p. 083001, Jun 2012. 17

[127] A. Loarte, B. Lipschultz, A. S. Kukushkin, G. F. Matthews, P. C. Stangeby, N. Asakura, G. F. Counsell, G. Federici, A. Kallenbach, K. Krieger, A. Mahdavi, V. Philipps, D. Reiter, J. Roth, J. Strachan, D. Whyte, R. Doerner, T. Eich, W. Fundamenski, A. Herrmann, M. Fenstermacher, P. Ghendrih, M. Groth, A. Kirschner, S. Konoshima, B. LaBombard, P. Lang, A. W. Leonard, P. Monier-Garbet, R. Neu, H. Pacher, B. Pegourie, R. A. Pitts, S. Takamura, J. Terry, E. Tsitrone, the ITPA Scrape-off Layer, and D. P. T. Group, "Chapter 4: Power and particle control," Nuclear Fusion, vol. 47, p. S203, Jun 2007. 18, 97

[128] Z. Lin, S. Ethier, T. S. Hahm, and W. M. Tang, "Size scaling of turbulent transport in magnetically confined plasmas," Physical Review Letters, vol. 88, p. 195004, Apr 2002. 23, 73

[129] J. Candy and R. E. Waltz, "An Eulerian gyrokinetic-Maxwell solver," Journal of Computational Physics, vol. 186, no. 2, pp. 545–581, 2003. 23

[130] Z. Lu, G. Meng, R. Hatzky, M. Hoelzl, and P. Lauber, "Full-f and gyrokinetic particle simulations of Alfvén waves and energetic particle physics," Plasma Physics and Controlled Fusion, vol. 65, p. 034004, Feb 2023. 24

[131] Y. Xiao, I. Holod, Z. Wang, Z. Lin, and T. Zhang, "Gyrokinetic particle simulation of microturbulence for general magnetic geometry and experimental profiles," Physics of Plasmas, vol. 22, no. 2, p. 022516, 2015. 24, 26, 30, 39, 112

[132] Z. Wang, Z. Lin, I. Holod, W. W. Heidbrink, B. Tobias, M. Van Zeeland, and M. E. Austin, "Radial localization of toroidicity-induced Alfvén eigenmodes," Physical Review Letters, vol. 111, p. 145003, Oct 2013. 24, 39

[133] J. Bao, Z. Lin, A. Kuley, and Z. X. Lu, "Particle simulation of lower hybrid wave propagation in fusion plasmas," Plasma Physics and Controlled Fusion, vol. 56, p. 095020, Aug 2014. 24, 39

[134] W. Zhang, Z. Lin, and L. Chen, "Transport of energetic particles by microturbulence in magnetized plasmas," Physical Review Letters, vol. 101, p. 095001, Aug 2008. 24, 39

[135] T. Singh, D. Sharma, T. Macwan, S. Sharma, J. Ghosh, A. Sen, Z. Lin, and A. Kuley, "Gyrokinetic simulations of electrostatic microturbulence in ADITYA-U tokamak," Nuclear Fusion, vol. 63, p. 056008, Mar 2023. 24, 33, 56, 65, 89, 92

[136] Y. Ma, B. Zhang, J. Bao, Z. Lin, W. Zhang, H. Cai, and D. Li, "Electrostatic turbulence in EAST plasmas with internal transport barrier," Nuclear Fusion, vol. 63, p. 056014, Mar 2023. 24

[137] C. K. Lau, D. P. Fulton, I. Holod, Z. Lin, M. Binderbauer, T. Tajima, and L. Schmitz, "Drift-wave stability in the field-reversed configuration," Physics of Plasmas, vol. 24, no. 8, p. 082512, 2017. 24

[138] K. Madduri, K. Z. Ibrahim, S. Williams, E.-J. Im, S. Ethier, J. Shalf, and L. Oliker, "Gyrokinetic toroidal simulations on leading multi- and manycore HPC systems," in Proceedings of 2011 International Conference for High Performance Computing, Networking, Storage and Analysis, SC '11, (New York, NY, USA), Association for Computing Machinery, 2011. 24, 32, 34, 35

[139] B. Wang, S. Ethier, W. Tang, K. Z. Ibrahim, K. Madduri, S. Williams, and L. Oliker, "Modern gyrokinetic particle-in-cell simulation of fusion plasmas on top supercomputers," The International Journal of High Performance Computing Applications, vol. 33, no. 1, pp. 169–188, 2019. 24, 35

[140] W. W. Lee, "Gyrokinetic particle simulation model," Journal of Computational Physics, vol. 72, no. 1, pp. 243 – 269, 1987. 25, 29, 33

[141] E. A. Frieman and L. Chen, "Nonlinear gyrokinetic equations for low frequency electromagnetic waves in general plasma equilibria," The Physics of Fluids, vol. 25, pp. 502–508, 03 1982. 25

[142] S. Ethier, W. M. Tang, and Z. Lin, "Gyrokinetic particle-in-cell simulations of plasma microturbulence on advanced computing platforms," Journal of Physics: Conference Series, vol. 16, p. 1, Jan 2005. 26

[143] L. L. Lao, H. S. John, R. D. Stambaugh, A. G. Kellman, and W. Pfeiffer, "Reconstruction of current profile parameters and plasma shapes in tokamaks," Nuclear Fusion, vol. 25, pp. 1611–1622, Nov 1985. 26, 101

[144] D. Sharma, R. Srinivasan, J. Ghosh, and P. Chattopadhyay, "Aditya upgradation equilibrium study," Fusion Engineering and Design, vol. 160, p. 111933, 2020. 26, 76

[145] S. Hirshman and J. Whitson, "Steepest-descent moment method for three-dimensional magnetohydrodynamic equilibria," The Physics of Fluids, vol. 26, no. 12, pp. 3553–3568, 1983. 26, 39, 59

[146] Z. Lin, W. M. Tang, and W. W. Lee, "Gyrokinetic particle simulation of neoclassical transport," Physics of Plasmas, vol. 2, no. 8, pp. 2975–2988, 1995. 27, 33

[147] I. Holod, W. L. Zhang, Y. Xiao, and Z. Lin, "Electromagnetic formulation of global gyrokinetic particle simulation in toroidal geometry," Physics of Plasmas, vol. 16, no. 12, p. 122307, 2009. 28

[148] R. D. Sydora, V. K. Decyk, and J. M. Dawson, "Fluctuation-induced heat transport results from a large global 3D toroidal particle simulation model," Plasma Physics and Controlled Fusion, vol. 38, p. A281, Dec 1996. 29

[149] "PETSc: Portable, Extensible Toolkit for Scientific computation, Mathematics and Computer Science Division, Argonne National Laboratory.." 31, 105

[150] R. D. Falgout and U. M. Yang, "Hypre: A library of high performance preconditioners," in Computational Science — ICCS 2002 (P. M. A. Sloot, A. G. Hoekstra, C. J. K. Tan, and J. J. Dongarra, eds.), (Berlin, Heidelberg), pp. 632–641, Springer Berlin Heidelberg, 2002. 31, 105

[151] A. C. J., S. Brunner, and J. Ball, "Effect of collisions on non-adiabatic electron dynamics in ITG-driven microturbulence," Physics of Plasmas, vol. 28, no. 9, p. 092303, 2021. 33, 74

[152] J. Lang, Y. Chen, and S. E. Parker, "Gyrokinetic δf particle simulation of trapped electron mode driven turbulence," Physics of Plasmas, vol. 14, no. 8, p. 082315, 2007. 33, 39, 47, 48, 53, 57, 65, 74, 92

[153] F. Ryter, C. Angioni, A. G. Peeters, F. Leuterer, H.-U. Fahrbach, and W. Suttrop, "Experimental study of trapped-electron-mode properties in tokamaks: Threshold and stabilization by collisions," Physical Review Letters, vol. 95, p. 085001, Aug 2005. 33, 74, 83

[154] W. Hu, H.-Y. Feng, and C. Dong, "Collisional effects on drift wave microturbulence in tokamak plasmas," Chinese Physics Letters, vol. 35, p. 105201, Oct 2018. 33, 74

[155] M. Osakabe, Y. Takeiri, T. Morisaki, G. Motojima, K. Ogawa, M. Isobe, M. Tanaka, S. Murakami, A. Shimizu, K. Nagaoka, H. Takahashi, K. Nagasaki, H. Takahashi, T. Fujita, Y. Oya, M. Sakamoto, Y. Ueda, T. Akiyama, H. Kasahara, S. Sakakibara, R. Sakamoto, M. Tokitani, H. Yamada, M. Yokoyama, Y. Yoshimura, and L. E. Group, "Current status of large helical device and its prospect for deuterium experiment," Fusion Science and Technology, vol. 72, no. 3, pp. 199–210, 2017. 37, 55

[156] A. Zocco, A. Mishchenko, A. Knies, M. Falessi, and F. Zonca, "Nonlinear drift-wave and energetic particle long-time behaviour in stellarators: solution of the kinetic problem," Journal of Plasma Physics, vol. 89, no. 3, p. 905890307, 2023. 38

[157] J. H. Nicolau, G. Choi, J. Fu, P. Liu, X. Wei, and Z. Lin, "Global gyrokinetic simulation with kinetic electron for collisionless damping of zonal flow in stellarators," Nuclear Fusion, vol. 61, p. 126041, Nov 2021. 38, 40, 57, 74

[158] J. Nicolau, Z. Lin, G. Choi, P. Liu, X. Wei, and G. Brochard, "Gyrokinetic simulations of the helically trapped electron mode in the W7-X stellarator," in APS Division of Plasma Physics Meeting Abstracts, vol. 2021 of APS Meeting Abstracts, p. PP11.079, Jan. 2021. 38, 39, 57

[159] F. Wilms, A. B. Navarro, G. Merlo, L. Leppin, T. Görler, T. Dannert, F. Hindenlang, and F. Jenko, "Global electromagnetic turbulence simulations of W7-X-like plasmas with GENE-3D," Journal of Plasma Physics, vol. 87, no. 6, p. 905870604, 2021. 38, 41, 57, 67, 117

[160] K. D. Makwana, P. W. Terry, M. J. Pueschel, and D. R. Hatch, "Subdominant modes in zonal-flow-regulated turbulence," Physical Review Letters, vol. 112, p. 095002, Mar 2014. 39, 47, 57, 65, 92

[161] L. Chen, Z. Lin, and R. White, "Excitation of zonal flow by drift waves in toroidal plasmas," Physics of Plasmas, vol. 7, no. 8, pp. 3129–3132, 2000. 39, 47, 57, 65, 92

[162] F. Merz and F. Jenko, "Nonlinear saturation of trapped electron modes via perpendicular particle diffusion," Physical Review Letters, vol. 100, p. 035005, Jan 2008. 39, 47, 57, 65, 92

[163] J. Lang, S. E. Parker, and Y. Chen, "Nonlinear saturation of collisionless trapped electron mode turbulence: Zonal flows and zonal density," Physics of Plasmas, vol. 15, no. 5, p. 055907, 2008. 39, 47, 48, 53, 57, 65, 74, 92

[164] D. R. Ernst, J. Lang, W. M. Nevins, M. Hoffman, Y. Chen, W. Dorland, and S. Parker, "Role of zonal flows in trapped electron mode turbulence through nonlinear gyrokinetic particle and continuum simulation," Physics of Plasmas, vol. 16, no. 5, p. 055906, 2009. 39, 47, 48, 53, 57, 65, 74, 82, 92

[165] T. Dannert and F. Jenko, "Gyrokinetic simulation of collisionless trapped-electron mode turbulence," Physics of Plasmas, vol. 12, no. 7, p. 072309, 2005. 39, 47, 57, 65, 74, 82, 92

[166] Y. Xiao, I. Holod, W. Zhang, S. Klasky, and Z. Lin, "Fluctuation characteristics and transport properties of collisionless trapped electron mode turbulence," Physics of Plasmas, vol. 17, no. 2, p. 022302, 2010. 39, 47, 65, 74, 82, 92

[167] S. Toda, M. Nunami, and H. Sugama, "Reduced models of turbulent transport in helical plasmas including effects of zonal flows and trapped electrons," Journal of Plasma Physics, vol. 86, no. 3, p. 815860304, 2020. 39, 65

[168] I. Holod, Z. Lin, S. Taimourzadeh, R. Nazikian, D. Spong, and A. Wingen, "Effect of resonant magnetic perturbations on microturbulence in DIII-D pedestal," Nuclear Fusion, vol. 57, p. 016005, Oct 2016. 39, 40

[169] E. Sánchez, A. Mishchenko, J. García-Regaña, R. Kleiber, A. Bottino, L. Villard, and the W7-X team, "Nonlinear gyrokinetic PIC simulations in stellarators with the code EUTERPE," Journal of Plasma Physics, vol. 86, no. 5, p. 855860501, 2020. 41, 57

[170] M. D. J. Cole, R. Hager, T. Moritaka, J. Dominski, R. Kleiber, S. Ku, S. Lazerson, J. Riemann, and C. S. Chang, "Verification of the global gyrokinetic stellarator code XGC-S for linear ion temperature gradient driven modes," Physics of Plasmas, vol. 26, no. 8, p. 082501, 2019. 41

[171] P. Xanthopoulos, S. A. Bozhenkov, M. N. Beurskens, H. M. Smith, G. G. Plunk, P. Helander, C. D. Beidler, J. A. Alcusón, A. Alonso, A. Dinklage, O. Ford, G. Fuchert, J. Geiger, J. H. E. Proll, M. J. Pueschel, Y. Turkin, F. Warmer, and the W7-X Team, "Turbulence mechanisms of enhanced performance stellarator plasmas," Physical Review Letters, vol. 125, p. 075001, Aug 2020. 48

[172] D. P. Fulton, Z. Lin, I. Holod, and Y. Xiao, "Microturbulence in DIII-D tokamak pedestal. I. Electrostatic Instabilities," Physics of Plasmas, vol. 21, no. 4, p. 042110, 2014. 49, 81

[173] Z. Lin, L. Chen, and F. Zonca, "Role of nonlinear toroidal coupling in electron temperature gradient turbulence," Physics of Plasmas, vol. 12, no. 5, p. 056125, 2005. 49

[174] H. Chen and L. Chen, "How zonal flow affects trapped-electron-driven turbulence in tokamak plasmas," Physical Review Letters, vol. 128, p. 025003, Jan 2022. 54

[175] F. Warmer, K. Tanaka, P. Xanthopoulos, M. Nunami, M. Nakata, C. D. Beidler, S. A. Bozhenkov, M. N. A. Beurskens, K. J. Brunner, O. P. Ford, G. Fuchert, H. Funaba, J. Geiger, D. Gradic, K. Ida, H. Igami, S. Kubo, A. Langenberg, H. P. Laqua, S. Lazerson, T. Morisaki, M. Osakabe, N. Pablant, E. Pasch, B. Peterson, S. Satake, R. Seki, T. Shimozuma, H. M. Smith, T. Stange, A. v. Stechow, H. Sugama, Y. Suzuki, H. Takahashi, T. Tokuzawa, T. Tsujimura, Y. Turkin, R. C. Wolf, I. Yamada, R. Yanai, R. Yasuhara, M. Yokoyama, Y. Yoshimura, M. Yoshinuma, D. Zhang, and W7-X Team and LHD Experimental Group, "Impact of magnetic field configuration on heat transport in stellarators and heliotrons," Physical Review Letters, vol. 127, p. 225001, Nov 2021. 55

[176] H. Urano, M. Nakata, N. Aiba, H. Kubo, M. Honda, N. Hayashi, M. Yoshida, Y. Kamada, and the JT-60 Team, "Roles of argon seeding in energy confinement

and pedestal structure in JT-60U," Nuclear Fusion, vol. 55, p. 033010, Feb 2015. 55, 89

[177] M. Nakata, "Microinstability and zonal-flow response in mixture plasmas with medium-Z and nonthermal impurity," Plasma and Fusion Research, vol. 17, pp. 1203078–1203078, 2022. 55, 89

[178] E. Hinnov, K. Bol, D. Dimock, R. J. Hawryluk, D. Johnson, M. Mattioli, E. Meservey, and S. V. Goeler, "Effects of tungsten radiation on the behaviour of PLT tokamak discharges," Nuclear Fusion, vol. 18, p. 1305, Sep 1978. 55

[179] K. Itoh, S.-I. Itoh, and L. Giannone, "Modelling of density limit phenomena in toroidal helical plasmas," Journal of the Physical Society of Japan, vol. 70, no. 11, pp. 3274–3284, 2001. 55

[180] F. J. Casson, R. M. McDermott, C. Angioni, Y. Camenen, R. Dux, E. Fable, R. Fischer, B. Geiger, P. Manas, L. Menchero, G. Tardini, and the ASDEX Upgrade Team, "Validation of gyrokinetic modelling of light impurity transport including rotation in ASDEX Upgrade," Nuclear Fusion, vol. 53, p. 063026, May 2013. 56

[181] Y. Turkin, C. D. Beidler, H. Maaßberg, S. Murakami, V. Tribaldos, and A. Wakasa, "Neoclassical transport simulations for stellarators," Physics of Plasmas, vol. 18, no. 2, p. 022505, 2011. 56

[182] M. Landreman, H. M. Smith, A. Mollén, and P. Helander, "Comparison of particle trajectories and collision operators for collisional transport in nonaxisymmetric plasmas," Physics of Plasmas, vol. 21, no. 4, p. 042503, 2014. 56, 67

[183] S. Matsuoka, S. Satake, M. Yokoyama, A. Wakasa, and S. Murakami, "Neoclassical electron transport calculation by using δf Monte Carlo method," Physics of Plasmas, vol. 18, no. 3, p. 032511, 2011. 56

[184] D. A. Spong, "Generation and damping of neoclassical plasma flows in stellarators," Physics of Plasmas, vol. 12, no. 5, p. 056114, 2005. 56

[185] T. Singh, J. H. Nicolau, Z. Lin, S. Sharma, A. Sen, and A. Kuley, "Global gyrokinetic simulations of electrostatic microturbulent transport using kinetic electrons in LHD stellarator," Nuclear Fusion, vol. 62, p. 126006, Oct 2022. 56, 57, 58, 65, 74

[186] K. Nagaoka, H. Takahashi, M. Nakata, S. Satake, K. Tanaka, K. Mukai, M. Yokoyama, H. Nakano, S. Murakami, K. Ida, M. Yoshinuma, S. Ohdachi, T. Bando, M. Nunami, R. Seki, H. Yamaguchi, M. Osakabe, T. Morisaki, and the LHD Experiment Group, "Transport characteristics of deuterium and hydrogen

plasmas with ion internal transport barrier in the Large Helical Device," Nuclear Fusion, vol. 59, p. 106002, Aug 2019. 57

[187] M. Nakata, K. Nagaoka, K. Tanaka, H. Takahashi, M. Nunami, S. Satake, M. Yokoyama, F. Warmer, and the LHD Experiment Group, "Gyrokinetic microinstability analysis of high-ti and high-te isotope plasmas in Large Helical Device," Plasma Physics and Controlled Fusion, vol. 61, p. 014016, Nov 2018. 57

[188] A. B. Navarro, G. Merlo, G. G. Plunk, P. Xanthopoulos, A. von Stechow, A. D. Siena, M. Maurer, F. Hindenlang, F. Wilms, and F. Jenko, "Global gyrokinetic simulations of ITG turbulence in the magnetic configuration space of the Wendelstein 7-X stellarator," Plasma Physics and Controlled Fusion, vol. 62, p. 105005, Aug 2020. 57

[189] W. M. Tang, P. H. Rutherford, H. P. Furth, and J. C. Adam, "Stabilization of trapped-particle modes by reversed-gradient profiles," Physical Review Letters, vol. 35, pp. 660–663, Sep 1975. 61

[190] T. S. Hahm and W. M. Tang, "Properties of ion temperature gradient drift instabilities in H-mode plasmas," Physics of Fluids B: Plasma Physics, vol. 1, no. 6, pp. 1185–1192, 1989. 61

[191] K. Tanaka, C. A. Michael, L. N. Vyacheslavov, A. L. Sanin, K. Kawahata, T. Akiyama, T. Tokuzawa, and S. Okajima, "Two-dimensional phase contrast imaging for local turbulence measurements in large helical device (invited)," Review of Scientific Instruments, vol. 79, no. 10, p. 10E702, 2008. 66, 67

[192] A. Mollén, M. Landreman, H. M. Smith, J. M. García-Regaña, and M. Nunami, "Flux-surface variations of the electrostatic potential in stellarators: impact on the radial electric field and neoclassical impurity transport," Plasma Physics and Controlled Fusion, vol. 60, p. 084001, Jun 2018. 67

[193] K. Fujita, S. Satake, R. Kanno, M. Nunami, M. Nakata, J. M. García-Regaña, J. L. Velasco, and I. Calvo, "Global calculation of neoclassical impurity transport including the variation of electrostatic potential," Journal of Plasma Physics, vol. 86, no. 3, p. 905860319, 2020. 67

[194] B. Scott, "Three-dimensional computation of drift Alfvén turbulence," Plasma Physics and Controlled Fusion, vol. 39, p. 1635, Oct 1997. 67, 75, 117

[195] S. Maeyama, A. Ishizawa, T.-H. Watanabe, M. Nakata, N. Miyato, M. Yagi, and Y. Idomura, "Comparison between kinetic-ballooning-mode-driven turbulence and ion-temperature-gradient-driven turbulence," Physics of Plasmas, vol. 21, 05 2014. 052301. 67, 117

[196] G. G. Whelan, M. J. Pueschel, and P. W. Terry, "Nonlinear electromagnetic stabilization of plasma microturbulence," Physical Review Letters, vol. 120, p. 175002, Apr 2018. 67, 117

[197] C. Angioni, "Impurity transport in tokamak plasmas, theory, modelling and comparison with experiments," Plasma Physics and Controlled Fusion, vol. 63, p. 073001, May 2021. 68

[198] J. Seo, H. Jhang, and J.-M. Kwon, "Effects of light impurities on zonal flow activities and turbulent thermal transport," Physics of Plasmas, vol. 29, no. 5, p. 052502, 2022. 68

[199] H. Du, Z.-X. Wang, and J. Q. Dong, "Impurity effects on trapped electron mode in tokamak plasmas," Physics of Plasmas, vol. 23, no. 7, p. 072106, 2016. 68

[200] G. Motojima, S. Masuzaki, T. Morisaki, K. Y. Watanabe, M. Kobayashi, K. Ida, R. Sakamoto, M. Yoshinuma, R. Seki, H. Nuga, T. Tsujimura, C. Suzuki, M. Emoto, Y. Tsuchibushi, T. Murase, and Y. Takeiri, "Particle control in long-pulse discharge using divertor pumping in LHD," Physica Scripta, vol. 97, p. 035601, Feb 2022. 69

[201] W. M. Tang, "Scientific and computational challenges of the fusion simulation project (FSP)," Journal of Physics: Conference Series, vol. 125, p. 012047, Jul 2008. 73

[202] P. K. Atrey, D. Pujara, S. Mukherjee, and R. L. Tanna, "Design, development, and operation of seven channels 100-GHz interferometer for plasma density measurement," IEEE Transactions on Plasma Science, vol. 47, no. 2, pp. 1316–1321, 2019. 76

[203] G. Shukla, K. Shah, M. B. Chowdhuri, H. Raj, T. Macwan, R. Manchanda, U. C. Nagora, R. L. Tanna, K. A. Jadeja, K. Patel, K. B. K. Mayya, P. K. Atrey, and J. G. and, "Observations of toroidal plasma rotation reversal in the Aditya-U tokamak," Nuclear Fusion, vol. 59, p. 106049, Sep 2019. 76, 90

[204] P. C. Liewer, J. M. McChesney, S. J. Zweben, and R. W. Gould, "Temperature fluctuations and heat transport in the edge regions of a tokamak," The Physics of Fluids, vol. 29, no. 1, pp. 309–317, 1986. 76

[205] B. Nold, T. T. Ribeiro, M. Ramisch, Z. Huang, H. W. Müller, B. D. Scott, U. Stroth, and the ASDEX Upgrade Team, "Influence of temperature fluctuations on plasma turbulence investigations with langmuir probes," New Journal of Physics, vol. 14, p. 063022, Jun 2012. 76

[206] T. Macwan, Effect of Short Gas-puff Pulses and Biased-electrode on Transport, MHD Instabilities, Plasma-Wall Interaction and Runaway Electrons in

ADITYA-U Tokamak. PhD thesis, Homi Bhabha National Institute, 2022. 76, 78, 85

[207] R. Dey et al., "Simulations of edge plasma parameters of ADITYA-U tokamak using UEDGE code." Article, private communication, 2021. 76, 85

[208] J. D. Callen and G. L. Jahns, "Experimental measurement of electron heat diffusivity in a tokamak," Physical Review Letters, vol. 38, pp. 491–494, Feb 1977. 78, 85

[209] J. R. Duff, Z. R. Williams, D. L. Brower, B. E. Chapman, W. X. Ding, M. J. Pueschel, J. S. Sarff, and P. W. Terry, "Observation of trapped-electron-mode microturbulence in reversed field pinch plasmas," Physics of Plasmas, vol. 25, no. 1, p. 010701, 2018. 81

[210] D. R. Ernst, P. T. Bonoli, P. J. Catto, W. Dorland, C. L. Fiore, R. S. Granetz, M. Greenwald, A. E. Hubbard, M. Porkolab, M. H. Redi, J. E. Rice, K. Zhurovich, and Alcator C-Mod Group, "Role of trapped electron mode turbulence in internal transport barrier control in the Alcator C-Mod Tokamak," Physics of Plasmas, vol. 11, no. 5, pp. 2637–2648, 2004. 81

[211] H. Arnichand, J. Citrin, S. Hacquin, R. Sabot, A. Krämer-Flecken, X. Garbet, C. Bourdelle, C. Bottereau, F. Clairet, J. C. Giacalone, Z. O. Guimarães-Filho, R. Guirlet, G. Hornung, A. Lebschy, P. Lotte, P. Maget, A. Medvedeva, D. Molina, V. Nikolaeva, D. Prisiazhniuk, the Tore Supra, and the ASDEX Upgrade teams, "Identification of trapped electron modes in frequency fluctuation spectra," Plasma Physics and Controlled Fusion, vol. 58, p. 014037, Nov 2015. 81

[212] G. T. Hoang, C. Bourdelle, X. Garbet, G. Giruzzi, T. Aniel, M. Ottaviani, W. Horton, P. Zhu, and R. V. Budny, "Experimental determination of critical threshold in electron transport on Tore Supra," Physical Review Letters, vol. 87, p. 125001, Sep 2001. 81

[213] J. C. Hillesheim, J. C. DeBoo, W. A. Peebles, T. A. Carter, G. Wang, T. L. Rhodes, L. Schmitz, G. McKee, Z. Yan, G. Staebler, K. H. Burrell, E. J. Doyle, C. Holland, C. C. Petty, S. P. Smith, A. E. White, and L. Zeng, "Observation of a critical gradient threshold for electron temperature fluctuations in the DIII-D tokamak," Physical Review Letters, vol. 110, p. 045003, Jan 2013. 81

[214] D. Villegas, R. Guirlet, C. Bourdelle, G. T. Hoang, X. Garbet, and R. Sabot, "Experimental electron temperature gradient dependence of heavy impurity transport in fusion devices," Physical Review Letters, vol. 105, p. 035002, Jul 2010. 81

[215] W. L. Zhong, X. L. Zou, C. Bourdelle, S. D. Song, J. F. Artaud, T. Aniel, and X. R. Duan, "Convective velocity reversal caused by turbulence transition in tokamak plasma," Physical Review Letters, vol. 111, p. 265001, Dec 2013. 81

[216] B. J. Faber, M. J. Pueschel, J. H. E. Proll, P. Xanthopoulos, P. W. Terry, C. C. Hegna, G. M. Weir, K. M. Likin, and J. N. Talmadge, "Gyrokinetic studies of trapped electron mode turbulence in the helically symmetric experiment stellarator," Physics of Plasmas, vol. 22, no. 7, p. 072305, 2015. 81

[217] C. B. Deng, D. L. Brower, D. T. Anderson, F. S. B. Anderson, A. Briesemeister, and K. M. Likin, "Core density turbulence in the HSX stellarator," Nuclear Fusion, vol. 55, p. 123003, Oct 2015. 81

[218] R. Jha, A. Sen, P. K. Kaw, P. K. Atrey, S. B. Bhatt, N. Bisai, K. Tahiliani, R. L. Tanna, and the ADITYA Team, "Investigation of gas puff induced fluctuation suppression in ADITYA tokamak," Plasma Physics and Controlled Fusion, vol. 51, p. 095010, Aug 2009. 89

[219] G. Rewoldt and W. M. Tang, "Toroidal microinstability studies of high temperature tokamaks," Physics of Fluids B: Plasma Physics, vol. 2, pp. 318–323, 02 1990. 92

[220] L. Bai, X. M. Qiu, L. Huang, and X. M. Song, "A possible hybrid dissipative trapped electron ion temperature gradient mode," Physics of Plasmas, vol. 3, pp. 3004–3012, 08 1996. 92

[221] J. Q. Dong, S. M. Mahajan, and W. Horton, "Coupling of η_i and trapped electron modes in plasmas with negative magnetic shear," Physics of Plasmas, vol. 4, pp. 755–761, 03 1997. 92

[222] R. Cesario, L. Amicucci, A. Cardinali, C. Castaldo, M. Marinucci, L. Panaccione, F. Santini, O. Tudisco, M. Apicella, G. Calabro, C. Cianfarani, D. Frigione, A. Galli, G. Mazzitelli, C. Mazzotta, V. Pericoli, G. Schettini, A. A. Tuccillo, and FTU Team, "Current drive at plasma densities required for thermonuclear reactors," Nature Communications, vol. 1, 2010. 97

[223] F. Wising, D. A. Knoll, S. I. Krasheninnikov, T. D. Rognlien, and D. J. Sigmar, "Simulation of detachment in ITER-geometry using the UEDGE code and a fluid neutral model," Contributions to Plasma Physics, vol. 36, no. 2-3, pp. 309–313, 1996. 97

[224] V. Rozhansky, E. Kaveeva, P. Molchanov, I. Veselova, S. Voskoboynikov, D. Coster, G. Counsell, A. Kirk, S. Lisgo, and the ASDEX-Upgrade Team and the MAST Team, "New B2SOLPS5.2 transport code for H-mode regimes in tokamaks," Nuclear Fusion, vol. 49, p. 025007, Jan 2009. 97

[225] S. Braginskii, "Transport Processes in a Plasma," Reviews of Plasma Physics, vol. 1, p. 205, Jan. 1965. 97

[226] A. V. Chankin, D. P. Coster, N. Asakura, X. Bonnin, G. D. Conway, G. Corrigan, S. K. Erents, W. Fundamenski, J. Horacek, A. Kallenbach, M. Kaufmann, C. Konz, K. Lackner, H. Müller, J. Neuhauser, R. A. Pitts, and M. Wischmeier, "Discrepancy between modelled and measured radial electric fields in the scrape-off layer of divertor tokamaks: a challenge for 2D fluid codes?," Nuclear Fusion, vol. 47, p. 479, May 2007. 97

[227] S. K. Erents, R. A. Pitts, W. Fundamenski, J. P. Gunn, and G. F. Matthews, "A comparison of experimental measurements and code results to determine flows in the JET SOL," Plasma Physics and Controlled Fusion, vol. 46, p. 1757, Sep 2004. 97

[228] M. Wischmeier, M. Groth, S. Wiesen, S. Potzel, L. Aho-Mantila, D. P. Coster, R. Dux, C. Fuchs, A. Kallenbach, H. Müller, D. Reiter, and A. Scarabosio, "Assessment of edge modeling in support of ITER," Journal of Nuclear Materials, vol. 415, no. 1, Supplement, pp. S523–S529, 2011. Proceedings of the 19th International Conference on Plasma-Surface Interactions in Controlled Fusion. 97

[229] C. Pan, S. Wang, and J. Ou, "Co-current rotation of the bulk ions due to the ion orbit loss at the edge of a tokamak plasma," Nuclear Fusion, vol. 54, p. 103003, Sep 2014. 97

[230] C. S. Chang, S. Kue, and H. Weitzner, "X-transport: A baseline nonambipolar transport in a diverted tokamak plasma edge," Physics of Plasmas, vol. 9, pp. 3884–3892, 08 2002. 97

[231] J. T. Omotani and B. D. Dudson, "Non-local approach to kinetic effects on parallel transport in fluid models of the scrape-off layer," Plasma Physics and Controlled Fusion, vol. 55, p. 055009, Apr 2013. 97

[232] J. A. Wesson, "Effect of temperature gradient on plasma sheath," Plasma Physics and Controlled Fusion, vol. 37, p. 1459, Dec 1995. 97

[233] A. Kuley and V. K. Tripathi, "Stabilization of ion temperature gradient driven modes by lower hybrid wave in a tokamak," Physics of Plasmas, vol. 16, 03 2009. 032504. 97

[234] C. S. Chang, S. Ku, P. Diamond, M. Adams, R. Barreto, Y. Chen, J. Cummings, E. D'Azevedo, G. Dif-Pradalier, S. Ethier, L. Greengard, T. S. Hahm, F. Hinton, D. Keyes, S. Klasky, Z. Lin, J. Lofstead, G. Park, S. Parker, N. Podhorszki, K. Schwan, A. Shoshani, D. Silver, M. Wolf, P. Worley, H. Weitzner, E. Yoon, and

D. Zorin, "Whole-volume integrated gyrokinetic simulation of plasma turbulence in realistic diverted-tokamak geometry," Journal of Physics: Conference Series, vol. 180, p. 012057, Jul 2009. 98

[235] Z. Lin, W. M. Tang, and W. W. Lee, "Neoclassical transport in enhanced confinement toroidal plasmas," Physical Review Letters, vol. 78, pp. 456–459, Jan 1997. 98

[236] H. S. Zhang, Z. Lin, and I. Holod, "Nonlinear frequency oscillation of Alfvén eigenmodes in fusion plasmas," Physical Review Letters, vol. 109, p. 025001, Jul 2012. 98

[237] J. Bao, D. Liu, and Z. Lin, "A conservative scheme of drift kinetic electrons for gyrokinetic simulation of kinetic-MHD processes in toroidal plasmas," Physics of Plasmas, vol. 24, 10 2017. 102516. 98

[238] J. Bao, Z. Lin, A. Kuley, and Z. X. Wang, "Electromagnetic particle simulation of the effect of toroidicity on linear mode conversion and absorption of lower hybrid waves," Nuclear Fusion, vol. 56, p. 066007, May 2016. 98

[239] D. P. Fulton, C. K. Lau, I. Holod, Z. Lin, and S. Dettrick, "Gyrokinetic particle simulation of a field reversed configuration," Physics of Plasmas, vol. 23, 01 2016. 012509. 98

[240] S. De, T. Singh, A. Kuley, J. Bao, Z. Lin, G. Y. Sun, S. Sharma, and A. Sen, "Kinetic particle simulations in a global toroidal geometry," Physics of Plasmas, vol. 26, 08 2019. 082507. 104, 118

[241] J. R. Shewchuk, "Triangle: Engineering a 2D Quality Mesh Generator and Delaunay Triangulator," in Applied Computational Geometry: Towards Geometric Engineering (M. C. Lin and D. Manocha, eds.), vol. 1148 of Lecture Notes in Computer Science, pp. 203–222, Springer-Verlag, May 1996. From the First ACM Workshop on Applied Computational Geometry. 104

[242] K. H. Huebner, D. L. Dewhirst, D. E. Smith, and T. G. Byrom, The Finite Element Method for Engineers. Wiley, 2015. 105

[243] J. Bao, C. K. Lau, Z. Lin, H. Y. Wang, D. P. Fulton, S. Dettrick, and T. Tajima, "Global simulation of ion temperature gradient instabilities in a field-reversed configuration," Physics of Plasmas, vol. 26, 04 2019. 042506. 118

[244] C. K. Lau, D. P. Fulton, J. Bao, Z. Lin, T. Tajima, L. Schmitz, S. Dettrick, and the TAE Team, "Cross-separatrix simulations of turbulent transport in the field-reversed configuration," Nuclear Fusion, vol. 59, p. 066018, May 2019. 118

[245] W. W. Heidbrink, "Basic physics of Alfvén instabilities driven by energetic particles in toroidally confined plasmasa," Physics of Plasmas, vol. 15, p. 055501, 02 2008. 118

[246] LHD Experiment Group, "Contribution of the Large Helical Device plasmas to Alfvén eigenmode physics in toroidal plasmas," Plasma Science and Technology, vol. 11, p. 377, Aug 2009. 118